MAGYAR ÁLLAMI
EÖTVÖS LORÁND
GEOFIZIKAI INTÉZET

# GEOFIZIKAI KÖZLEMÉNYEK

ВЕНГЕРСКИЙ
ГЕОФИЗИЧЕСКИЙ
ИНСТИТУТ
ИМ Л. ЭТВЕША

ГЕОФИЗИЧЕСКИЙ
БЮЛЛЕТЕНЬ

BUDAPEST

EÖTVÖS LORÁND
GEOPHYSICAL INSTITUTE
OF HUNGARY

# GEOPHYSICAL TRANSACTIONS

CONTENTS



VOL. 34. NO. 4. JUNE 1989. (ISSN 0016—7177)

# TARTALOMJEGYZÉK

## СОДЕРЖАНИЕ

GEOPHYSICAL TRANSACTIONS 1988
Vol. 34. No. 4. pp. 263–282

# A STUDY OF THE VARIATION OF TIDAL NUMBERS WITH EARTH STRUCTURE

Péter VARGA* and Carlo DENIS**

Studies in earlier works on the determination of Love numbers were based on specific Earth models. This paper, however, aims at the systematic investigation of Love-number variations as a function of varying certain elements of the Earth model. We also examine the possible regional variations of Love numbers and their combinations in the case of a 3D Earth model based on seismology. From these model investigations we concluded that the difference between observation results and the gravity Love-number combination theoretically determined for the PREM cannot be explained by lateral inhomogeneities of the 3D model.

**Keywords: Earth tides, Earth models, Love numbers, radial inhomogeneity, lateral inhomogeneity**

## 1. Brief historical outline and our present conception about the interior of the Earth

In the course of the 4 years between the XVIIIth and XIXth congress of the International Union of Geodesy and Geophysics (held in Hamburg and in Vancouver, respectively), a fundamental change has taken place in our conception about the interior of the Earth.

In order to only approximately demonstrate this development it is worthwhile glancing at the improvement of the conception formed by science on the interior of our planet. 1987 was the 300th anniversary of one of the greatest scientific works ever published, Newton's Philosophiae Naturalis Principia Matematica. This was a turning point in the history of science. It is evident that preceding this time—in ignorance of the law of gravity—one cannot speak about any scientifically grounded idea relating to the interior of the Earth. After Newton, one had to wait for more than 50 years till it could be stated, on the basis of Bouguer's Chimborazo experiment in 1738, that the surface rocks are substantially less dense than the Earth generally i.e. density is increasing from the surface towards the centre of our planet. This was actually the first step towards the understanding of our planet. The real mean density values were obtained only considerably later on the basis of the experiments carried out on the Schiehallion hill and in its surroundings in Scotland in 1774 and of Cavendish's laboratory measurements of 1798.

* Central Office of Geology, Budapest, Arany János u. 25, H–1051
** Geophysics Section, Departement of Astronomy and Astrophysics, University of Liége, 5, Av. de Cointe, B–4200 Liége, Belgium
Manuscript received: 8 March, 1988

Radial density distribution was given for the first time by the theories of Legendre (1793) and Laplace (1825) based on Clairaut's formula (1743) which we now know was based on completely unrealistic assumptions. The core of the Earth appears only in Radou's (1855) and Wiechert's (1897) models.

From the beginning of the XXth century the development and application of seismology in the research of the structure of our planet enabled us to form a detailed conception about the interior of the Earth. Applying Williamson's and Adam's theory set up in 1923 and the seismic data accumulated so far, Bullen created his first model—the A model—in 1936. In the same year Lehmann discovered the solid inner core. Oldham had already proved in 1906 that the outer core was fluid. Bullen's A model together with Gutenberg's velocity data, the so called GBA model, enabled the forming of a rather good overall conception on the structure of the planet that acquited itself well until the early 60s, when the first successful and good quality records of free oscillations afforded possibility of checking the model created earlier. On the basis of free oscillations and the rapidly accumulating seismic data base, a great number of new Earth models appeared in the late 60s, which in fact gave a similar picture of the interior of the Earth as the Bullen model. This new wave of the radially symmetric 1D models can be divided into two main groups:

— optimum models made by using all possible data e.g. model B 497 [Dziewonski–Gilbert 1972] or model B1 of Jordan and Anderson [1974];
— reference models from which in addition to the expectations concerning good approximation of the observations and minimum deviation from the optimum models, primarily simple handling is required. Up to now there has been no final generally accepted reference model, but Dziewonski and Anderson's [1981] Preliminary Reference Earth Model (PREM) is widely used.

Thus we arrived—in our historical review—to 1983 and to the year of the UGGI congress in Hamburg. In the course of the 296 years from the appearance of Newton's Principia, planetary geophysics had reached the stage of having a reliable picture on the radial distribution of density and elastic parameters. Naturally a model like this leaves several questions without answers. If the internal features of our planet had only spherical symmetry, the Earth would be completely lifeless from the viewpoint of tectonics. As it is not so, for the investigation of tectonic and even shorter period effects, the lateral variations of the physical parameters need to be known. Geophysicists have been seeking after this for a long time but a real break-through could be achieved only now, when in the years following the Hamburg UGGI conference an ever increasing number of publications has appeared describing 3D planetary structures instead of one-dimensional models supposing only radial inhomogeneity. The study of lateral inhomogeneities in the interior of the Earth gathered a decisive impetus from two sources, (i) seismic networks set up in the 70s, yielding digital data, and (ii) the appearance of big computers in the early 80s that are able to handle simultaneously the enormous data base. These two facts explain how, between 1983 and 1987, 3D Earth research became a central topic. Compared to the past

we have today substantially improved picture about the inhomogeneities in both the mantle and the core. The lateral inhomogeneities of the upper mantle were investigated in detail by WOODHOUSE and DZIEWONSKI [1984]. In the upper-most 50 km of the upper mantle, lateral inhomogeneities of ±8% appear, whereas from 250 km on only those of ±2.5% and in the immediate vicinity of the transition zone velocity anomalies detectable perpendicularly to the radious amount to 2%. The detected inhomogeneities roughly correspond to the extent of radial velocity changes. In the PREM model e.g. crossing the Mohorovičić discontinuity, the velocity contrast is 15% whereas at depths of 200 and 670 km it is 6 and 7%, respectively.

The velocity anomalies of the upper mantle are connected to the surface elements of global tectonics. This is true primarily for the mantle up to a depth of 250 km, where the most substantial heterogeneities can be found. The roots of the continental shields can be characterized by positive velocity anomalies of 4% and they penetrate down to a depth of 200 km. From here the extent of the velocity anomaly gradually decreases and fully disappeares in the transition zone between 400 and 670 km. The mid-oceanic ridges and the subduction zones of the western part of the Pacific Ocean can be characterized by negative velocity-anomalies traceable up to 350 km depth. On the basis of DZIEWONSKI's model [1984], the 3D model of the lower mantle presents the following picture: in the vicinity of the transition zone and in the *D''* layer covering the core–mantle boundary, the lateral velocity anomalies reach 3%, but in the greater part of the lower mantle these do not exceed 1% i.e. laterally the lower mantle is substantially more homogeneous than the upper mantle. There appears to be no connection between velocity anomalies in the lower mantle and surface tectonics. For understanding the processes within the mantle, it is rather important to investigate the nature of transition zone *C*. It is a question to be decided whether the definite seismic discontinuity at 670 km is a mineralogical phase boundary through which the material of the mantle can flow or if it is a boundary between different materials not allowing such penetration. The question can be solved by investigating the velocity anomalies at both sides of the 670 km discontinuity as follows: If the anomalies on both sides are similar, then the first assumption is more probable. Otherwise one should deduce that the composition of the lower- and upper mantle differs. DZIEWONSKI and WOODHOUSE [1987] compared the lateral distribution of these velocity anomalies and found them, apart from a few exceptions (N-Siberia and the middle part of the Pacific Ocean) to be similar. CREAGER and JORDAN [1986] also proved that there are anomalies crossing the 670 km discontinuity, i.e. transition zone *C* separating the upper and lower mantle is probably of a phase boundary character and as such it does not hinder material flow. Lateral velocity variations throughout the Earth mantle can be explained by temperature, rheological features and density distribution. Studying the 3D model of the upper mantle shows that positive velocity anomalies can be connected to low temperatures and vice versa (i.e. negative anomalies relate to areas of higher temperatures) [DZIEWONSKI–WOODHOUSE 1987].

Interpreting the anomalies of the lower mantle seems to be a more difficult task. There is an opinion that the reason for geoid undulations can be found in the lower mantle [HAGER et al. 1985], although several observations show that horizontal variations of seismic velocities connected to the geoid anomalies can be detected in the Earth's crust and in the uppermost part of the mantle [MASTERS et al. 1982, STARK et al. 1983].

In the interior of the Earth the most drastic changes of physical parameters can be observed at the core–mantle boundary. The anomalies of this discontinuity amount to ± 8 km, as compared to the regular hydrostatic surface [CREAGER–JORDAN 1986, MORELLI et al. 1986]. The topography of the core–mantle boundary shows that the shape of the Earth's core cannot be considered as a hydrostatic surface in the strict sense of the word. STEVENSON [1987] showed, at the same time, that—with highly good approximation—the exterior liquid part of the core is laterally homogeneous.

## 2. Dependence of the Love numbers and their combinations on the Earth's structure

The new 3D model on the Earth's interior is based almost exclusively on seismic results. Naturally it would be good if the conception formed on lateral inhomogeneity could be supported by other, independent observations. The distribution of Love numbers and their combinations obtained from Earth tide observations is one method for such investigations. In this paper we wish first of all to clarify the connection of Love numbers and their combinations with the structure of our planet, and to what extent they contribute to the making of our picture on lateral inhomogeneity more complete.

Theoretical Love numbers ($h$, $k$ and $l$) have already been studied for different spherically symmetrical Earth models by many authors [TAKEUCHI 1950, MOLODENSKY 1953, 1961, ALTERMANN–JAROSCH–PEKERIS 1959, LONGMAN 1962, 1966, ALSOP–KUO 1964, KUO–ERWING 1966, FARELL 1972, 1973, VARGA 1974, DENIS 1974, 1979, WILHELM 1978]. The most important result of these calculations is that the Earth tide varies only to a small extent, provided that the structure of the mantle in the radially symmetric Earth models is only varied between realistic limits determined by seismology.

This paper aims—differently from earlier investigations—at the systematic study of Love-number variations upon changing certain elements of the Earth model. The method is to vary the physical parameters describing the PREM model in the Earth mantle or in some of its spherical layers, and to study the effects on Love numbers. Our calculations are based on MOLODENSKII's inhomogeneous differential equation system [1953, 1961], which was solved by the fourth order Runge–Kutta method, choosing an integration step of $\Delta r/a = 0.001$ ($a = 6371$ km, $r$ is the distance from the Earth's centre). On the basis of the latest seismic data, we supposed the core–mantle boundary (CMB) to be at the relative

depth of $r/a = 0.547$, in spite of the fact that in the PREM (the basis of our calculations) $r/a = 0.546$.

We have investigated not only the dependence of $h$, $k$ and $l$ on the Earth structure, but we have also considered their combinations. The following combinations were determined:

— gravity tidal factor: $\delta = 1 + h - 3/2k$
— tilt factor: $\gamma = 1 + k - h$
— vertical extensometric factor: $\Sigma_V = ah' + 2h$
— horizontal, 2-dimensional deformation factor: $\Sigma_H = 2h - 6l$
— dilatation factor: $\Theta = \Sigma_V + \Sigma_H$

(where $h'$ is a derivative relative to the Earth's radius)

As compared to the PREM, wave velocities $\alpha$ and $\beta$ as well as the compressibility modulus ($\kappa$) and the shear modulus ($\mu$) were changed:

*a)* As a first step we performed the changes as compared to the PREM for the whole mantle within the rather extreme limits of ± 20%. *Table I/a* shows the effect of varying *P*-wave velocities ($\alpha$) (with unvaried $\beta$ and $\varrho$, where $\varrho$ is the density function). It can be seen that changing the value of $\alpha$ has negligible effect on the values of $k$, $h$, $\delta$ and $\gamma$ but substantially modifies the value of $l$ and those of the three deformation factors ($\Sigma_V$, $\Sigma_H$, and $\Theta$).

Varying the *S*-wave velocity ($\beta$)—also within the ±20% extreme limits—only affects the value of $l$ to any significant extent (Table I/b). Tables I/c and I/d show the effect of varying the elastic constants $\kappa$ and $\mu$. The results of the above calculations are illustrated by graphs in *Figs. 1/a* through *h*. It can be seen that the variation of Love numbers and their combinations describing the Earth's reaction in the course of varying the extent of perturbation is on the one hand not linear and on the other, not symmetrical compared to the original case ($\varepsilon = 0$) i.e. to the PREM. Results show that while the dependence of the gravity tidal factor—which can be most reliably recorded by traditional earth-tide observation methods—on the mantle structure is not remarkable, the extensometric components greatly depend on the mantle structure. Unfortunately these can be observed with less accuracy—primarily due to calibration problems—and thus the lateral earth tide variation cannot be effectively examined with them.

*b)* How Love numbers and their combinations depend on the perturbation of the wave velocities at different depths is an interesting question. The results of an investigation into this can be seen in *Table II.* For the investigation a spherical layer of 0.05 relative thickness (~ 319 km) located in various depths was assumed. Tables II/a–d show the position of the upper boundary of the spherical layer. Thus the first and uppermost layer can be found between the depth limits of 1.00–0.95, whereas the lowest layer characterized by a relative depth of 0.6, practically lies on the core–mantle boundary. The respective average depths are as follows: 159, 478, 796, 1115, 1433, 1752, 2071, 2389 and 2708 km. The velocities ($\alpha$ and $\beta$) and the elastic constants ($\kappa$ and $\mu$) were uniformly changed by 10%. Varying the *P*-wave velocity (Table II/a), greater effects were again obtained for the deformation factors than for Love numbers

**a)**

| $\varepsilon$ | $\Delta k$, % | $\Delta h$, % | $\Delta l$, % | $\Delta\delta$, % | $\Delta\gamma$, % | $\Delta\Theta$, % | $\Delta\Sigma_H$, % | $\Delta\Sigma_V$, % |
|---|---|---|---|---|---|---|---|---|
| −0.20 | 8.48 | 28.95 | −64.59 | 12.15 | −22.25 | 79.38 | 94.48 | 68.50 |
| −0.15 | 4.43 | 14.90 | −32.71 | 6.22 | −11.42 | 40.87 | 48.14 | 35.64 |
| −0.10 | 2.31 | 7.58 | −16.30 | 3.14 | − 5.86 | 20.80 | 24.31 | 18.28 |
| −0.05 | 0.96 | 3.07 | − 6.45 | 1.26 | − 2.33 | 8.42 | 9.78 | 7.44 |
| +0.00 | 0.00 | 0.00 | 0.00 | 0.00 | 0.00 | 0.00 | 0.00 | 0.00 |
| +0.05 | −0.31 | −2.22 | 4.69 | −0.91 | 1.68 | − 6.10 | − 7.02 | − 5.43 |
| +0.10 | −1.22 | −3.89 | 8.20 | −1.60 | 2.96 | −10.71 | −12.31 | − 9.56 |
| +0.15 | −1.64 | −5.20 | 10.90 | −2.14 | 3.94 | −14.32 | −17.41 | −12.81 |
| +0.20 | −2.00 | −6.26 | 12.90 | −2.56 | 4.74 | −17.21 | −19.30 | −15.43 |

**b)**

| $\varepsilon$ | $\Delta k$, % | $\Delta h$, % | $\Delta l$, % | $\Delta\delta$, % | $\Delta\gamma$, % | $\Delta\Theta$, % | $\Delta\Sigma_H$, % | $\Delta\Sigma_V$, % |
|---|---|---|---|---|---|---|---|---|
| −0.20 | 26.90 | 22.38 | 50.88 | 1.17 | −8.03 | 6.00 | 2.46 | 8.55 |
| −0.15 | 18.67 | 15.21 | 36.34 | 0.64 | −5.28 | 3.51 | 1.24 | 5.14 |
| −0.10 | 12.27 | 9.90 | 23.56 | 0.36 | −3.38 | 1.64 | 0.34 | 2.58 |
| −0.05 | 5.85 | 4.63 | 11.49 | 0.12 | −1.54 | 0.45 | −0.13 | 0.86 |
| +0.00 | 0.00 | 0.00 | 0.00 | 0.00 | 0.00 | 0.00 | 0.00 | 0.00 |
| +0.05 | − 5.30 | − 3.97 | −10.90 | 0.00 | 1.19 | 0.41 | 0.89 | 0.06 |
| +0.10 | −10.00 | − 7.27 | −21.57 | 0.16 | 2.00 | 1.85 | 2.78 | 1.17 |
| +0.15 | −14.01 | − 9.43 | −32.36 | 0.59 | 2.16 | 4.61 | 6.03 | 3.58 |
| +0.20 | −18.09 | −11.46 | −43.73 | 1.15 | 2.16 | 9.18 | 11.20 | 7.72 |

**c)**

| $\varepsilon$ | $\Delta k$, % | $\Delta h$, % | $\Delta l$, % | $\Delta\delta$, % | $\Delta\gamma$, % | $\Delta\Theta$, % | $\Delta\Sigma_H$, % | $\Delta\Sigma_V$, % |
|---|---|---|---|---|---|---|---|---|
| −0.20 | 1.22 | 3.89 | −8.21 | 1.61 | −2.96 | 10.28 | 10.28 | 8.74 |
| −0.15 | 0.84 | 2.74 | −5.74 | 1.13 | −2.07 | 7.21 | 8.69 | 6.15 |
| −0.10 | 0.55 | 1.71 | −3.52 | 0.70 | −1.30 | 4.52 | 5.43 | 3.86 |
| −0.05 | 0.25 | 0.80 | −1.64 | 0.33 | −0.61 | 2.13 | 2.55 | 1.82 |
| +0.00 | 0.00 | 0.00 | 0.00 | 0.00 | 0.00 | 0.00 | 0.00 | 0.00 |
| +0.05 | −0.22 | −0.70 | 1.52 | −0.29 | 0.55 | −1.91 | −2.28 | −1.64 |
| +0.10 | −0.42 | −1.37 | 2.93 | −0.56 | 1.04 | −3.64 | −4.34 | −3.14 |
| +0.15 | −0.61 | −1.94 | 4.22 | −0.81 | 1.49 | −5.21 | −6.20 | −4.50 |
| +0.20 | −0.77 | −2.49 | 5.28 | −1.02 | 1.88 | −6.64 | −7.89 | −5.74 |

**d)**

| $\varepsilon$ | $\Delta k$, % | $\Delta h$, % | $\Delta l$, % | $\Delta\delta$, % | $\Delta\gamma$, % | $\Delta\Theta$, % | $\Delta\Sigma_H$, % | $\Delta\Sigma_V$, % |
|---|---|---|---|---|---|---|---|---|
| −0.20 | 13.01 | 10.52 | 24.97 | 0.40 | −3.61 | 1.82 | 0.42 | 2.83 |
| −0.15 | 9.13 | 7.24 | 18.05 | 0.21 | −2.41 | 1.03 | 0.07 | 1.73 |
| −0.10 | 6.01 | 4.76 | 11.72 | 0.13 | −1.58 | 0.47 | −0.12 | 0.09 |
| −0.05 | 2.89 | 2.27 | 5.74 | 0.05 | −0.74 | 0.13 | −0.15 | 0.33 |
| +0.00 | 0.00 | 0.00 | 0.00 | 0.00 | 0.00 | 0.00 | 0.00 | 0.00 |
| +0.05 | −2.60 | −1.96 | − 5.39 | −0.01 | 0.59 | 0.08 | 0.33 | −0.09 |
| +0.10 | −5.17 | −3.89 | −10.67 | 0.00 | 1.16 | 0.38 | 0.86 | 0.04 |
| +0.15 | −7.33 | −5.34 | −15.59 | 0.09 | 1.51 | 0.91 | 1.60 | 0.41 |
| +0.20 | −9.67 | −7.00 | −20.63 | 0.15 | 1.94 | 1.67 | 2.56 | 1.02 |

($h$, $k$ and $l$) which reached maximal mean values when the anomaly was in the third layer from the surface. There is a maximum change in $\delta$ and $\gamma$ Love–number combinations for the second layer (at the average depth of 478 km).

Perturbating the shear-wave velocity the greatest changes for $k$, $h$, $\gamma$ and $\Sigma_H$ can be observed when the layer is on the core–mantle boundary (Table II/b). The dilatation ($\Theta$) and the vertical extensometric component ($\Sigma_V$) are sensitive primarily to the variations of the near-surface velocities. $l$ is the most sensitive to the varying of $\beta$ when it is done in the 3rd and 4th layer from the surface. The gravity factor is equally sensitive to such perturbations on the surface and on the core–mantle boundary, but with the opposite sign. Perturbating the elastic constants it can be stated that:

— varying the compressibility modulus ($\kappa$) by 10% (Table II/c) similar influence is obtained when it is carried out in the 1st to the fourth layer. Perturbation in the lower part of the mantle has practically no effect;

— varying the shear modulus ($\mu$) (Table II/d)—similarly to varying $\beta$—the situation is more complicated. The $k$, $h$ and $\gamma$ values depend primarily on the changes carried out in the lower mantle. $l$ and the horizontal extensometric component ($\Sigma_H$) are the most sensitive to the variations of $\kappa$ (and $\beta$) in the 0.95–0.80 relative depth range. The other two extensometric components ($\Theta$, $\Sigma_V$) depend primarily on surface perturbations. The gravity tidal factor is the less dependent on $\mu$ and $\beta$.

⇦ *Table I.* Love number variations versus varying elastic parameters $\alpha$, $\beta$, $\kappa$ and $\mu$ within the limits of $\pm 20\%$. $\varepsilon$ is the extent of variation, $\varepsilon = 0$ corresponds to the PREM

a) Variations of $P$-wave velocity: $\alpha = \alpha_0(1+\varepsilon)$

b) Variations of $S$-wave velocity: $\beta = \beta_0(1+\varepsilon)$

c) Variations of compressibility modulus: $\kappa = \kappa_0(1+\varepsilon)$

d) Variations of shear modulus: $\mu = \mu_0(1+\varepsilon)$

⇦ *I. táblázat.* A Love számok változásai az $\alpha$, $\beta$, $\kappa$ és $\mu$ rugalmas paraméterek $\pm 20\%$ határok közötti változtatásai függvényében. $\varepsilon$ a változtatás mértéke. $\varepsilon = 0$ a PREM esetének felel meg.

a) a longitudinális hullámsebesség változtatásai: $\alpha = \alpha_0(1+\varepsilon)$

b) a transzverzális hullámsebesség változtatásai: $\beta = \beta_0(1+\varepsilon)$

c) az összenyomhatósági modulus értékének változtatásai: $\kappa = \kappa_0(1+\varepsilon)$

d) a nyírási modulus értékének változtatásai: $\mu = \mu_0(1+\varepsilon)$

⇦ *Таблица I.* Изменения чисел Лава в зависимости от изменений упругих параметров $\alpha$, $\beta$, $\kappa$ и $\mu$ в пределах $\pm 20\%$—степень изменений; $\varepsilon = 0$ соответствует случаю PREM

a) Изменение скоростей продольных волн: $\alpha = \alpha_0(1+\varepsilon)$

b) Изменение скоростей поперечных волн: $\beta = \beta_0(1+\varepsilon)$

c) Изменение модуля сжимаемости: $\kappa = \kappa_0(1+\varepsilon)$

d) Изменение модуля скалывания: $\mu = \mu(1+\varepsilon)$

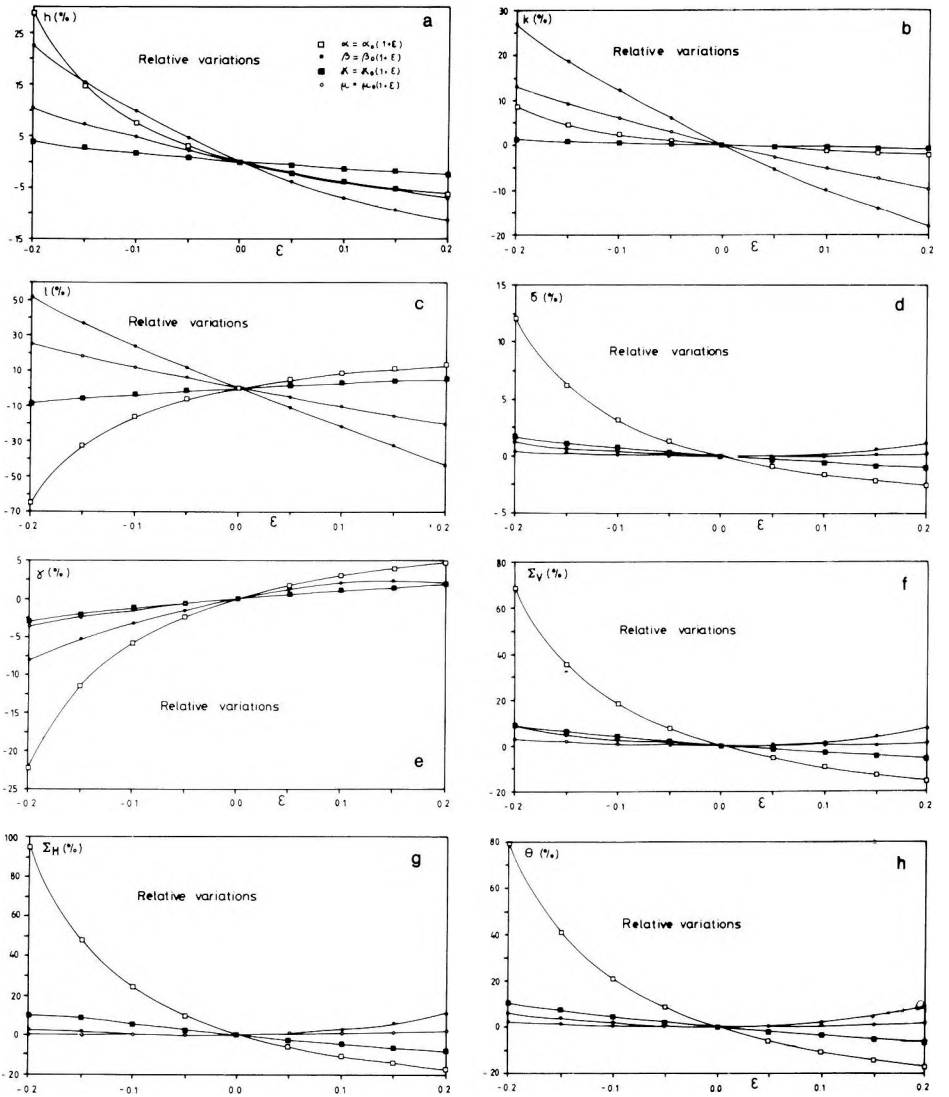
h (%)
a
Relative variations
□ κ = κ0 (1+ε)
• β = β0 (1+ε)
■ K = K0 (1+ε)
○ μ = μ0 (1+ε)
ε
k (%)
b
Relative variations
ε
l (%)
c
Relative variations
ε
δ (%)
d
Relative variations
ε
γ (%)
Relative variations
e
ε
Σv (%)
f
Relative variations
ε
ΣH (%)
g
Relative variations
ε
θ (%)
h
Relative variations
ε

*Fig. 1.* Variations of the second order Love numbers on the surface caused by varying $\alpha$, $\beta$, $\kappa$ and $\mu$ in the Earth's mantle, within the limits of $\pm 20\%$. $\varepsilon = 0$ corresponds to the case of PREM

a) Variation of Love number $h$
b) Variation of Love number $k$
c) Variation of Love number $l$
d) Variation of Love number combination $\delta = 1 + h - 3/2k$
e) Variation of Love number combination $\gamma = 1 + k - h$
f) Variation of Love number combination $\Sigma_V = ah' + 2h$
g) Variation of Love number combination $\Sigma_H = 2h - 6l$
h) Variations of Love number combination $\Theta = \Sigma_V + \Sigma_H = ah' + 4h - 6l$

*1. ábra.* A másodfokú Love számok változásai a felszínen $\alpha$, $\beta$, $\kappa$ és $\mu$ $\pm 20\%$ határok közötti változtatásának hatására a földköpenyben. $\varepsilon = 0$ a PREM esetének felel meg

a) A $h$ Love szám változásai
b) A $k$ Love szám változásai
c) Az $l$ Love szám változásai
d) A $\delta = 1 + h - 3/2k$ kombináció változásai
e) A $\gamma = 1 + k - h$ kombináció változásai
f) A $\Sigma_V = ah' + 2h$ kombináció változásai
g) A $\Sigma_H = 2h - 6l$ kombináció változásai
h) A $\Theta = \Sigma_V + \Sigma_H = ah' + 4h - 6l$ kombináció változásai

*Рис. 1.* Изменения чисел Лава второго порядка на поверхности, обусловленные изменениями $\alpha$, $\beta$, $\kappa$ и $\mu$ в мантии в пределах $\pm 20\%$. $\varepsilon = 0$ соответствует случаю PREM

a) Изменения числа $h$ Лава
b) Изменения числа $k$ Лава
c) Изменения числа $l$ Лава
d) Изменения комбинации $\delta = 1 + h - 3/2k$
e) Изменения комбинации $\gamma = 1 + k - h$
f) Изменения комбинации $\Sigma_V = ah' + 2h$
g) Изменения комбинации $\Sigma_H = 2h - 6l$
h) Изменения комбинации $\Theta = \Sigma_V + \Sigma_H = ah' + 4h - 6l$

*c)* Subsequently, we also investigated the relation between the Love-number variations and the Earth core structure. This investigation was not extended to the extensometric components $\Sigma_H$, $\Sigma_V$ and $\Theta$, since these hardly depend on the structural variations of the lower mantle either (see Table II). Concerning the core, we tried to clarify the following problems:

— dependence of the Love numbers on the density distribution in the core
— dependence of the Love numbers on the density contrast at the CMB
— to what extent Love numbers depend on the uncertainty of the CMB position
— to what extent Love numbers depend on the outer core being a potentially not-ideal fluid.

*Table II.* Love number variations in relation to the PREM model versus increasing the elastic parameters by 10% in spherical layers of 5% thickness of the Earth radius ($a$) and located at different relative depth ($r_{up}/a$)

a) Increasing *P*-wave velocities ($\alpha$) by 10%
b) Increasing *S*-wave velocities ($\beta$) by 10%
c) Increasing compressibility modulus ($\kappa$) by 10%
d) Increasing shear modulus ($\mu$) by 10%.

*II. táblázat.* A Love számok variációi a PREM modellhez viszonyítva a rugalmas paraméterek értékének 10%-kal történő növelésével a gömbhéjak belsejében. A héjak a földsurág 5%-át kitevő vastagságúak különböző relatív mélységeknél ($r_{up}/a$)

a) a longitudinális hullámsebesség 10%-kal történő növelése
b) a transzverzális hullámsebesség 10%-kal történő növelése
c) az összenyomhatósági modulus értékének 10%-kal történő növelése
d) a nyírási modulus értékének 10%-kal történő növelése

*Таблица II.* Изменения чисел Лава по сравнению со случаем PREM при увеличении значений упругих параметров на 10% внутри сферических оболочек, мощность которых составляет 5% от радиуса Земли при различных относительных глубинах ($r_{up}/a$)

a) Увеличение скоростей продольных волн на 10%
b) Увеличение скоростей поперечных волн на 10%
c) Увеличение модуля сжимаемости на 10%
d) Увеличение модуля скалывания на 10%

a)

| $r_{up}/a$ | $\Delta k$, % | $\Delta h$, % | $\Delta l$, % | $\Delta\delta$, % | $\Delta\gamma$, % | $\Delta\Theta$, % | $\Delta\Sigma_H$, % | $\Delta\Sigma_V$, % |
|---|---|---|---|---|---|---|---|---|
| 1.00 | −0.19 | −0.92 | 1.64 | −0.42 | 0.74 | −6.30 | −2.69 | −8.89 |
| 0.95 | −0.29 | −1.01 | 1.99 | −0.43 | 0.80 | −1.62 | −3.11 | −0.55 |
| 0.90 | −0.32 | −0.95 | 2.23 | −0.39 | 0.72 | −1.59 | −3.16 | −0.47 |
| 0.85 | −0.32 | −0.71 | 1.76 | −0.29 | 0.54 | −1.22 | −2.45 | −0.33 |
| 0.80 | −0.16 | −0.47 | 1.29 | −0.19 | 0.35 | −0.80 | −1.64 | −0.20 |
| 0.75 | −0.06 | −0.24 | 0.82 | −0.10 | 0.19 | −0.45 | −0.93 | −0.10 |
| 0.70 | 0.00 | −0.08 | 0.35 | −0.04 | 0.07 | −0.17 | −0.36 | −0.03 |
| 0.65 | 0.00 | 0.00 | 0.00 | 0.00 | 0.00 | −0.02 | −0.06 | 0.00 |
| 0.60 | 0.00 | 0.00 | 0.00 | 0.00 | 0.00 | 0.00 | 0.00 | 0.00 |

b)

| $r_{up}/a$ | $\Delta k$, % | $\Delta h$, % | $\Delta l$, % | $\Delta\delta$, % | $\Delta\gamma$, % | $\Delta\Theta$, % | $\Delta\Sigma_H$, % | $\Delta\Sigma_V$, % |
|---|---|---|---|---|---|---|---|---|
| 1.00 | −0.09 | 0.55 | −1.17 | 0.33 | −0.54 | 7.07 | 1.81 | 10.85 |
| 0.95 | −0.19 | 0.41 | −2.81 | 0.30 | −0.46 | 1.07 | 2.68 | −0.09 |
| 0.90 | −0.45 | 0.11 | −3.63 | 0.24 | −0.30 | 0.86 | 2.72 | −0.48 |
| 0.85 | −0.80 | −0.37 | −3.63 | 0.12 | −0.03 | 0.31 | 1.96 | −0.89 |
| 0.80 | −1.12 | −0.84 | −3.28 | 0.01 | 0.23 | −0.32 | 0.95 | −1.24 |
| 0.75 | −1.48 | −1.27 | −2.81 | −0.09 | 0.48 | −0.95 | −0.15 | −1.52 |
| 0.70 | −1.80 | −1.67 | −2.23 | −0.18 | 0.71 | −1.57 | −1.28 | −1.77 |
| 0.65 | −2.09 | −2.06 | −1.64 | −0.26 | 0.91 | −2.16 | −2.87 | −2.00 |
| 0.60 | −2.57 | −2.62 | −1.17 | −0.37 | 1.20 | −2.90 | −3.58 | −2.41 |

c)

| $r_{up}/a$ | $\Delta k$, % | $\Delta h$, % | $\Delta l$, % | $\Delta\delta$, % | $\Delta\gamma$, % | $\Delta\Theta$, % | $\Delta\Sigma_H$, % | $\Delta\Sigma_V$, % |
|---|---|---|---|---|---|---|---|---|
| 1.00 | −0.06 | −0.29 | 0.59 | −0.14 | 0.23 | −1.93 | −0.87 | −2.69 |
| 0.95 | −0.10 | −0.32 | 0.70 | −0.14 | 0.26 | −0.53 | −1.02 | −0.18 |
| 0.90 | −0.10 | −0.31 | 0.70 | −0.12 | 0.23 | −0.51 | −1.01 | −0.15 |
| 0.85 | −0.10 | −0.23 | 0.59 | −0.10 | 0.17 | −0.39 | −0.79 | −0.11 |
| 0.80 | −0.06 | −0.14 | 0.47 | −0.06 | 0.12 | −0.26 | −0.54 | −0.07 |
| 0.75 | −0.03 | −0.08 | 0.23 | −0.03 | 0.06 | −0.15 | −0.31 | −0.03 |
| 0.70 | −0.03 | −0.03 | 0.12 | −0.02 | 0.03 | −0.05 | −0.12 | −0.01 |
| 0.65 | 0.00 | 0.00 | 0.00 | 0.00 | 0.00 | 0.00 | 0.00 | 0.00 |
| 0.60 | 0.00 | 0.00 | 0.00 | 0.00 | 0.00 | 0.00 | 0.00 | 0.00 |

d)

| $r_{up}/a$ | $\Delta k$, % | $\Delta h$, % | $\Delta l$, % | $\Delta\delta$, % | $\Delta\gamma$, % | $\Delta\Theta$, % | $\Delta\Sigma_H$, % | $\Delta\Sigma_V$, % |
|---|---|---|---|---|---|---|---|---|
| 1.00 | −0.04 | 0.24 | −0.46 | −0.15 | −0.23 | 3.30 | 0.79 | 5.11 |
| 0.95 | −0.10 | 0.18 | −1.29 | −0.14 | −0.20 | 0.47 | 1.22 | −0.06 |
| 0.90 | −0.22 | 0.02 | −1.64 | −0.10 | −0.13 | 0.37 | 1.23 | −0.25 |
| 0.85 | −0.38 | −0.19 | −1.76 | −0.05 | 0.00 | 0.11 | 0.89 | −0.45 |
| 0.80 | −0.55 | −0.42 | −1.64 | 0.00 | 0.13 | −0.18 | 0.43 | −0.61 |
| 0.75 | −0.70 | −0.62 | −1.29 | −0.04 | 0.23 | −0.47 | −0.09 | −0.75 |
| 0.70 | −0.87 | −0.82 | −1.06 | −0.09 | 0.35 | −0.77 | −0.62 | −0.87 |
| 0.65 | −1.03 | −1.00 | −0.82 | −0.13 | 0.43 | −1.05 | −1.14 | −0.98 |
| 0.60 | −1.25 | −1.27 | −0.59 | −0.18 | 0.58 | −1.41 | −1.73 | −1.18 |

In *Table III* deviations of the Love number combinations (from the PREM model) for two different core models with theoretically assumed, completely invalid density distributions are presented. Although there is a considerable difference between the homogeneous hydrostatic core and the real case, it is hardly reflected in the $\delta$ and $\gamma$ values (i.e. the density distribution in the core does not remarkably affect Love-number combinations). On the contrary, the core density at the core–mantle boundary affects the $h$, $k$, $l$, $\delta$ and $\gamma$ values *(Fig. 2)*. In reality, however, this density may vary between rather narrow limits 9.9–10.2 g/cm$^3$ [PRESS 1970]. Accordingly, the variations for the investigated quantities may be as follows:

$\Delta k = 0.67\%$, $\Delta h = 0.40\%$, $\Delta l = 0.43\%$, $\Delta\delta = 0.22\%$, and $\Delta\gamma = 0.18\%$.

Since the variations given by PRESS relate to the maximum possible density variation, it can be concluded that the effect of the core on the surface is not remarkable in this respect.

Although the average position of the CMB is known rather precisely undulations up to 10 km may be envisaged. The influence of relative depth of the CMB on Love numbers can be seen in *Fig. 3*. The variations belonging to a 10 km undulation are not very large:

$\Delta k = 0.43\%$, $\Delta h = 0.21\%$, $\Delta l = 0.10\%$, $\Delta\delta = 0.06\%$ and $\Delta\gamma = 0.04\%$.

| Core model | $\Delta k$(%) | $\Delta h$(%) | $\Delta l$(%) | $\Delta\delta$(%) | $\Delta\gamma$(%) |
|---|---|---|---|---|---|
| Constant core density | −3.01 | −1.52 | 4.76 | 0.37 | 0.03 |
| Hydrostatic density distribution | −0.46 | −0.40 | −0.24 | −0.02 | 0.13 |

*Table III.* Dependence of Love numbers (and their combinations) on the selected core model, (in relation to the respective PREM values)

*III. táblázat.* A Love számok és kombinációik változásai a választott mag-modell függvényében (a megfelelő PREM értékekhez viszonyítva)

*Таблица III.* Изменения чисел Лава и их комбинаций как функция выбранной модели Земли (отнесенные к соответствующим значениям в случае PREM)

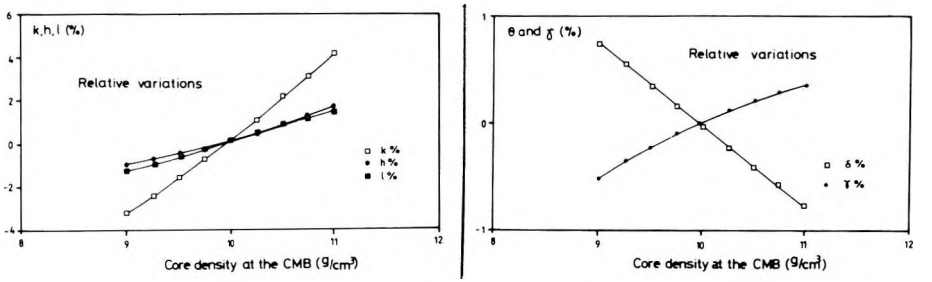


*Fig. 2.* Effect of the core density at the core–mantle boundary on Love numbers and their combinations in relation to the core density in the PREM (9.9037 g/cm$^3$)

*2. ábra.* A mag sűrűségének hatása a Love-számokra és kombinációikra a mag–köpeny határon a PREM mag sűrűségének értékéhez viszonyítva (9,9037 g/cm$^3$)

*Рис. 2.* Влияние изменений плотности земного ядра по сравнению с плотностью ядра в PREM (9,9037 г/см$^3$) на числа Лава и их комбинации на границе мантии с ядром

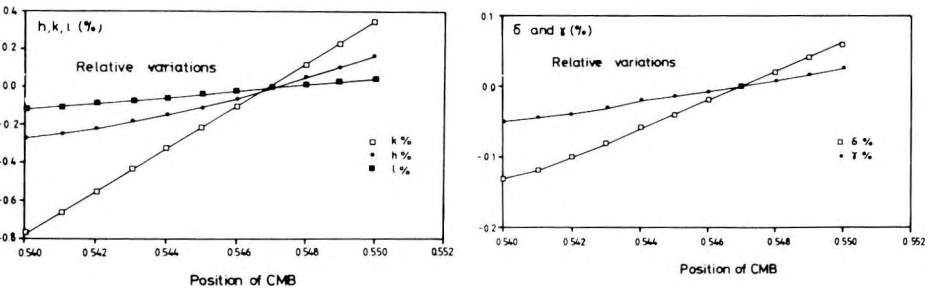


*Fig. 3.* Effect of the relative depth of the core–mantle boundary on Love numbers and their combinations in relation to the value (0.547) accepted in PREM

*3. ábra.* A mag–köpeny határ relatív mélységének hatása a Love-számokra és kombinációikra a PREM-ben elfogadott értékhez (0,547) viszonyítva

*Рис. 3.* Влияние изменений относительной глубины залегания границы мантии с ядром по сравнению с плотностью ядра в PREM (0,547) на числа Лава и их комбинации

The problem of the outer core being an ideal fluid or not has been an interesting question for geophysics for a long time. Therefore such PREM variations were calculated which assume a certain extent of rigidity in the outer core *(Fig. 4)*. Earlier it was assumed that the shear modulus of the outer can even be as high as $10^9$ N/m$^2$ [SATO–ESPINOZA 1967, IBRAHIM 1973]. Nowadays KUO, ZHANG and CHU [1986] showed that this value should be less than $10^8$ N/m$^2$. If this is so, then the possible deviation of the outer core from the ideal fluid state does not influence Love numbers.

Summerizing what has been said concerning Love numbers and their combinations, one can say that:

— the possible uncertainties of the core model do not influence the calculated values of Love numbers to any great extent;

— the lateral variations of the 3D model in the upper mantle are considerable, whereas in the lower mantle they are not. If this is so, then the regional variations of the earth tide observations should reflect the lateral inhomogeneities of the upper mantle.

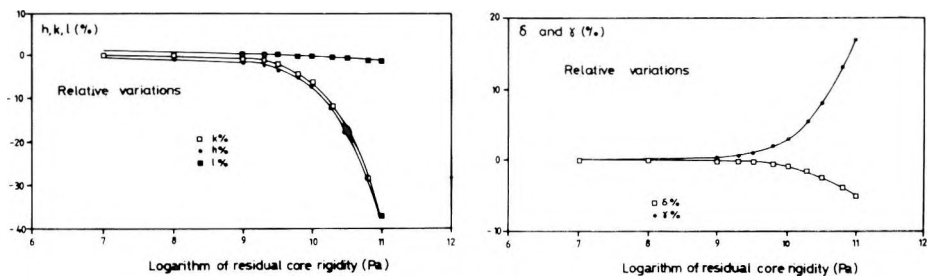


*Fig. 4.* Effect of the rigidity of the outer core on the Love numbers and their combinations compared to the ideal fluid state ($\mu = 0$)

*4. ábra.* A külső mag szilárdságának hatása a Love-számokra és kombinációikra. A változások viszonyítási alapja az ideális cseppfolyós állapot ($\mu = 0$)

*Рис. 4.* Влияние изменений твердости внешнего ядра по сравнению с идеально жидким состоянием ($\mu = 0$) на числа Лава и их комбинации

### 3. Possible variations of Love numbers and their combinations on the Earth's surface

The applicability of earth tide research for the investigation of lateral inhomogeneities primarily depends on whether or not these result in measurable variations of Love numbers and their combinations on the Earth surface. MOLODENSKII and KRAMER [1980] studied different lateral inhomogeneity models. The basic feature of their models is that the elastic wave velocities under the oceans are 5% lower than under the continents in the whole mantle or in certain depth ranges. The effects are determined in each case for the gravity tidal factor $\delta = 1 + h - 3/2k$.

In the first model *(Fig. 5/a)* *P*-wave velocities ($\alpha$) are 5% higher under the continents up to 300 km from the surface whereas in the second case this 5% increase in velocity characterises the *S*-waves ($\beta$) *(Fig. 5/b)*. In the third model the lateral inhomogeneity of the *P*-wave penetrates the whole mantle *(Fig. 5/c)*. For the first model the maximum change in $\delta$ is 0.3% whereas for the second it is 1.2% and for the third one it is 1.25%.

The common features of the results are as follows:

- the calculated $\delta$ anomalies follow the boundaries of the lateral inhomogeneities;
- the amplitudes of the anomalies do not depend on the size of the source (e.g. the amplitude of the anomaly for Australia equals that obtained for Eurasia).

From our investigations, in the course of which first the values of $\alpha$ and then that of $\beta$ were changed by 5% in the upper-most 300 km in relation to the PREM, variations in $\delta$ of 0.2% and 0.3% were obtained. Changing $\alpha$ by 5% in the whole mantle resulted in a change of 1.0%. Comparing our results with MOLODENSKII–KRAMER's data for laterally inhomogeneous models, it can be stated that the magnitude of the regional Love-number variations caused by lateral inhomogeneities can be estimated by means of two radial models: one containing the modified value of the physical parameter as in a whole spherical layer, the other is the PREM. Naturally, in this way the regional anomalies cannot be described, however, the magnitudes of the possible anomalies will be estimated.

Starting from the above conclusions, the magnitude of $\delta$ variations expected on the basis of the 3D model prepared by DZIEWONSKI and WOODHOUSE can be determined. For this, however, it should be assumed that the Lamé constants are equal in the mantle, i.e. $\mu = \lambda$, and thus $\alpha = \sqrt{3}\,\beta$. As it is known, this assumption is true in the mantle to a rather good approximation. This assumption was necessary because the 3D model was based only on *S*-waves for the upper mantle whereas for the lower mantle only *P*-waves are used. Considering the above facts we tried to estimate the possible magnitudes of the regional variations of Love numbers and their combinations on the basis of the studies of WOODHOUSE and DZIEWONSKI [1984] as well as DZIEWONSKI [1984].

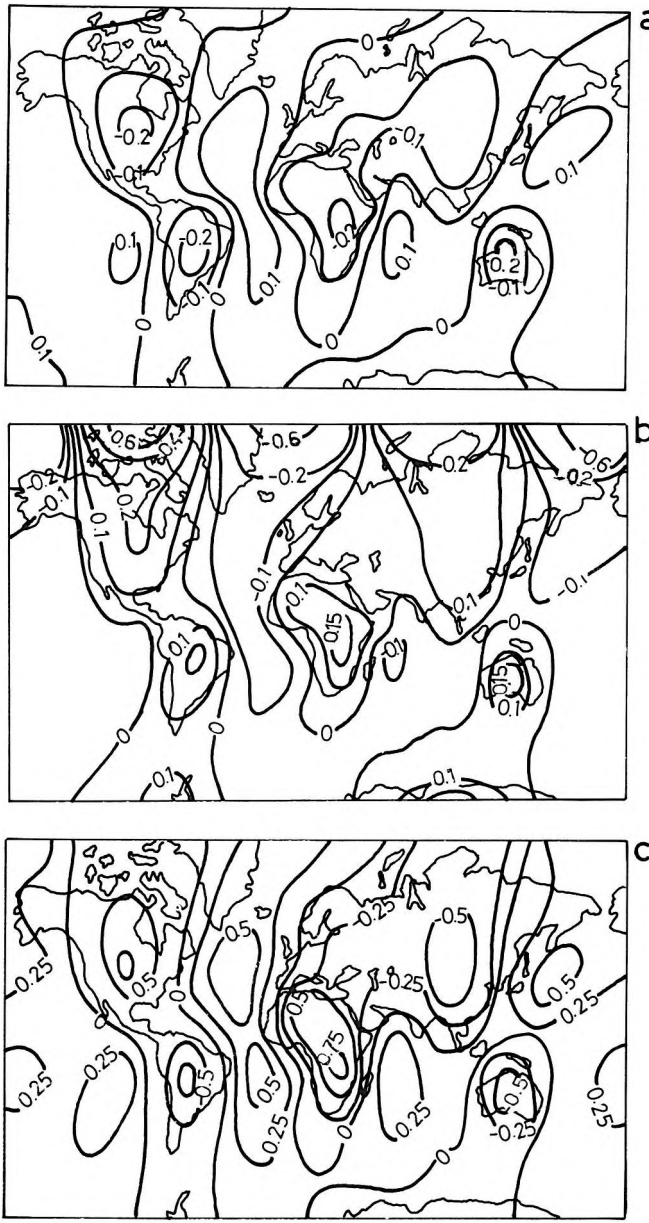
a.
b.
c.

For this purpose a model was studied in which, in the upper mantle ($1.00 \geqq r/a \geqq 0.90$) $\alpha$ exceeds by 8% and $\beta$ by 5% the PREM values (*Table IV*), whereas in transition zone *C*, $\alpha$ and $\beta$ exceed the PREM values by 3 and 2% respectively. In the lower mantle the seismic velocities are only 1% higher than those of the reference model, except in layer *D″* at the core–mantle boundary. Here $\alpha$ exceeds by 3% and $\beta$ by 2% the velocities accepted in the PREM. The deviation from the reference model (Table IV) is the least in the case of gravity tidal factor $\delta$ ($\Delta\delta = -0.72\%$) that can be best observed, whereas the greatest deviations were found in the extensometric components.

| Definition of the model | Deviation of Love numbers and their combinations from PREM (in %) |
|---|---|
| Upper mantle | |
| $1.00 \geqq r/a > 0.90$ | $\Delta k = -1.80$ |
| $\alpha = 1.08 \cdot \alpha_0$ | $\Delta h = -2.67$ |
| $\beta = 1.05 \cdot \beta_0$ | $\Delta l = 0.82$ |
| *C* layer | |
| $0.90 \geqq r/a > 0.85$ | $\Delta\delta = -0.72$ |
| $\alpha = 1.03 \cdot \alpha_0$ | $\Delta\gamma = 1.59$ |
| $\beta = 1.02 \cdot \beta_0$ | $\Delta\Theta = -4.99$ |
| Lower mantle | |
| $0.85 \geqq r/a > 0.60$ | $\Delta\Sigma_H = -5.26$ |
| $\alpha = 1.01 \cdot \alpha_0$ | $\Delta\Sigma_V = -4.79$ |
| $\beta = 1.01 \cdot \beta_0$ | |
| *D″* layer | |
| $0.60 \geqq r/a > 0.55$ | |
| $\alpha = 1.03 \cdot \alpha_0$ | |
| $\beta = 1.02 \cdot \beta_0$ | |

*Table IV.* Variations of Love numbers and their combinations for the 3D model suggested by DZIEWONSKI and WOODHOUSE [1984] as well as DZIEWONSKI [1984]. (Reference basis: $\alpha_0$ and $\beta_0$ velocities of PREM)

*IV. táblázat.* A Love-számok és kombinációik változásai a DZIEWONSKI és WOODHOUSE [1984] és DZIEWONSKI [1984] által javasolt 3D modellre. (Vonatkoztatási alap: PREM sebességek)

*Таблица IV.* Изменения чисел Лава и их комбинации в трехмерной модели, предложенной Дзевонским и Вудхаузом [DZIEWONSKI and WOODHOUSE 1984] и Дзевонским [DZIEWONSKI 1984] (основа для сравнения – скорости PREM)

*Fig. 5.* Effect of velocity inhomogeneity on gravity tidal factor $\delta$
a) $\alpha$ is greater by 5% under the continents than under the oceans up to 300 km depth
b) $\beta$ is greater by 5% under the continents than under the oceans up to 300 km depth
c) $\alpha$ is greater by 5% under the continents than under the oceans in the whole mantle

*5. ábra.* A sebesség inhomogenitásának hatása a földárapály paraméterre ($\delta$)
a) $\alpha$ értéke 5%-kal nagyobb a kontinensek alatt, mint az óceánok alatt, 300 km mélységig
b) $\beta$ értéke 5%-kal nagyobb a kontinensek alatt, mint a óceánok alatt, 300 km mélységig
c) $\alpha$ értéke 5%-kal nagyobb a kontinensek alatt, mint az óceán alatt, az egész köpenyben

*Рис. 5.* Влияние неоднородностей скоростей на параметр земных приливов ($\delta$)
a) Значение $\alpha$ под континентами на 5% больше, нежели под океанами, до глубин 300 км
b) Значение $\beta$ под континентами на 5% больше, нежели под океанами, до глубин 300 км
c) Значение $\alpha$ под континентами на 5% больше, нежели под океанами, на всю мантию

The gravity tidal factor obtained for the PREM model is $\delta = 1.1564$. This is in rather good agreement with the result of DEHANT and DUCARME [1986] ($\delta = 1.1543$), which they obtained starting from WAHR's theory [1981]. Both results considerably differ, however, from the planetary mean value of the observation results $\delta = 1.161$ [MELCHIOR 1977]. The reasons for this deviation need to be clarified both from the side of the theory and from that of observation techniques. This is one of the most important tasks of today's earth tide research.

## Acknowledgement

P. Varga conducted his part of the research work as a Humboldt research fellow during his stay at the Geodetical Institute of Stuttgart University. Carlo Denis is grateful to the Fonds National de la Recherche Scientifique (Brussels, Belgium) for research funds which have enabled him to undertake this study.

## REFERENCES

ALSOP L. E., KUO J. T. 1964: The characteristics of semi-diurnal earth tidal components for various Earth models. Ann. Geophys., **20**, 3, pp. 286–300

ALTERMAN Z., JAROSCH H., PEKERIS C. L. 1959: Oscillation of the Earth. Proc., Roy. Soc. London, Ser. A, **252**, pp. 80–95

CREAGER K. C., JORDAN T. H. 1986: Aspherical structure of the core–mantle boundary, from PKP travel times. Geophys. Res. Lett., **13**, 13, pp. 1497–1500

DEHANT V., DUCARME B. 1987: Comparison between the theoretical and observed tidal gravimetric factors. Phys. Earth Plan. Int., **49**, 3–4, pp. 192–212

DENIS C. 1974: Oscillations de configurations sphériques auto-gravitantes et applications á la Terre. Thése de doctorat, Université de Liége, 350 p.

DENIS C. 1979: Static and dynamic effects in theoretical Love numbers. In: BONATZ M., MELCHIOR P. (eds.) Proc. 8th Int. Symp. Earth Tides, Bonn, 1977. pp. 709–729

DZIEWONSKI A. M., GILBERT F. 1972: Observations of normal modes from 84 recordings of the Alaskan earthquake of 1964 March 28. Geophys. J., **27**, 4, pp. 393–446

DZIEWONSKI A. M., ANDERSON D. L. 1981: Preliminary reference Earth Model. Phys. Earth Plan. Int., **25**, 4, pp. 297–356

DZIEWONSKI A. M. 1984: Mapping the lower mantle: determination of lateral heterogenity in *P* velocity up to degree and order 6. J. Geophys. Res., **89**, B 7, pp. 5929–5952

DZIEWONSKI A. M., WOODHOUSE J. H. 1987: Global images of the Earth's interior. Science, **236**, pp. 761–797

FARRELL W. E. 1972: Deformations of the Earth by surface loads. Rev. Geophys. Space Phys., **10**, 3, pp. 761–797

FARRELL W. E. 1973: Earth tides, ocean tides and tidal loading. Phil. Trans. Roy. Soc., London, Ser. A, **274**, pp. 253–259

HAGER B. H., CLAYTON R. W., RICHARDS M. A., COMER R. P., DZIEWONSKI A. M. 1985: Lower mantle heterogeneity, dynamic topography and the geoid. Nature, **313**, pp. 541–545

IBRAHIM A. K. 1973: Evidences for a low velocity core–mantle transition zone. Phys. Earth Plan. Int., **7**, 2, pp. 187–198

JORDAN T. H., ANDERSON D. L. 1974: Earth structure from free oscillations and travel times. Geophys. J., **36**, 2, pp. 411–459

KUO J. T., EWING M. 1966: Spatial variations of tidal gravity. In: STEINHART J. S., SMITH T. J. (eds.) Earth beneath the continents. pp. 595–610

KUO J. T., ZHANG V., CHU Y. 1986: Time-domain total Earth tides. Proc. 10th Int. Symp. on Earth tides, Consejo Superior de Investigaciones Cientificas, Madrid, pp. 491–506

LONGMAN I. M. 1962: A Green's function for determining the deformation of the Earth under surface mass loads. I. Theory. J. Geophys. Res., **67**, 2, pp. 845–850

LONGMAN I. M. 1966: Computation of Love numbers and load deformation coefficients for a model Earth. Geophys. J. Roy. Astr. Soc. **11**, 1–2, pp. 133–137

MASTERS G., JORDAN T. H., SILVER P. G., GILBERT F. 1982: A spherical Earth structure from fundamental spheroidal mode data. Nature, **298**, pp. 609–611

MELCHIOR P. 1977: Report on activities of the International Centre for Earth Tides. Proc. of the 8th Int. Symp. on the Earth Tides, Bonn, pp. 30–41

MOLODENSKII M. S. 1953: Elastic tides, free nutations, some questions concerning the internal structure of the Earth (in Russian). Trudy Geofis. Inst. Akad. Nauk S.S.S.R., Moscow, No. **19**, (146), pp. 3–42

MOLODENSKII M. S., KRAMER M. V. 1961: Earth tides and nutations of the earth (in Russian). Izd. Akad. Nauk S.S.S.R., Moscow, 40 p.

MOLODENSKII M. S., KRAMER M. V. 1980: Influence of big scale horizontal inhomogenities of the mantle and the tides of the earth. Fizika Zemli, **1**, pp. 3–20

MORELLI A., DZIEWONSKI A. M., WOODHOUSE J. H. 1986: Anisotropy of the inner core inferred from PKIKP travel times. Geophys. Res. Let., **13**, 13, pp. 1545–1548

PRESS F. 1970: Earth models consistent with geophysical data. Phys. Earth Plan. Int., **3**, pp. 3–22

SATO R., ESPINOSA A. F. 1967: Dissipation in the Earth's mantle and rigidity and viscosity in the Earth's core determined from waves multiply reflected from the mantle-core boundary. Bull., Seis. Soc. Am., **57**, 5, pp. 829–856

STARK M., FORSYTH D. W. 1983: The geoid, small-scale convection, and differential travel time anomalies of shear waves in the central Indian ocean. J. Geophys. Res., **88**, Ser. B, 3, pp. 2273–2294

STEVENSON D. J. 1987: Limits on lateral density and velocity variations in the Earth's outer core. Geophys. J. Roy. Astr. Soc., **88**, 1, pp. 311–319

TAKEUCHI M. 1950: On the earth tide of the compressible earth of variable density and elasticity. Trans. Am. Geophys. Un., **31**, 5, pp. 651–689

VARGA P. 1974: Dependence of the Love numbers upon the inner structure of the Earth and comparison of theoretical models with results of measurements. PAGEOPH, **112**, pp. 777–785

WAHR J. M. 1981: Body tides on an elliptical, rotating, elastic and oceanless earth. Geophys. J. Roy. Astr. Soc., **64**, 3, pp. 677–703

WILHELM H. 1978: Upper mantle structure and global earth tides. J. Geophys., **44**, 5, pp. 435–439

WOODHOUSE J. H., DZIEWONSKI A. M. 1984. Mapping the upper mantle: three-dimensional modeling of Earth structure by inversion of seismic waveforms. J. Geophys. Res., **89**, Ser. B, 7, pp. 5953–5986

## A FÖLDÁRAPÁLY PARAMÉTEREK FÖLDSZERKEZET OKOZTA LEHETSÉGES VÁLTOZÁSAI

VARGA Péter és Carlo DENIS

A Love számok meghatározásával foglalkozó korábbi munkák egyes konkrét földmodellekre alapozzák vizsgálataikat. Jelen dolgozat célja viszont: szisztematikusan vizsgálni, hogyan változnak a Love számok a Földmodell egyes elemeinek megváltoztatása függvényében. Megvizsgáljuk azt is, hogy a szeizmológiai alapokon nyugvó 3D földmodell esetében a Love számok és kombinációinak milyen regionális változásai lehetségesek.

## ВОЗМОЖНЫЕ ИЗМЕНЕНИЯ ПАРАМЕТРОВ ЗЕМНЫХ ПРИЛИВОВ, СВЯЗАННЫЕ СО СТРУКТУРОЙ ЗЕМЛИ

Пётер ВАРГА и Карло ДЕНИС

В прежних работах по определению чисел Лава исследования базировались на каких-либо конкретных моделях Земли. Цель же настоящей статьи заключается в систематическом изучении изменений чисел Лава в зависимости от изменений тех или иных элементов модели Земли, а также региональных изменений чисел Лава и их комбинаций для трехмерной модели Земли, основывающейся на сейсмологических данных.

GEOPHYSICAL TRANSACTIONS 1988
Vol. 34. No. 4. pp. 283–294

# SEISMIC ACTIVITY OF THE PANNONIAN BASIN AND COMPARISON WITH OTHER GEOPHYSICAL FIELDS

Uwe WALZER*, Richard MAAZ* and László TÓTH**

From the earthquakes taking place in the Pannonian Basin from 1763 till 1984, seismic maps were constructed by means of a computer. The maps with lines of equal epicentral density and magnitude density are particularly closely related to the tectonic units of the basin striking WSW–ENE. Maxima in the afore-said seismic maps are linked with minima in the map of the temperature at a depth of 2 km. The distribution of the epicentral and magnitude density maxima also exhibits a relationship with the heat flow minima and, to a somewhat lesser extent, with the maxima of the horizontal geothermal gradient and with the positive regional Bouguer anomalies.

**Keywords: seismicity maps, epicenters, magnitude density, temperature, crust, Pannonian Basin, seismology**

## 1. Introduction

The aim of this paper is to present the seismic activity of the Pannonian Basin with the help of maps in a manner as objective as possible. The relationship between this distribution and geophysical fields of a different type and the geology is to be investigated. It is clear that, from a given seismological catalogue, seismological fields can be derived in various manners. The maps with lines of equal seismic energy per unit of time and area are governed by a few high-energy earthquakes.

Consequently, they need not necessarily be in agreement with a map (which unfortunately cannot be prepared) of the same type, which would be applicable, e.g. for a more recent geological period, such as the Holocene or the Quarternary. For this reason, maps with lines of equal density of the seismic epicentres are more important for comparison with tectonic maps because the epicentres are less randomly distributed. However, if one wants to attach greater importance to the stronger earthquakes, it is possible to introduce the magnitude or the epicentral intensity as a weighting factor. The maps were constructed with the help of a computer, and the isolines were printed by means of a plotter.

* Central Institute of Physics of the Earth of the Academy of Sciences of the GDR, Burgweg 11, DDR-6900 Jena, German Dem. Rep.
** Geodetic and Geophysical Research Institute of the Hungarian Academy of Sciences, Seismological Observatory, Meredek u. 18, H-1112 Budapest, Hungary
Manuscript received (revised version): 15 March, 1988

## 2. Computation of fields of seismic activity

The catalogue of all known earthquakes in the Pannonian Basin by ZSIROS et al. [1988] forms the data base for the seismological part of the paper. It contains 2745 seismic events. With respect to the historical earthquakes, it is based mainly on RÉTHLY [1952]. The parameters of some historical earthquakes have, however, been re-estimated. The catalogue prepared by ZSIROS et al. [1988] contains for each earthquake the focal time, geographical latitude and longitude of the epicentre, the focal depth—computed according to the Kövesligethy formula [see SPONHEUER 1960], the magnitude, the epicentral intensity on the MSK–64 scale [see SPONHEUER 1965 and WILLMORE 1979], the error of the determination of the epicentre $\sigma_i$, the geographic designation of the epicentre, the error of the intensity determination and the literature source. According to the error of the determination of the epicentre, the earthquakes have been formally categorized in five classes: $\sigma_i = 5$ km, $\sigma_i = 10$ km, $\sigma_i = 20$ km, $\sigma_i = 50$ km, $\sigma_i =$ undetermined. Only earthquakes of the first three categories have been used in the computation of the maps so as not to adversely affect the accuracy of the maps. Since the catalogue obviously contains only a small portion of the earthquakes that took place in earlier centuries and as the determination of the intensities is also unreliable for these periods, only the earthquakes which took place between 1763 and 1984 have been used for constructing the maps. The 111 years between 1763 and 1873 have been denoted as the first epoch and the 111 years between 1874 and 1984 as the second epoch. The maps have been constructed for the entire period, that is for the period from 1763 to 1984, and for both epochs.

The maps have been constructed in the following manner: Let $Q$ be any point in the area studied, $Q_i$ the point indicated in the catalogue as the epicentre of the $i$-th earthquake. Let $d_i$ be the distance $\overline{QQ_i}$, $\sigma_i$ the scattering of the epicentre given in the catalogue—a centrosymmetric normal distribution being assumed. Thus, the epicentre with the probability density

$$P_i(Q) = \frac{1}{2\pi\sigma_i^2} \exp\left(\frac{-d_i^2}{2\sigma_i^2}\right) \tag{1}$$

is located at point $Q$. This position function $P_i$, whose integral over the entire area is 1, constitutes the epicentral density of earthquakes, whereas

$$S_1(Q) = \sum_i P_i(Q) \tag{2}$$

is the epicentral density of all earthquakes. Let $T$ be the investigated period during which the earthquakes have taken place. In this case,

$$s_1(Q) = \frac{1}{T} S_1(Q) \tag{3}$$

| epoch | $s_1$ | $s_M$ | $s_I$ | $s_E$ |
|---|---|---|---|---|
| 1763–1873 | 4 | 3 | 3 | − 14 |
| 1874–1984 | 4 | 3 | 3 | − 13 |
| 1763–1984 | 4 | 4 | 3 | − 14 |

*Table I.* The scaling variable $N$ for various seismic fields

*I. Táblázat* Az $N$ skála változó értéke különböző szeizmikus terekre

*Таблица I.* Переменные значения шкалы $N$ при различных сейсмических полях

is the time-normalized epicentral density or, in other words, the epicentral density flow. Hence, the dimension of $s_1$ is $km^{-2} \cdot a^{-1}$. In addition, a scaling was performed according to which the numbers printed in the maps have to be multiplied by $10^{-N} \cdot N$ is given in *Table I.* The following equation

$$s_g(Q) = \frac{1}{T} \sum_i g_i P_i(Q) \tag{4}$$

is a generalization of $s_1$, with $g_i > 0$. The magnitude $M_i$ of the $i$-th earthquake, which magnitude is always positive in the above catalogue has, for example, been used as $g_i$. The time-normalized magnitude density $s_M(Q)$ thus created causes stronger earthquakes to become more distinctly evident on the map than does the epicentral density $s_1$. The situation is similar with $s_I$, with the epicentral intensity serving as the weighting factor. The dimension and scaling of $s_M$ and $s_I$ are the same as those for $s_1$. In none of the cases was normalization by means of $\sum_i g_i$ used. If the energy of the earthquake is substituted for $g_i$, one obtains the time-normalized energy density $s_E$ with the dimension $erg \cdot km^{-2} \cdot a^{-1}$. The equations developed by BÅTH and DUDA [1964] were used:

$$\log E = 12.24 + 1.44M \tag{5}$$

$$\log V = 9.58 + 1.47M \tag{6}$$

where log is the logarithm to base 10; $E$ the seismic wave energy in erg; $M$ the magnitude, which is equivalent with the Gutenberg–Richter magnitude; and $V$ the earthquake volume in $cm^3$. The last of these is identified with the total aftershock volume. In the computation of $s_E$, $\sigma_i + R$ was substituted for $\sigma_i$, with $R = \sqrt[3]{3/4\pi}\ V$ in km. ULLMANN and MAAZ [1969] have considered in greater detail the computation of seismic fields, while BÅTH [1981] provides an up-to-date survey of problems of the earthquake magnitude. The density functions $s_1$, $s_M$, $s_I$ and $s_E$ have been plotted in an isogram for both epochs and for the overall period from 1763 to 1984 within a polygon with the following vertices:

| | | | | | | | |
|---|---|---|---|---|---|---|---|
| 17 | 20 | 23 | 26 | 26.5 | 22 | 16 | $\lambda$ in degrees longitude east |
| 49 | 49.5 | 49 | 47 | 45.5 | 44.59 | 46.37 | $\varphi$ in degrees latitude north |

On the map plane, the afore-said spherical polygon was mapped with the help of a Lambert's conformal conic projection. This made possible an exact comparison with the International Tectonic Map of Europe [SCHATSKY et al. 1964]. To facilitate comparison with other maps, the network of parallels and meridians was used in our illustrations, and the rivers Danube, Dráva, Tisza and Maros as well as Lake Balaton and the Neusiedler See were drawn with broken lines.

### 3. Seismic fields and comparisons with other geophysical fields

*Figure 1* shows the (time-averaged) density of the seismic epicentres. One can notice an almost linear chain of highs extending approximately WSW–ENE: I located approximately at Csehi to the north of Zalaegerszeg; II Várpalota–Mór; III Dunaharaszti; IV Eger; VII Csap. It is noticeable that this chain of epicentral highs lies directly to the north of the Balaton line on the Bakony–Bükk Unit [BALLA 1984] and also runs parallel to its strike. V Kecskemét, VI Érmellék and VIII Komárom are further significant areas with a high epicentral density. Other highs (e.g. in Slovakia) have not been numbered. The magnitude density in *Fig. 2* shows the afore-said chain of highs even more distinctly: further maxima located on this line are observed in addition to the above five maxima. The question we ask now is to what extent the results depend on the time interval in which the earthquakes took place. Figure 2 shows $s_M$ for the entire period, *Fig. 3* for the second epoch, *Fig. 4* for the first epoch. It can be seen that Fig. 2 is similar to Fig. 3. With regard to Fig. 4, this has been computed only from historical earthquakes taking place between 1763 and 1873, it also shows the afore-said chain of anomalies.

A strongly negative correlation is found between the epicentral density (for the entire period investigated) $s_1$ and the temperature at a depth of 2 km (see *Fig. 5*). $s_1 > 100$ and $T > 120°$ C have been drawn separately. The aforementioned chain of epicentral highs striking WSW–ENE is located at its western and central parts in the cooler region. Likewise, the high IV in the eastern part is located on the temperature low in the Bükk Mts. The seismic high V also lies in a temperature minimum. Obviously, stresses that have seismic effects can more easily build up in cooler, less ductile portions of the crust. This effect is well known from solid-state physics. It is, however, only a supposition that the correlation between the positive epicentral density anomalies and the negative temperature anomalies could be partially explained by it. The largest warm regions in the Pannonian Basin also strike WSW–ENE. They are located on the Mid-Hungarian Belt [see BALLA 1984, p. 319], that is, to the south of the seismic chain of anomalies. This belt is possibly linked to a high position of the

asthenosphere [POSPÍŠIL and VASS 1984, p. 359]. According to a kinematic analysis performed by BALLA [1984], this is the suture between two blocks. The southeastern domains rotated in a clockwise direction by 100°, the northwestern block rotated counter-clockwise by 30°.

Earlier paleomagnetic investigations led to similar conclusions: In the Early Miocene, the Transdanubian Range rotated by 35° in a counter-clockwise direction [MÁRTON and MÁRTON 1983] whereas South Transdanubia rotated by 60° or more in a clockwise direction [MÁRTON 1981]. To the south of Lake Balaton and to the south of Székesfehérvár, the Balaton line is characterized by an electric conductivity anomaly [VARGA 1979, ÁDÁM 1985], alongside which special heat flow anomaly can also be found [DÖVÉNYI et al. 1983]. It constitutes the continuation of the Periadriatic lineament which separates the Southern Alps from the metamorphosed Eastern Alps. The Periadriatic lineament in the Gail valley and in the Karawanken mountains is also characterized by a conductivity anomaly and an increased heat flow [ÁDÁM et al. 1984].

WALZER et al. [1989] studied the correlation between the heat flow and seismic magnitude density in the Pannonian Basin. They also found a negative correlation, which was, however, not quite as distinct as that between the temperature at a depth of 2 km and the epicentral density. Somewhat less recognizable are the correlations between the epicentral density and magnitude density (this work), on the one hand, and the maxima of the horizontal geothermal gradient according to STEGENA [1979], on the other hand. Here, too, there is an anomaly chain, oriented WSW–ENE, which determines the overall picture. But the pronounced seismic anomalies II and VIII are clearly situated outside the maxima of Stegena's map. Anomaly V also lies on a maximum of the map of the geothermal gradient. A relationship between the distributions cannot be denied. If one compares the survey of the most important thermal springs in Mesozoic carbonates [DÖVÉNYI et al. 1983, p. 38] with modern maps of seismic activity (Figs. 1 to 3), it becomes evident that these springs are located without any exception at the edge of seismic highs: Spring regions of 67, 17 and 9 MW at the edge of I, those of 100 and 6 MW at the edge of VIII, a spring region of 35 MW at the edge of III, those of 42 and 20 MW at anomaly IV, a spring region of 15 MW (Harkány) at the edge of an unnumbered magnitude density anomaly in the southern part of Transdanubia.

Whereas there is a very close relationship between regions with a low temperature and earthquake regions, the relationships with the field of gravity are only loose. At any rate, the largest positive regional Bouguer anomalies [MESKÓ 1983], which were obtained by means of a low-pass filter with a cut-off frequency of 20 km and of 45 km, coincide with our seismic anomaly chains I, II, III, IV. The remaining anomalies are not clearly associated with seismic highs. Understandably, the correlation between the negative regional Bouguer anomalies, which were obtained by means of a low-pass filter with a cut-off frequency of 20 km [MESKÓ 1983], and the largest depths of the pre-Tertiary basement [KILÉNYI and RUMPLER 1984] is very close, as can be shown by directly projecting the maps on one another.

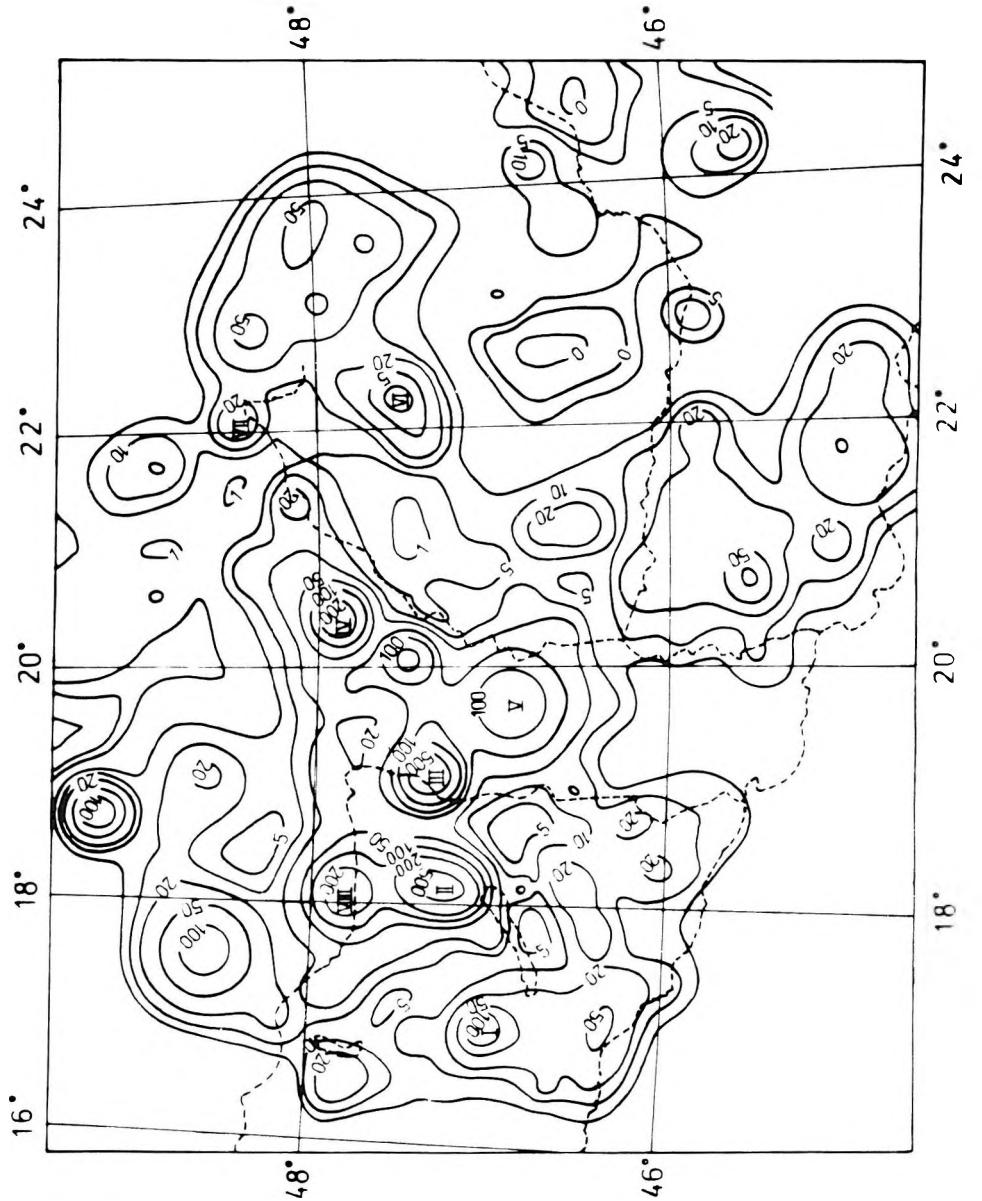


*Fig. 1.* Time-normalized epicentral density $s_1$ for the period 1763–1984

*1. ábra.* Időre normált epicentrum-sűrűség eloszlás $s_1$ az 1763–1984 időszakra

*Рис. 1.* Распределение плотности эпицентров $s_1$, отнесенное ко времени, для периода 1763–1984

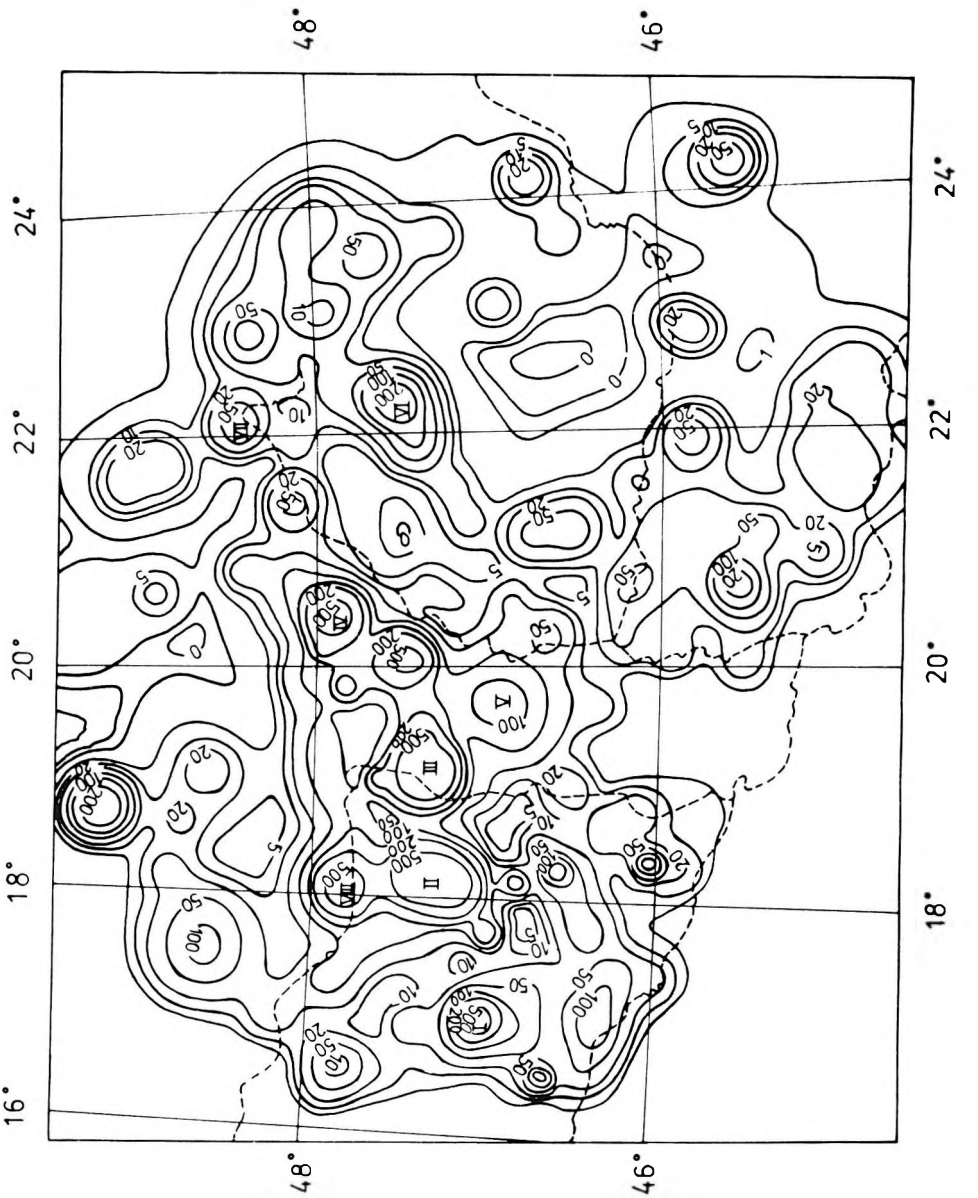


*Fig. 2.* Time-normalized magnitude density $s_M$ for the period 1763–1984

*2. ábra.* Időre normált magnitúdó-sűrűség eloszlás $s_M$ az 1763–1984 időszakra

*Рис. 2.* Распределение плотности магнитуд $s_M$, отнесенное ко времени, для периода 1763–1984

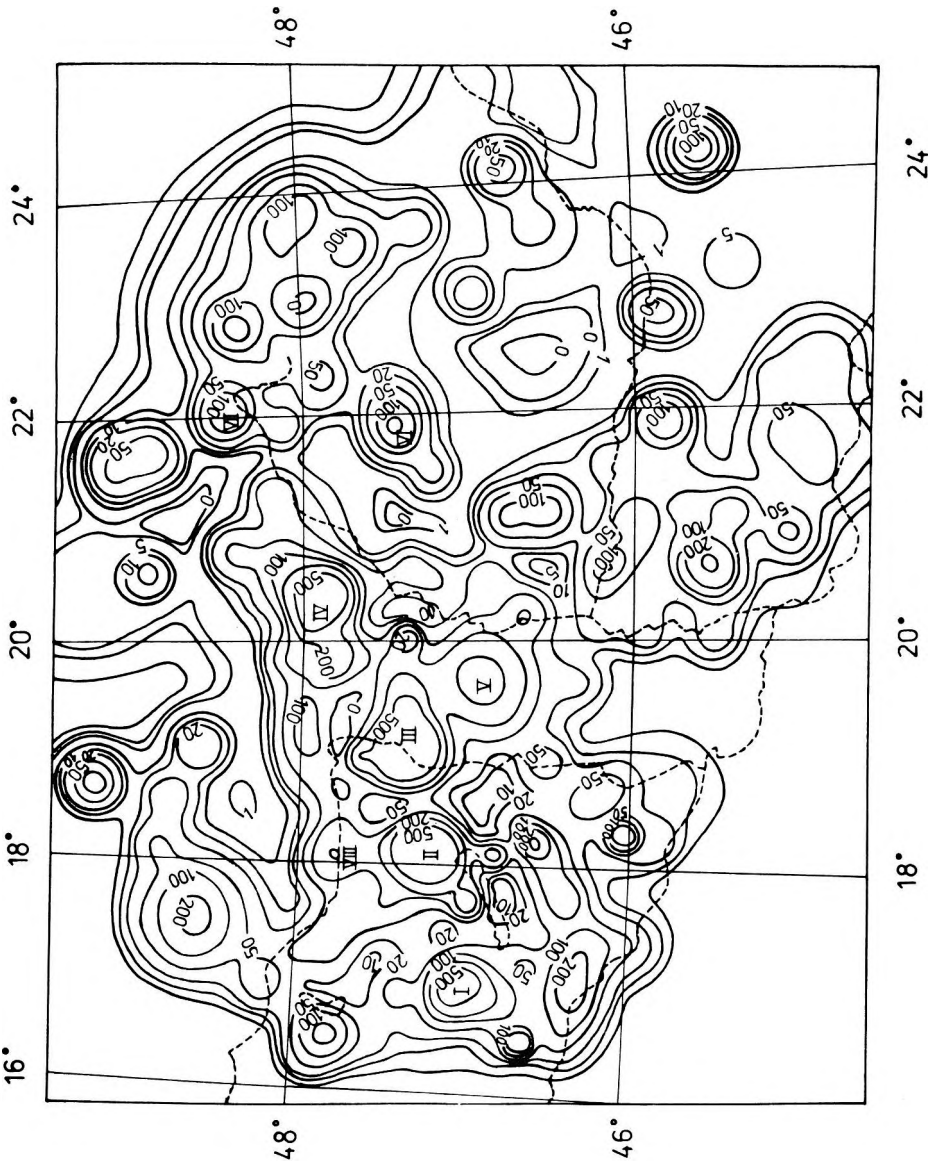


*Fig. 3.* Time-normalized magnitude density $s_M$ for the second epoch (1874–1984)

*3. ábra.* Időre normált magnitúdó-sűrűség eloszlás $s_M$ a második vizsgált időszakra (1874–1984)

*Рис. 3.* Распределение плотности магнитуд $s_M$, отнесенное ко времени, для второго периода (1874–1984)

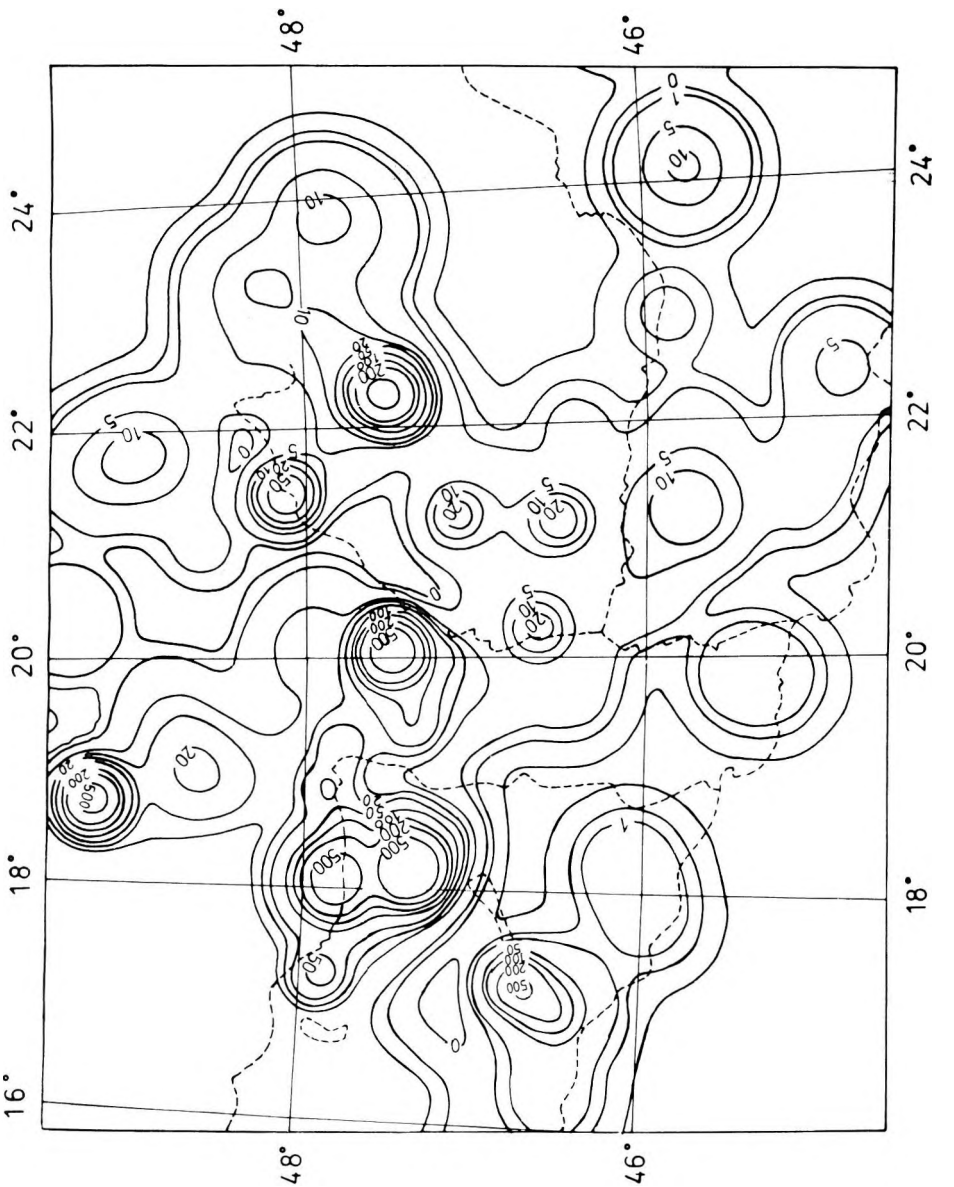


*Fig. 4.* Time-normalized magnitude density $s_M$ for the first epoch (1763–1873)

*4. ábra.* Időre normált magnitúdó-sűrűség eloszlás $s_M$ az első vizsgált időszakra (1763–1873)

*Рис. 4.* Распределение плотности магнитуд $s_M$, отнесенное ко времени, для первого периода (1763–1873)

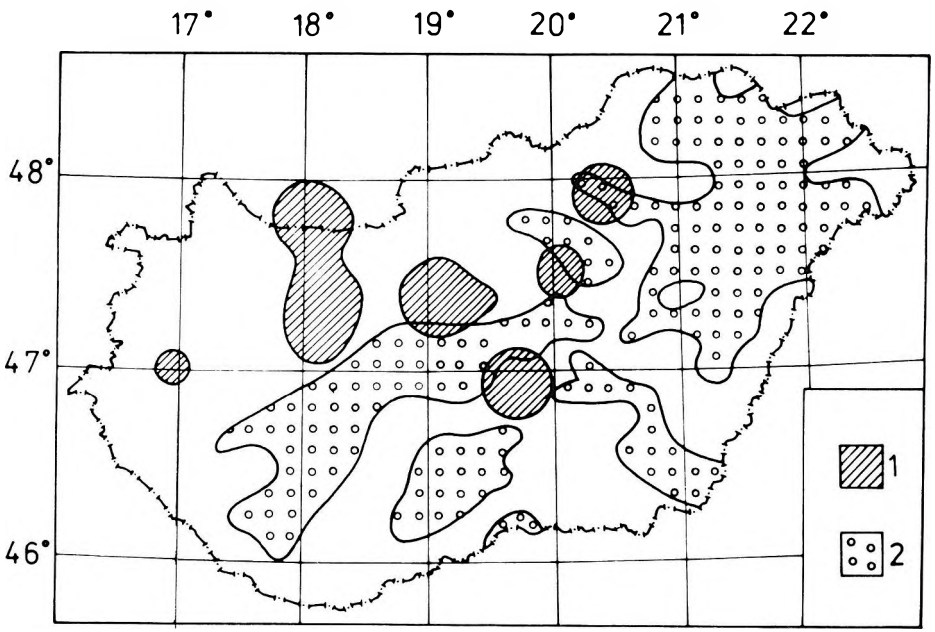


*Fig. 5.* Comparison of regions with high epicentral density $s_1$ with regions of high temperature. It can be seen that the seismic activity occurs preferably in those regions of the Pannonian Basin which are less hot
1—$s_1 > 100$ for earthquakes between 1763 and 1984; 2—$T > 120$°C at 2 km below the surface [DÖVÉNYI et al. 1983, p. 14]

*5. ábra.* A nagy $s_1$ epicentrum-sűrűségű területek összehasonlítása nagy hőmérsékletű területekkel. Látható, hogy a szeizmikus aktivitás főként a Pannon medence kevésbé meleg területein jelentkezik
1 — $s_1 > 100$ területei az 1763 és 1984 közötti földrengésekre; 2— $T > 120$ °C, a felszín alatt 2 km mélységben. [DÖVÉNYI et al. 1983]

*Рис. 5.* Сопоставление районов с высокой плотностью эпицентров $s_1$ с районами высоких температур. Можно заметить, что сейсмичность приурочена ва основном к менее нагретым районам Паннонской впадины
1—районы $s_1 > 100$ по землетрясениям 1763–1984 гг.; 2—$T > 120$ °C на глубине 2 км [DÖVÉNYI et al. 1983]

It is remarkable that the chain of positive anomalies with the WSW–ENE orientation is very pronounced on our epicentral and magnitude density maps, while the same cannot be said of the published maximum intensity maps. Whereas the positive anomalies V, II, VIII and IV (in this order) are the most important ones on the maximum intensity map of SIMON [1930]; V, VIII and, to a lesser extent, IV and III are dominant in BISZTRICSÁNY et al. [1961]. In ZSÍROS and MÓNUS [1984, p. 442], V and III are dominant. These differences are certainly due to a varying degree of the completeness of the material as well as to different methods used.

## REFERENCES


ÁDÁM A. 1985: Electric conductivity increases in the earth's crust in Transdanubia (W-Hungary). Acta Geodaet., Geophys. et Montanist. Hung. **20,** 1, pp. 173–182

ÁDÁM A., DUMA G., GUTDEUTSCH R., VERŐ J., WALLNER Á. 1984: The research of the Periadriatic lineament by magnetotellurics. Magyar Geofizika, **25,** 4, pp. 136–150

BALLA Z. 1984: The Carpathian loop and the Pannonian Basin: A kinematic analysis. Geophysical Transactions, **30,** 4, pp. 313–353

BÅTH M. 1981: Earthquake magnitude—Recent research and current trends. Earth-Sci. Rev. **17,** 4, pp. 315–398

BÅTH M., DUDA S. J. 1964: Earthquake volume, fault plane area, seismic energy, strain, deformation and related quantities. Annali di Geofisica **17,** 3, pp. 353–368

BISZTRICSÁNY E., CSOMOR D., KISS Z. 1961: Earthquake zones in Hungary. Annales Univ. Sci. Budapest, Sec. Geol. **4,** pp. 35–38

DÖVÉNYI P., HORVÁTH F., LIEBE P., GÁLFI J., ERKI I. 1983: Geothermal conditions of Hungary. Geophysical Transactions **29,** 1, pp. 3–114

KILÉNYI É., RUMPLER J. 1984: Pre-Tertiary basement relief map of Hungary. Geophysical Transactions, **30,** 4, pp. 425–428

MÁRTON E. 1981: Tectonic implication of palaeomagnetic data for the Carpatho-Pannonian Region. Earth Evol. Sci. **1,** 257–264

MÁRTON E., MÁRTON P. 1983: A refined apparent polar wander curve for the Transdanubian Central Mountains and its bearing on the Mediterranean history. Tectonophysics **98,** 1/2, pp. 43–57

MESKÓ A. 1983: Regional Bouguer gravity maps of Hungary. Acta Geodaet., Geophys. et Montanist. Hung. **18,** 1–2, pp. 187–200

POSPÍŠIL L., VASS D. 1984: Influence of the structure of the lithosphere on the formation and development of intramontane and back molasse basins of the Carpathian Mountains. Geophysical Transactions **30,** 4. Bp. 355–371

RÉTHLY A. 1952: Earthquakes in the Carpathian Basins between 455 and 1918 (in Hungarian), Akadémiai Kiadó, Budapest, 510 p.

SCHATSKY N., STILLE H., BOGDANOFF A., BLONDEL F. (Eds.) 1964: Congrès Géologique International, Commission de la Carte Géologique du Monde, Sous-Commission de la Carte Tectonique du Monde, Carte Tectonique Internationale de l'Europe, Échelle 1 : 250.000, Moscou

SIMON B. 1930: Die Erdbebentätigkeit des Ungarischen Beckens. Veröff. Reichsanstalt für Erdbebenforschung Jena **40,** pp. 80–84

SPONHEUER W. 1960: Methoden zur Herdtiefenbestimmung in der Makroseismik. Freiberger Forschungshefte **C 88,** pp. 1–117

SPONHEUER W. 1965: Bericht über die Weiterentwicklung der seismischen Skala. Veröff. Inst. Geodynamik Jena **8,** pp. 1–21

STEGENA L. 1979: Geothermics and seismicity in the Pannonian Basin. In: Terrestrial and Space Techniques in Earthquake Prediction Research, A Vogel ed. Vieweg, Braunschweig, pp. 467–471

ULLMANN V., MAAZ R. 1969: Prolegomena zur Seismizität, Teil I. Veröff. Inst. Geodynamik Jena **13,** pp. 104–118

VARGA G. 1979: Geophysical investigations of geological profiles I. Report of the telluric and magnetotelluric measurements in 1979. Manuscript, 10 p.

WALZER U., MAAZ R., TÓTH L. 1989: Seismotectonics of the Pannonian Basin. In: Critical aspects of the plate tectonics Theory. Theophrastus Publ. S. A. Athens

WILLMORE P. L. (Ed.) 1979: Manual of seismological observatory practice. World Data Center A for Solid Earth Geophysics, Report SE-20, Boulder, Colorado

ZSÍROS T., MÓNUS P. 1984: An estimation of maximum ground motions caused by earthquakes in Hungary. Acta Geodaet., Geophys. et Montanist. Hung. **19,** pp. 433–449

ZSÍROS T., MÓNUS P., TÓTH L. 1988: Hungarian Earthquake Catalogue from 456 to 1987. Published by the GGKI, Hung. Acad. of Sciences, Sopron, 175 p.

## A PANNON MEDENCE SZEIZMIKUS AKTIVITÁSA ÉS EGYÉB GEOFIZIKAI MÉRÉSEKKEL VALÓ ÖSSZEHASONLÍTÁSA

Uwe WALZER, Richard MAAZ és TÓTH László

A Pannon medencében 1763 és 1984 közt kipattant földrengések adataiból számítógépes szeizmicitás térképet szerkesztettünk. A medence NyDNy–KÉK csapású tektonikai egységei szoros kapcsolatot mutatnak az epicentrum-sűrűség és magnitúdó-sűrűség izovonalaival. Az említett szeizmikus térképek maximumait 2 km mélységben felvett hőmérséklettérképek minimumaival korreláltuk. Az epicentrum- és magnitúdó-sűrűség maximumok eloszlása a hőáram minimumokkal is összefüggést mutat, és valamivel lazább kapcsolatot a horizontális geotermális gradiens maximumokkal, valamint a pozitív regionális Bouguer anomáliákkal.

## СЕЙСМИЧНОСТЬ ПАННОНСКОЙ ВПАДИНЫ В СОПОСТАВЛЕНИИ С ДРУГИМИ ГЕОФИЗИЧЕСКИМИ ДАННЫМИ

Уве ВАЛЬЦЕР, Рихард МАЦ и Ласло ТОТ

По данным землетрясений, имевших место в Паннонской впадине за период 1763–1984 гг., с помощью ЭВМ составлена карта сейсмичности. Тектонические единицы ЗЮЗ–ВСВ простирания в Паннонской впадине обнаруживают тесную связь с изолиниями плотности эпицентров и магнитуд. Максимумы на этой карте сейсмичности скоррелированы с минимумами на картах температур на глубине 2 км. Распределение максимумов плотности эпицентров и магнитуд обнаруживает связь также и с минимумами теплового потока, и несколько более слабую — с максимумами горизонтальных геотермических градиентов, а также с положительными региональными аномалиями Буге.

GEOPHYSICAL TRANSACTIONS 1988
Vol. 34. No. 4. pp. 295–307

# THE STATISTICAL PROPERTIES OF PALAEOMAGNETIC POLARITY–TIME SCALES

János MITNYIK*

The aim of the statistical investigation of the palaeomagnetic polarity–time scales is to get information about the average behaviour of the reversals in time, and to utilize these to construct models in which the same statistical properties are reflected. The principal problem associated with this objective was the description of the average behaviour in time. After the examination of the newest polarity–time scales we concluded the following:

— the polarity intervals show a non-stationarity which can be approached by linear regression;
— a gamma distribution is shown by the polarity intervals; the parameters of the distribution had changed during the Earth's history;
— the independence of the polarity intervals cannot be investigated with the recent mathematical statistical methods, but it can be proved analytically (if some conditions are fulfilled);
— the stability of the geomagnetic field is the same for the two polarity states: the question is, how the polarity bias is connected with the processes which cause the change of the $\lambda$ parameter of the gamma distribution.

**Keywords: polarity–time scales, polarity intervals, nonstationarity, gamma distribution, paleomagnetism**

## 1. Introduction

It is well-known that the dipole moment of the geomagnetic field has changed polarity many times in the Earth's history. This is not unique in the Universe; the Sun and some other stars change their polarity periodically. At the moment the dipole moment of the Earth is decreasing rapidly. If this decrease continues unchanged then the dipole moment of the magnetic field will vanish within 1000 years. In order to obtain information about the polarity changes, we have to initially investigate the marine magnetic anomalies. In this way, polarity–time scales can be made with a retrospective effect, as from the age of the oldest marine crust. The first polarity–time scale was made at the beginning of the 60's. Lacking the convenient divisions, these timescales were not suitable for statistical investigations. The first timescale which was sufficently long (from 0 to 80 million years), was produced by HEIRTZLER et al. in 1968. Naturally, its statistical analysis began concurrently. The timescales used in this text are by HEIRTZLER et al. [1968] (referred to hereafter as HDHPL–68) and NESS et al. [1980] (referred to hereafter as NLC–80).

* Eötvös Loránd Geophysical Institute of Hungary, POB 35, Budapest, H–1440, Hungary
Manuscript received (revised version): 3 March, 1988

The change of magnetic polarity from one stable polarity state to the other is called *polarity transition*. Plotting the normal and reversed polarity intervals against time, we get a *polarity–time scale (Fig. 1)*. The square-like wave illustrates that the polarity changes are momentary. If we investigate the statistical properties of the timescales, we have to assume that a polarity change can occur in an instant. It is acceptable to assume this because the length of the polarity intervals are in hundreds of thousands years, while a polarity change has as a length a multiple of ten thousand years. Futher on, let us see a sufficiently extensive time period with long equidistant samples. Let us determine the original polarity state of the samples. The proportion of samples with normal polarity state to those with reversed polarity state shows the time the field has spent in normal state. This is called the *polarity quotient,* (usually given in percent). *Fig. 2* shows the changing value of the polarity function plotted against geological time [IRVING and PULLAIAH 1976]. When the polarity quotient is near 50%, then the field oscillates considerably. However when its value is high (90%) or low (10%) for a long period, then no, or only a few reversals occur. Connected with these long intervals some further terms can be defined. When the field has dominantly normal polarization, it is called *normal polarity bias* and when the field is reversed dominantly, it is the *reversed polarity bias.*

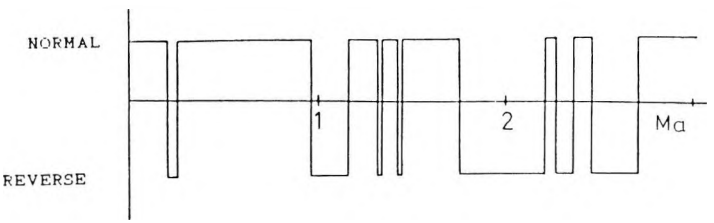


*Fig. 1.* Polarity–time scale for the last few million years

*1. ábra.* Polaritás–idő skála az elmúlt néhány millió évre

*Рис. 1.* Шкала полярность–время для последних нескольких млн. лет

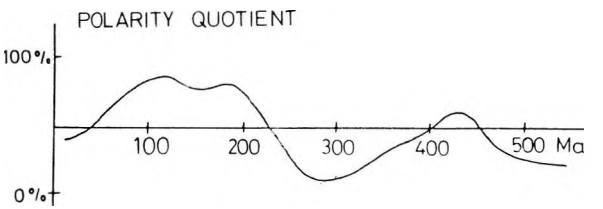


*Fig. 2.* The change of the polarity quotient as a function of time [after IRVING and PULLAIAH 1976]

*2. ábra.* A polaritáshányados változása a geológiai idő függvényében [IRVING és PULLAIAH 1976 nyomán]

*Рис. 2.* Изменение доли полярности как функция геологического времени [по IRVING and PULLAIAH 1976]

The dates of the polarity transitions are given by the polarity–time scales. The time between two succesive polarity transitions is called the "polarity interval". This polarity interval series can be made for the whole time scale. It is not the polarity–time scales which are investigated directly, but the polarity interval series, which were produced from them.

## 2. The analysis of the polarity intervals

In the mathematical sense, the polarity intervals form a time series. Consequently the polarity intervals can be analysed using time series analysis, $X_t$ ($t = 1, 2, \ldots$) representing the polarity intervals from the present to the past.

### *2.1 The stationarity of the polarity intervals*

Assume that $X_t$ polarity intervals ($t = 1, 2 \ldots$) form a stochastic process, which consists of three parts:

$$X_t = \varphi_t + d_t + Y_t \quad (t = 1, 2 \ldots) \tag{1}$$

where $\Phi_t$ is the trend, $d_t$ is a periodical function and $Y_t$ is a stationary time series. Further on, we assume that the periodical component is equal to zero [PHILLIPS and COX 1976 and LUTZ 1985]. Consequently, only trend and stochastic components are contained in our time series.

The first to try to determine the trend with the moving average method was NAIDU [1971], who analysed the HDHPL–68 timescale. He had investigated the changeability of the mean and the variance of the intervals in independent, 8 million year long, windows. The mean and the variance was found constant between 0 and 48 million and between 56 and 72 million years, while a discontinuity was found between 48 and 56 million years. The same was found by PHILLIPS et al. [1975] and PHILLIPS [1977], when they investigated the same timescale using the moving average method. *Fig. 3* shows the moving average of the HDHPL–68 timescale with 95% confidence intervals. (Normal distribution was assumed for the polarity intervals, when the confidence intervals were constructed—this is valid when the sample is large.) The HDHPL–68 timescale shows an almost constant behaviour between 0 and 40 and between 50 and 65 million years. The moving average of the NLC–80 timescale is shown in *Fig. 4*. A linear trend can clearly be seen. Other timescales—not demonstrated here—show similar properties: the moving average of the timescales made before 1974 are similar to the moving average of the HDHPL–68 and the moving average of the timescales since 1974 are also similar to the NLC–80 timescale. Perhaps the reason for the difference is the better definition of the new time scales. It must be said that the series of the trend values, so determined, gives a rough picture about the phenomenon in time. We cannot use it for a more

complete analysis or for forecasting. For these aims, the trend must be determined as an analytical function of time [ÉLTETŐ et al. 1982]. After this a linear trend is fitted for different ranges of some time scales. Let us assume that the time series has the next form:

$$X_t = at + b \quad (t = 1, 2 \ldots) \tag{2}$$

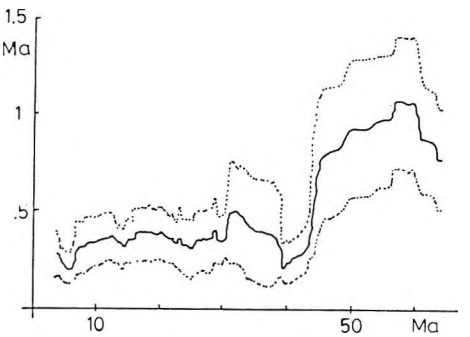


*Fig. 3.* The moving average of the HDHPL–68 timescale. Sliding window includes 20 intervals of each polarity and shifts by one interval of each polarity each time. The dashed lines show the 95% confidence interval

*3. ábra.* A HDHPL–68 időskála 20 intervallumon keresztül végzett mozgó átlagolás után. A szaggatott vonalak a 95%-os konfidencia-intervallumok

*Рис. 3.* Шкала HDHPL–68 после скользящего усреднения по 20 интервалам. Прерывистые линии – 95%-ные интервалы доверия

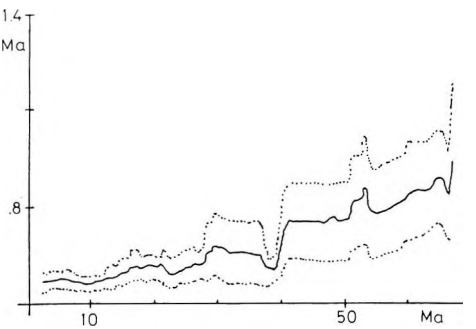


*Fig. 4.* The moving average of the NLC–80 timescale. Sliding window includes 20 intervals of each polarity and shifts by one interval of each polarity each time. The dashed lines show the 95% confidence interval

*4. ábra.* Az NLC–80 időskála 20 intervallumon keresztül végzett mozgó átlagolás után. A szaggatott vonalak a 95%-os konfidencia-intervallumok

*Рис. 4.* Шкала NLC–68 после скользящего усреднения по 20 интервалам. Прерывистые линии – 95%-ный интервал доверия

The results by the least square method are shown in *Table I.* It can be seen from the data that the trend changes at around 40 million years, and becomes steeper by one order between 40 and 80 million years. McFADDEN [1984] also investigated the nonstationarity of the time scales. We shall deal with this in the chapter on the distribution of polarity intervals.

If the trend is subtracted from the original time series, we shall get the stationary random component. *AR, MA* or *ARMA* models can be fitted for this. But, we shall see later that data for the time series do not exhibit the same distribution function. Therefore if we fit a stochastic model it will be impossible to interpret. At present the application of these stochastic models may only be done if the data for the stochastic process show the same distribution.

We can conclude the following: non-stationary behaviour is shown by the newest timescales. The moving average method is not a perfect test for stationarity, because it gives little independent information about the data set. For example if we have 100 samples and use a moving window with 25 data, we shall get only 4 independent data items for the time series. This problem—as we shall see in the next chapter—was solved by McFADDEN [1984] using the maximum likelihood principle.

| TIMESCALE | INTERVAL[Ma] | $a$ | $b$ |
|---|---|---|---|
| HDHPL–68 | 0–40 | $8.73 \cdot 10^{-4}$ | 0.28 |
| HDHPL–68 | 0–72 | $3.14 \cdot 10^{-3}$ | 0.17 |
| NLC–80 | 0–40 | $1.58 \cdot 10^{-3}$ | 0.15 |
| NLC–80 | 40–80 | $2.1 \cdot 10^{-2}$ | 0.38 |
| NLC–80 | 0–80 | $4.52 \cdot 10^{-3}$ | −0.02 |
| LA–81 | 0–80 | $3.25 \cdot 10^{-3}$ | 0.13 |

*Table I.* The linear trends which were fitted to some different parts of some timescales ($X_t = at + b$)

*I. táblázat.* Néhány időskála különböző tartományaira illesztett lineáris trend ($X_t = at + b$)

*Таблица 1.* Линейный тренд ($X_t = at + b$) различных интервалов некоторых шкал времени

## *2.2 The distribution of the polarity intervals*

If rough histograms of the length of the polarity intervals were made, we could see that the exponential distribution fits very well *(Fig. 5)*. However, using a finer scale, the histogram changes according to *Fig. 6*. On the basis of this, NAIDU [1971] generalized the exponential distribution into the gamma distribution. However, whether exponential or gamma distributions describe the polarity intervals, only a gamma distribution can be observed, because there are a lot of undetected polarity changes, which thin the original process.

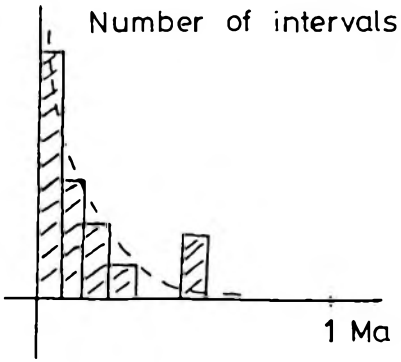


*Fig. 5.* The distribution function of polarity intervals, with rough division. The exponential distribution fits well

*5. ábra.* A polaritás-intervallumok gyakorisági görbéje, durva felbontásban. Az exponenciális eloszlás jól illik rá

*Рис. 5.* Гистограмма интервалов постоянной полярности при грубом разрешении. Достаточно хорошо описывается експоненциальным распределением

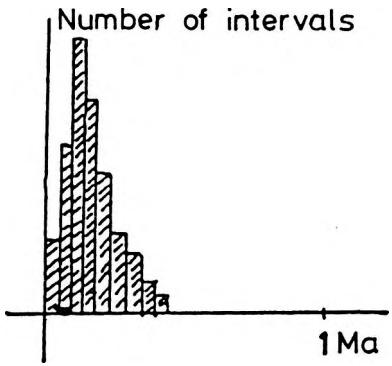


*Fig. 6.* The distribution function of polarity intervals, with fine division. The gamma distribution fits well

*6. ábra.* A polaritás-intervallumok gyakorisági görbéje nagyobb felbontásban. A gamma-eloszlás jól illik rá

*Рис. 6.* Гистограмма интервалов постоянной полярности при большем разрешении. Хорошо описывается гамма-распределением

Let us determine the parameters of the supposed distribution. The maximum likelihood estimation, suggested by Cox and Lewis [1966], was made unbiased by McFadden [1984] for the two parameters of the gamma distribution. The PDF (probability density function) of the gamma distribution is

$$f(x) = \frac{1}{\Gamma(k)} \lambda(\lambda x)^{k-1} e^{-\lambda x} \tag{3}$$

where $x>=0$, $\lambda$, $k \in R^+$, $\Gamma(k)$ the gamma function. The mean is

$$\mu = \frac{k}{\lambda} \tag{4}$$

For this reason we may turn to $\mu = k/\lambda$ parameter instead of $\lambda$. The maximum likelihood estimations of $\mu$ and $k$ and their variance are:

$$\hat{\mu} = \frac{1}{N}\sum_{i=1}^{N} x_i \qquad \text{var}(\hat{\mu}) = \frac{\hat{\mu}^2}{N\hat{k}} \tag{5}$$

$$\ln \hat{k} - \psi(\hat{k}) = \frac{N}{N-1} \ln \hat{\mu} - \frac{1}{N-1}\sum_{i=1}^{N} \ln x_i$$

$$\text{var}(\ln \hat{k}) = \frac{1}{N\hat{k}^2\left[\psi'(\hat{k}) - \frac{1}{\hat{k}}\right]} \tag{6}$$

where $\psi(k)$ is the digamma function, $\psi'(k)$ is the trigamma function [ABRAMOVITZ and STEGUN 1970].

The $\hat{k}$ parameter can not be expressed in an explicit way because $\psi(k)$ is not an analytical function. Therefore we have to approximate it numerically. So, can we estimate the $\mu$ and $k$ parameters independently? Yes, because the covariance matrix is diagonal with regard to $\mu$ and $k$. Therefore there is no correlation between them. Let us assume after this that $k$ and $\lambda$ can change in time, and let us calculate the change of $\hat{k}$ and $\hat{\lambda}$ in time, in 8 million-year-long disjunct intervals *(Fig. 7)*. It can be seen that $\hat{k}$ is approximately constant, while $\hat{\lambda}$ decreases linearly between 0 and 80 million years and it increases almost linearly between 120 and 160 million years.

After this let us handle separately the normal and reverse polarity intervals. MCFADDEN [1984] proved that there is no reason to reject the hypothesis that the value of $\hat{k}$ and $\hat{\lambda}$ are the same for both polarity states. (This assertion will be taken into account in the chapter which deals with the stability of the polarity states.) The change in time of the $\hat{k}$ and $\hat{\lambda}$ parameters for both polarity states is very similar to that shown in Figure 7.

Let us return to the investigation of non-stationarity, mentioned by MCFADDEN [1984]. The $\lambda$ parameter can be replaced with a linear trend

$$\lambda = \alpha + \beta t \tag{6}$$

in equation (3), and the value of $\hat{k}$, $\hat{\alpha}$, $\hat{\beta}$ were determined by the maximum likelihood method. It is obvious, that the non-stationary nature was described here in an analytical way without the moving average method and all data were used in the computations. In conclusion we can say that the observed polarity intervals show gamma distribution, and that its two parameters ($k$ and $\lambda$) have changed in geological history.

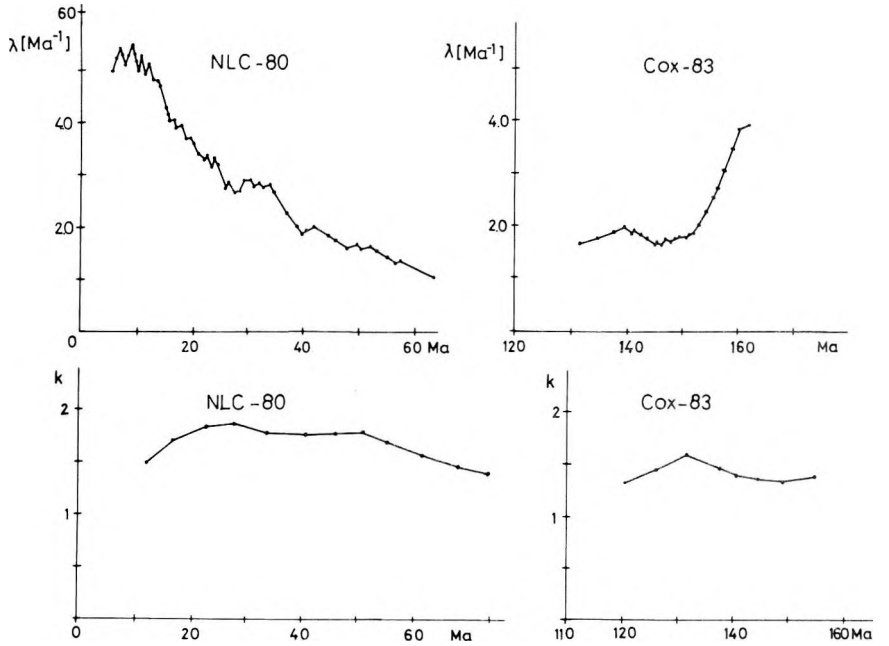


*Fig. 7.* The change of $\lambda$ and $k$ in time for the NLC–80 (from 0 to 80 million years) and for the Cox–83 (from 120 to 160 million years) timescales [McFadden and Merrill 1984]

*7. ábra.* $\lambda$ és $k$ időbeli változása az NLC–80 (0–80 millió év) és a Cox–83 (120–160 millió év) időskálára [McFadden and Merrill 1984]

*Рис. 7.* Изменение $\lambda$ и $\kappa$ во времени по шкалам NLC–80 (0–80 млн. лет) и Cox–83 (120–160 млн. лет) [McFadden and Merrill 1984]

### *2.3 The independence of the polarity intervals*

A very important question in the statistical investigation of time series is whether or not the time intervals between the polarity reversals are independent. First Naidu [1974, 1975] made tests for the independence. The autocorrelation function of the polarity intervals was constructed for the HDHPL–68 timescale from 0 to 72 million years *(Fig. 8)*. It can be seen that the autocorrelation function significantly differs from the autocorrelation function of the white noise. Therefore the independence can be rejected. The idea of Naidu was correct, but as has been shown by Ulrych and Clayton [1976], the autocorrelation analysis can be used only when the process is stationary. Therefore the autocorrelation function was made for the HDHPL–68 timescale from 0 to 48 million years. We can assume the stationarity for this time interval as per chapter 2.1. As *Fig. 9* shows, we can accept the independence of the intervals

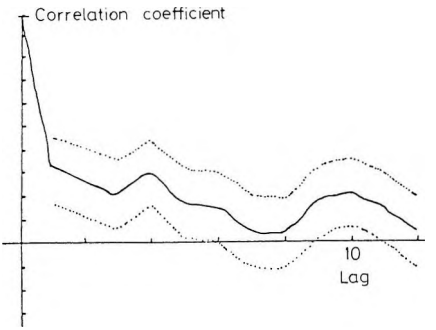


*Fig. 8.* The autocorrelation function for the whole HDHPL–68 timescale. The dashed lines show the 95% confidence interval [after ULRYCH and CLAYTON 1976]

*8. ábra.* A HDHPL–68 időskála autokorrelációs függvénye a teljes időskálára. A vízszintes tengelyen az eltolás, a függőleges tengelyen a korrelációs együttható látható. A pontozott vonal a 95%-os konfidencia-intervallumot jelöli [ULRYCH and CLAYTON 1976 nyomán]

*Рис. 8.* Функция автокорреляции временной шкалы HDHPL–68 по всей шкале времен. На горизонтальную ось нанесены смещения, а на вертикальную – коэффициенты корреляций. Пунктирной линией обозначен 95%-ный интервал доверия [по ULRYCH and CLAYTON 1976]

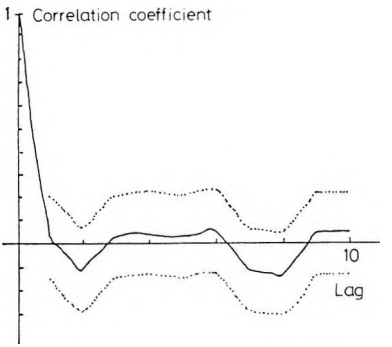


*Fig. 9.* The autocorrelation function for the HDHPL–68 timescale from 0 to 40 million years. The dashed lines show the 95% confidence interval [after ULRYCH and CLAYTON 1976]

*9. ábra.* A HDHPL–68 időskála autokorrelációs függvénye a 0–40 millió éves időszakra. A vízszintes tengelyen az eltolás, a függőleges tengelyen a korrelációs együttható látható. A pontozott vonal a 95%-os konfidencia-intervallumot jelöli [ULRYCH and CLAYTON 1976 nyomán]

*Рис. 9.* Функция автокорреляции временной шкалы HDHPL–68 по интервалу времени 0–40 млн. лет. На горизонтальную ось нанесены смещения, а на вертикальную – коэффициенты корреляций. Пунктирной линией обозначен 95%-ный интервал доверия [по ULRYCH and CLAYTON 1976]

for a 95% confidence limit. In his reply, NAIDU [1976] admitted the validity of ULRYCH and CLAYTON's result, but maintained that the polarity intervals are not independent between 48 and 72 million years. Practically the same investigation was made by PHILLIPS et al. [1975]. They concluded that for the stationary time intervals from 0 to 45 and from 45 to 76 million years, the intervals are independent. LAJ et al. [1979] found the same result for the whole HDHPL–68 timescale, with another method of building the autocorrelation function. It will be worth investigating why the discontinuity does not appear around 48 million years. We can see that the newer timescales are not stationary (therefore autocorrelation analysis cannot be carried out on them). Furthermore the samples do not originate from the same distribution, consequently statistical tests for the independence cannot be carried out on them (for example difference-test [MESZÉNA and ZIERMANN 1981]), because these tests assume that the samples originate from the same distribution. Consequently we can say nothing about the independence of the polarity intervals with the mentioned methods.

However we can say something about the independence in an analytical way. The sequence of ideas was suggested by MCFADDEN in private communication. For simplicity let us assume that the reversals are generated by a Poisson–process. Therefore the probability $P(t)$ that a reversal will happen in the interval $[t, t+dt]$ is:

$$P(t)\,\mathrm{d}t = \lambda \cdot \mathrm{e}^{-\lambda t}\,\mathrm{d}t \tag{7}$$

Further, let us assume that the $\lambda$ is a function of time, for example: $\lambda = \alpha + \beta t$. Let us start from time $t=0$, and wait for the first reversal, which will have happened in $t_1$ time moment. On the basis of equation (7) the probability density function relating to $t_1$ time moment is:

$$P(t_1) = \alpha \cdot e^{-\alpha t_1} \tag{8}$$

The probability density function for the next interval length $t_2$ upon condition $t_1$ is given by

$$P(t_2 | t_1) = (\alpha + \beta t_1) \exp\{-(\alpha + \beta t_1) t_2\} \tag{9}$$

It is obvious, that we can not get rid of $t_1$ in equation (9), since interval $t_2$ will depend on the previous $t_1$ interval. Thus the intervals are not independent.

### 3. The stability of the polarity states

To determine the stability of the polarity states we shall provide an equation which gives the probability of the next reversal as a function of the passed time from the previous reversal. Therefore we have to consider that the elements of the time series do not originate from the same distribution, namely $k$ and $\lambda$ change with time. Let us assume an event (for example normal polarity state)

which is in process at the time $t_0$. What is the probability that the event will be over before $t_0 + t$? (i.e. will a polarity change happen?) *(Fig. 10)*.

$$P(x \leqq t_0 + t \mid x \geqq t_0) = ?$$

where $X$ is the length of the polarity interval. After a simple calculation:

$$P(x \leqq t_0 + t \mid x \geqq t_0) = \frac{\gamma[\lambda(t_0 + t), k] - \gamma[\lambda t_0, k]}{1 - \gamma[\lambda t_0, k]} \tag{10}$$

where $\gamma[\lambda, k]$ is the incomplete gamma function [HARTER 1964]. Let us call this probability the *probability of reversals*. Let us choose $t_0$, that "first" time moment which will follow after a reversal with an infinitesimal time, and let us describe the probability of reversals for different geological dates with the help of the values $\lambda$ and $k$, which can be seen on Fig. 7 *(Fig. 11)*. It can be seen that

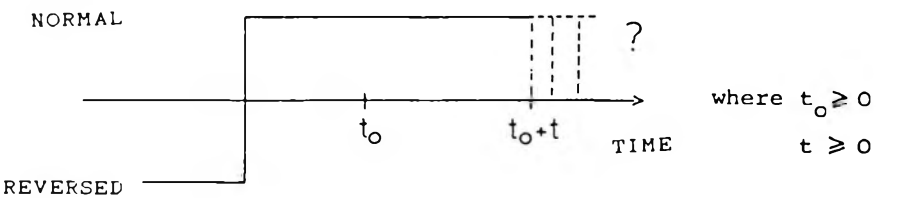


*Fig. 10.* A description of the polarity change

*10. ábra.* Polaritásváltás

*Рис. 10.* Перемена полярности

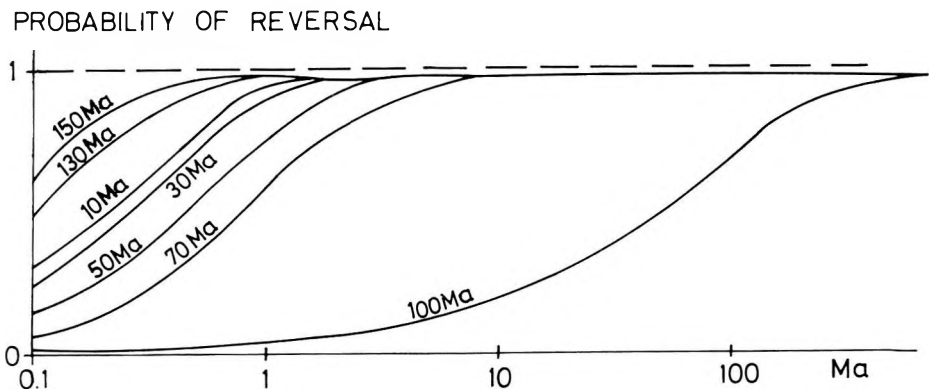


*Fig. 11.* The change of the probability of reversals with time, for different geological dates

*11. ábra.* A térfordulási valószínűségek alakulása az időben, különböző geológiai időpontokban

*Рис. 11.* Изменение вероятности перемены полярностей во времени для различных моментов геологического времени

until the Cretaceous Normal Interval (between 80 and 120 million years) the rate of increase of the probability of reversals decreases, and after the Cretaceous Normal Interval it starts to increase quickly (see Fig. 11). On the basis of this we can understand, in a qualitative way, the existence of the long intervals with the same polarity, because, if $\lambda$ approaches zero, the mean length of the polarity intervals will become infinite. It may also be assumed that it is by chance as to what kind of polarity will be a long polarity interval. Since according to chapter 2.2, the value of $k$ and $\lambda$ are the same for both polarity states, the probability of reversals (or the stability of the two polarity states) are also the same.

Some remarks about the polarity bias. Until now, this problem was connected with the question of the difference in stability between normal and reverse polarity states [PHILLIPS 1977]. If the stability of the two polarity states are the same, then the phenomena is due entirely to other reasons, and will not be valid for the models connected with this (e.g. the models of Cox [1981]). On the basis of these calculations, the question of the polarity bias is connected with those processes which cause the change of the $\lambda$ parameter of the gamma distribution.

## REFERENCES

ABRAMOVITZ N. and STEGUN I. A. 1970: Handbook of mathematical functions with formulas, graphs and mathematical tables. Dover Pub., New York, 1046 p.

COX A. 1981: A stochastic approach towards understanding the frequency and polarity bias of geomagnetic reversals. Phys. Earth Plan. Int. **24,** 2–3, pp. 178–190

COX D. R. and LEWIS P. A. W. 1966: The statistical analysis of series of events. Methuen Co., London, 285 p.

ÉLTETŐ Ö., MESZÉNA GY., ZIERMANN M. 1982: Stochastic methods and models (in Hungarian). Közgazdasági és Jogi Könyvkiadó, Budapest, 420 p.

HARTER L. 1964: New tables of the incomplete gamma-functions and of percent points of the chi- and beta-distribution. Aerospace Research Laboratories, US Air Force, 245 p.

HEIRTZLER J. R., DICKSON G. O., HERRON E. M., PITMAN W. C., LE PICHON X. 1968: Marine magnetic anomalies, geomagnetic field reversals and motion of the ocean floor and continents. J. Geophys. Res., **73,** 6, pp. 2119–2136

IRVING E. and PULLAIAH G. 1976: Reversals of the geomagnetic field, magnetostratigraphy and relative magnitude of paleosecular variation in the Phanerozoic. Earth Sci. Rev. **12,** 1, pp. 35–64

LAJ C., NORDEMANN D., POMEAU Y. 1979: Correlation function analysis of geomagnetic field reversals. J. Geophys. Res. **84,** B9, pp. 4511–4515

LUTZ T. M. 1985: The geomagnetic reversal record is not periodic. Nature **317,** 6036, pp. 404–407

MCFADDEN P. L. 1984: Statistical tools for the analysis of geomagnetic reversal sequences. J. Geophys. Res. **89,** B5, pp. 3363–3372

MCFADDEN P. L. and MERRILL R. T. 1984: Lower mantle convection and geomagnetism. J. Geophys. Res. **89,** B5, pp. 3354–3362

MESZÉNA GY. and ZIERMANN M. 1981: Probability theory and mathematical statistics (in Hungarian). Közgazdasági és Jogi Könyvkiadó, Budapest, 554 p.

NAIDU P. S. 1971: Statistical structure of geomagnetic field reversals. J. Geophys. Res. **76,** 11, pp. 2649–2662

NAIDU P. S. 1974: Are geomagnetic field reversals independent? J. Geomag. Geoelect. **26,** 1, pp. 101–104

NAIDU P. S. 1975: Second order statistical structure of geomagnetic field reversals. J. Geophys. Res. **80,** 5, pp. 803–806
NAIDU P. S. 1976: Reply. J. Geophys. Res. **81,** 5, p. 1034
NESS G., LEVI S., COUCH R. 1980: Marine magnetic anomaly timescales for the Cenozoic and Late Cretaceous: A précis, critique, and synthesis. Rev. Geophys. Space Phys. **18,** 4, pp. 753–770
PHILLIPS J. D. 1977: Time variation and assymetry in the statistics of geomagnetic reversal sequences. J. Geophys. Res. **82,** 5, pp. 835–843
PHILLIPS J. D. and COX A. 1976: Spectral analysis of geomagnetic reversal time scale. Geophys. J. R. Astr. Soc. **45,** 1, pp. 19–33
PHILLIPS J. D., BLAKELY R. J., COX A. 1975: Independence of geomagnetic polarity intervals. Geophys. J. R. Astr. Soc. **43,** 3, pp. 747–754
ULRYCH T. J. and CLAYTON R. W. 1976: Comment on 'second-order statistical structure of geomagnetic field reversals' by P. S. Naidu. J. Geophys. Res. **81,** 5, p. 1033

## A PALEOMÁGNESES POLARITÁS–IDŐ SKÁLÁK STATISZTIKAI TULAJDONSÁGAI

MITNYIK János

A paleomágneses polaritás–idő skálák statisztikai vizsgálatának célja, hogy információt szerezzünk a térfordulások átlagos időbeli viselkedéséről, és ezek felhasználásával olyan modellt készítsünk a jelenségről, amely ugyanezeket a statisztikai tulajdonságokat tükrözi. E feladatok közül a dolgozat az átlagos időbeli viselkedés leírását tűzte maga elé. A legújabb időskálák vizsgálatával a következő eredmények adódnak:

— a polaritásintervallumok időben nem-stacionárius viselkedést mutatnak, amely lineáris regresszióval közelíthető;
— az észlelt polaritásintervallumok gamma-eloszlást követnek; az eloszlás paraméterei változtak a földtörténeti múltban;
— a jelenlegi matematikai statisztikai módszerekkel nem vizsgálható az intervallumok függetlensége, analitikus úton — megfelelő feltételek esetén — azonban bizonyítható;
— a tér stabilitása mindkét polaritásállapotra azonos; a polaritásállapotok túlsúlyának kérdése összekapcsolódik a gamma-elosztás $\lambda$ paraméterének változását előidéző folyamatokkal

## СТАТИСТИЧЕСКИЕ СВОЙСТВА ПАЛЕОМАГНИТНЫХ ШКАЛ ПОЛЯРНОСТЬ–ВРЕМЯ

Янош МИТНЬИК

Цель статистического исследования палеомагнитных шкал полярность–время заключается в извлечении информации о среднем поведении изменений полярности во времени и в создании с ее помощью модели, отражающей те же статистические свойства. Из этих задач в данной статье рассматривается характеристика среднего поведения во времени. При изучении новейших шкал времени можно придти к следующим выводам:

— интервалы постоянной полярности обнаруживают не стационарное во времени поведение, которое может быть аппроксимировано линейной регрессией;
— наблюдаемые интервалы постоянной полярности распределены по гамма-закону; параметры распределения менялись в ходе геологической истории;
— независимость интервалов не может быть изучена известными математическими методами, но—при надлежащих условиях—может быть доказана;
— стабильность поля одинакова в обоих состояниях полярности; вопрос о преобладании состояния той или иной полярности связана с процессами, вызывающими изменения параметра $\lambda$ гамма-распределения.

GEOPHYSICAL TRANSACTIONS 1988
Vol. 34. No. 4. pp. 309–332

# SYNTHETIC 2-D SEISMIC WAVE PROPAGATION USING A HYPERCUBE PARALLEL COMPUTER

Johnny PETERSEN* and Rosemary RENAUT**

Large 2-D synthetic seismic wave propagation codes using explicit finite difference methods, are computing intensive. These codes need present day supercomputers to produce artificial traces on a timescale of minutes. An alternative is to run similar codes on a parallel computer which is available for a fraction of the cost of a serial computer with similar power. Following this option a finite difference code has been written for a 32 processor Inter Hypercube parallel computer. Each processor can be compared to an IBM PC–AT. The 2-D region was divided into 32 equally large subregions and distributed among the processors. Each processor has its own memory of 512 kbytes, where about 250–300 kbytes are available for programming. The problem is an ordinary 2-D seismic code with absorbing boundaries on the bottom, left and right sides based on the CLAYTON and ENGQUIST [1977] paraxial model. The different aspects of programming on a Hypercube are discussed. An example problem is presented together with the results. The program was also run on 1 and on 16 processors. The CPU times for the different processor configurations are presented and the multiprocessor efficiency is discussed.

**Keywords: synthetic seismograms, wave propagation, computers, hypercube parallel computers, finite difference analysis**

## 1. Background

An important step in understanding seismic measurements as required by the oil industry is the modelling of seismic wave propagation on a computer. The effect certain geologic structures have on a seismic wave can be modelled accurately by the solution of the wave equation. The model gives important insights into the relationships between changes in densities, positions etc. of structures and the echos received, however it is a computationally intensive problem.

A recent development within the computer industry is the advent of highly parallel computers. These machines make large computing power available at lower cost. Problems with a high degree of parallelism, such as this, can make optimum use of this new computer architecture. Here we show that the seismic wave problem can be efficiently solved using the finite difference method on a

* Bergen Scientific Centre IBM, Allegt. 36, Bergen, Norway
Formerly: Chr. Michelsen Institute, Bergen, Norway
** Dept. of Mathematics, Arizona State University, Tempe, Arizona
Manuscript received: 9 May, 1988

Hypercube parallel computer. The problem we have considered incorporates the modelling of an acoustic pressure wave travelling through differing geological strata beneath the ocean floor. The reflections from these strata produce signals received at an horizontal array of hydrophones.

The finite difference equations, Section 2, approximate the two-dimensional partial differential equations of motion describing the propagation of pressure waves in media with varying sound velocities. This numerical method accounts for direct waves, primary reflected waves, multiply reflected waves, diffracted waves and critically refracted waves. This technique can also be applied to include shear waves, and the interaction between shear and pressure waves.

Our algorithm has been implemented on an Intel Hypercube, or iPSC (intel Personal Super Computer). The Intel Hypercube is a parallel computer with 16, 32, 64 or 128 nodes or processors, and a cube manager which is an Intel 310 computer. The configuration at CMI has 32 nodes. The cube manager works as a front end to the parallel machines. Editing of the programs and interfacing to the processors are done through the cube manager. The nodes are in a hypercube architecture of five dimensions, $2^5 = 32$ nodes. A hypercube is a distributed memory machine, this means that each processor has its own memory. CMI has two 32 node hypercubes, one with 512 kbytes of RAM per node, and the other with 4.5 Mbytes of RAM per node. The system takes up about 200 kbytes of RAM per node.

The hypercube architecture is in some sense the optimal solution to having a developed communication between nodes with a minimum number of communication channels. The interconnection scheme is also called a binary $n$-cube, where $n$ is the dimension of the cube with $2^n$ processors. Each processor will have $n$ directly-connected neighbours, so as the number of nodes increases, the number of communication channels per node will increase as $\log(n)$. In order to pass a message from one node to another, the message will in the worst case pass through $n-1$ other nodes. The interconnection schemes for 2, 3 and 4-dimensional cubes are shown in *Fig. 1*. The hypercube topology also maps nicely into other topologies, such as linear arrays, 2-D meshes, 3-D meshes etc. In our case we will use the 2-D array.

For a 5-D hypercube with nodes mapped into a 2-dimensional array, we can split the finite difference mesh into 32 subarrays giving each node a subarray to work on. On the edge of the subarray the node needs to communicate with another node which is a nearest neighbour node (except where the edge is at the boundary of the global array). This lowers the time used in communication, and the program can go nearly 32 times faster than with one node. The size of the problem can also be quite large because of large total cube RAM, those at CMI having 16 Mbytes and 144 Mbytes respectfully. The system will use about 6.5 Mbytes. With such memory, large problems can be kept in memory and time-consuming calls to the secondary storage are avoided.

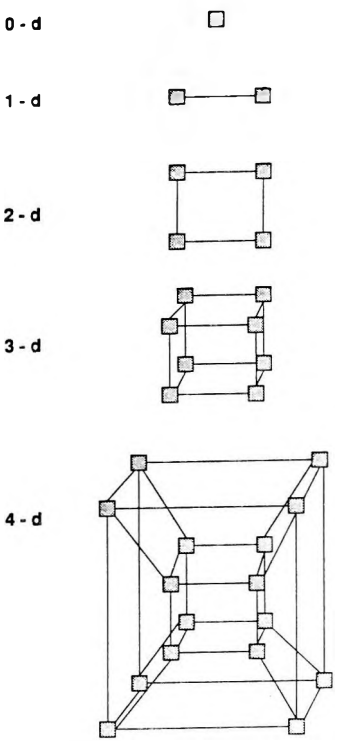


*Fig. 1.* Cubes of different dimensions

*1. ábra.* Különböző dimenziójú hálózatok

*Рис. 1.* Сети с различным количеством измерений

## 2. Description of the work

### *2.1 The wave equation*

The linear wave equation in two dimensions

$$\nabla^2 P = \frac{1}{v^2} \frac{\partial^2 P}{\partial t^2} \tag{2.1.1}$$

is the simplest representation of wave motion in a laterally varying medium. Here $P = P(x, y, t)$ is the pressure wave and $v = v(x, y)$ its velocity, dependent on the density and bulk modulus of the medium. This equation, subject to an initial pulse, representing the explosion, is solved numerically to produce synthetic seismic data.

### 2.2 The interior solution

For the numerical solution of (2.1.1) we have chosen the method of finite differences, as this is a widely used approach for the numerical solution of partial differential equations. In this case it generalizes straightforwardly to application on a local memory parallel processing computer such as the Intel Hypercube, cf. CLAYTON [1986]. The continuous derivatives of the Laplacian in (2.1.1) may be replaced by discrete approximations. For this we introduce the forward and backward difference operators defined by

$$D_q^+ f = \frac{f(q+\Delta q)-f(q)}{\Delta q}$$

$$D_q^- f = \frac{f(q)-f(q-\Delta q)}{\Delta q}.$$

Substituting these operators into (2.1.1) we obtain its discrete form

$$\left[ D_x^+ D_x^- + D_y^+ D_y^- - \frac{1}{v^2} D_t^+ D_t^- \right] P(x, y, t) = 0.$$

Expanding as in the definition gives an explicit recursion relation for $P$ from which the pressure can be advanced in time:

$$\begin{aligned} P(x, y, t+\Delta t) = {} & 2P(x, y, t) - P(x, y, t-\Delta t) \\ & + \left(\frac{v\Delta t}{h}\right)^2 [P(x+\Delta x, y, t) + P(x-\Delta x, y, t) \\ & + P(x, y+\Delta y, t) + P(x, y-\Delta y, t) - 4P(x, y, t)]. \end{aligned} \tag{2.2.1}$$

Here $\Delta x$, $\Delta y$ are the grid sizes in the $x$ and $y$ directions and $\Delta t$ is the time increment. In our case we use a square grid so that $\Delta x = \Delta y = h$. This formula is suitable for all points not lying on the boundary, i.e. *interior points*. In *Figure 2* the difference equation is represented by a stencil. From this stencil it is clear which points at the old time levels the new point depends upon. This is helpful not only for comparing formulae but also in the design of the parallel algorithm.

As we have replaced the continuous derivatives in (2.1.1) by difference expressions the difference formula is not an exact representation of (2.1.1) but only an approximation to it. We say that the numerical formula has *order of accuracy* two as it approximates the real equation accurately up to terms in $h^2$ and $\Delta t^2$. This is seen by applying Taylor's theorem for functions of three variables to the numerical formula. Not only is there an error involved in replacing the continuous derivatives by differences but also, as a consequence, the numerical method will have solutions whose properties differ from those of the real equation. Solutions of (2.1.1) move with a medium dependent *phase* velocity $\vec{c}$, $|\vec{c}| = v$ and energy is transported equally in all directions at a *group*

velocity $\vec{C}$, $|\vec{C}| = v$ normal to the wave front. It is demonstrated in the appendix that this is not the case for the numerical solution, the phase and group velocities being direction dependent and only approximating the true values. Therefore the numerical scheme is *dispersive*. The amount of dispersion may be controlled by picking a grid with sufficiently small gridsize so that the number of points per wavelength is relatively high, i.e. approx. > 10.

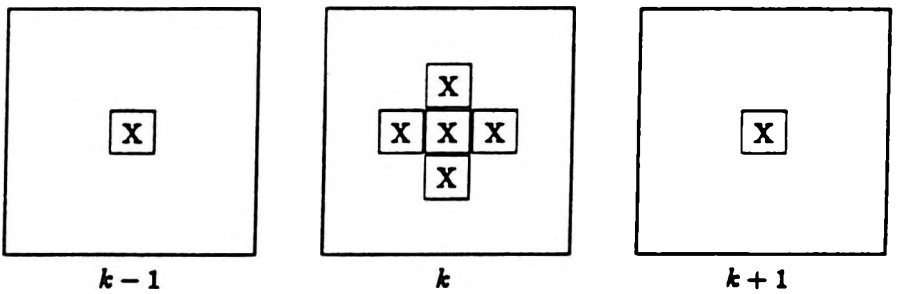


*Fig. 2.* Stencil representing the difference equation

*2. ábra.* A differencia-egyenletet bemutató sablon

*Рис. 2.* Схема представления уравнения разностей

A further criterion which must be considered when using the numerical formula, is the convergence of its solution to the real solution. In this case convergence is equivalent to von Neumann stability, as described in RICHTMYER and MORTON [1967]. The imposition of stability restricts the time increment that may be used according to the inequality

$$\mu = \frac{v\Delta t}{\Delta x} \leqq \frac{1}{\sqrt{2}},$$

where $\mu$ is the Courant number and this condition the Courant condition. The numerical solution at interior points is therefore governed by the properties of the numerical formula which restrict both grid size and time increment. In the Appendix we give two other explicit formulae, one of accuracy two, and one of accuracy four. Dispersion relations and the propagation properties of these schemes are compared to that of the scheme (2.2.1) in PETERSEN and RENAUT [1987].

### 2.3 Boundary conditions

In reality the solution has no strictly defined boundaries. However the numerical solution imposes the need for boundaries to the solution domain. From Fig. 2 we see that the solution of the difference scheme requires knowledge of points outside the domain when we try to solve for points on the boundaries. Therefore an alternative approach is required there. Boundary conditions must be used which mimic the infinite domain of the physical situation.

The situation at the the water surface is the simplest since in reality most energy will be reflected, the velocity of the wave in air being much less than in water. Therefore we impose zero pressure at the surface. At the remaining boundaries, which are artificial, it is required that energy be completely absorbed. We use the absorbing boundary conditions as derived by CLAYTON and ENGQUIST [1977] from paraxial approximations to a one-way dispersion relation. Waves which obey such a relation travel in one direction only, which we choose to be into the boundary. However the one-way wave equations, derived from these approximations, do allow some waves travelling in the wrong direction. By choosing an approximation of sufficiently high order it can be expected that all but glancing reflections will be captured.

The second-order paraxial approximation leads to the one-way wave equation at the right hand boundary:

$$P_{xt} + \frac{1}{v} P_{tt} - \frac{v}{2} P_{yy} = 0. \tag{2.3.1}$$

An approximation of this on the discrete domain is the first-order difference scheme

$$D_x^- D_t^0 P_{Njk} + \frac{1}{2v} D_t^+ D_t^- (P_{Njk} + P_{N-1jk}) -$$

$$- \frac{v}{4} D_y^+ D_y^- (P_{N-1jk+1} + P_{Njk-1}) = 0, \tag{2.3.2}$$

where the central difference operator $D_q^0$ is defined by

$$D_q^0 f = \frac{f(q+\Delta q) - f(q-\Delta q)}{2\Delta q}$$

and $P_{ijk} \approx P(i\Delta x, j\Delta y, k\Delta t)$. The stencil for this formula is given in *Figure 3*. Equivalent formulae are applied for the left and bottom boundaries with the corner points being solved from a rotated formula that ensures absorption for incidence directly into a corner.

For the above boundary conditions the reflection coefficient given in PETERSEN and RENAUT [1987] shows that 99% absorption of waves incident at angles of about 35° to the normal should occur. For angles up to about 75° roughly 35% of energy is reflected with almost complete reflection occurring at glancing incidence [CLAYTON 1986]. In seismic data generation the distance between the initial shot and the final group of hydrophones will be large so that glancing incidence will take place. Obviously we would like as much absorption of these waves as possible. Therefore we chose to use the second order one-way wave equation rather than the first order which predicts absorption of waves only up to incidence about 10°. A higher order approximation is also discussed in PETERSEN and RENAUT [1987].

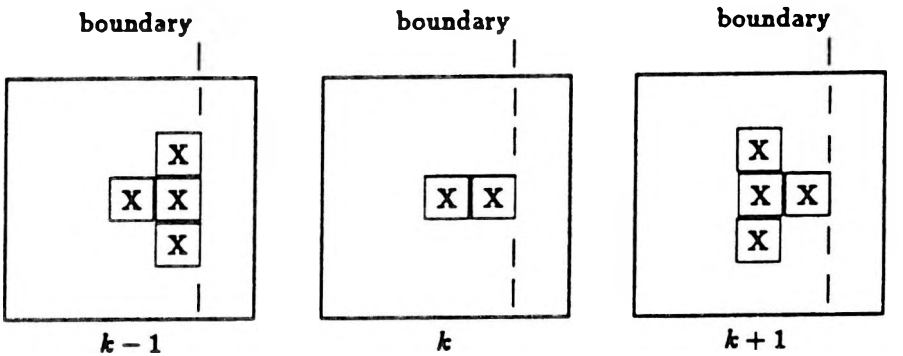


*Fig. 3.* Stencil for the first order difference scheme

*3. ábra.* Az elsőrendű differencia-séma vázlata

*Рис. 3.* Схема разностей первого порядка

### *2.4 Implementation*

For the adaptation of the algorithm for application on a parallel machine, in this case the Intel Hypercube, we have followed the procedure suggested by CLAYTON [1986]. We are required to solve the equation on a rectangular domain. This is easily divided into equal sized rectangular sub regions. In our case we divide into 32 sub regions in order that each processor is in charge of one area of the domain. Information is propagated through the region by assuming an overlap of one row or column between neighbouring processors as in *Figure 4*. At each iteration the values within the processor are updated and the edge values then communicated to the neighbours on all sides. If a processor has an edge which coincides with the boundary of the region it then applies the appropriate boundary conditions.

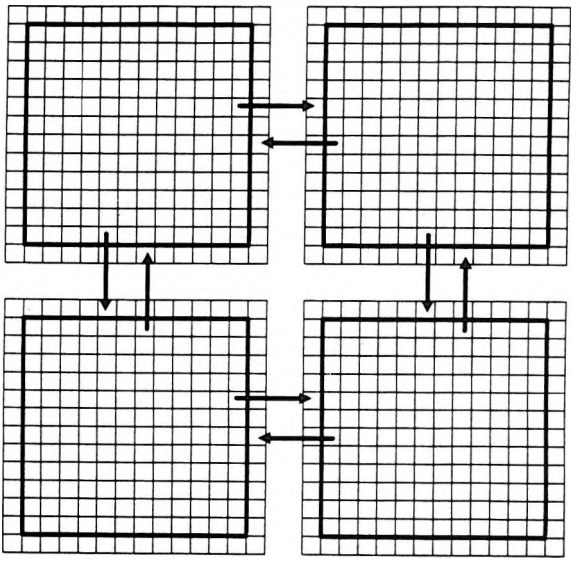

*Fig. 4.* Information propagation between processors

*4. ábra.* Információterjedés a processzorok között

*Рис. 4.* Распространение информации между процессорами

Storage is conserved by overwriting the information at the $k-1$ time level with the updated values of the $k+1$ time level. Therefore we only require a three-dimensional array where the third dimension is two instead of three. However the calculation of the boundary points requires some of the values which have been overwritten. Therefore we need to store additional boundary information in two two-dimensional arrays whose second dimension is only two. This is a considerable saving of storage which becomes more pertinent when we move to the solution of larger problems. We also assume that a processor does not at the same time have boundaries both above and below or left and right. This is a reasonable assumption due to the size of the models that must be considered.

### *2.5 Initial conditions*

For this initial value problem, the initial conditions are the initial pressure amplitude and its first derivative with time, $P(x, y, t = 0)$ and $\mathrm{d}P/\mathrm{d}t$ at $t = 0$. The pressure distribution needs to have a continuous bell shape, making the Lorentzian function, $(\cos f(r) + 1)/2$ and the Gaussian function likely candidates. $f(r)$ is a simple function of $r$, where $r$ is the distance from the initial pressure pulse. The pressure distribution chosen was the Gaussian shape:

$$P(x, y, t = 0) = \exp\left(-\left(\frac{x - x_0}{x_g}\right)^2 - \left(\frac{y - y_0}{y_g}\right)^2\right),$$

where $(x_0, y_0)$ is the location of the source, $x_g$ and $y_g$ are parameters which shape the Gaussian bell. If $x_g \neq y_g$ then the Gaussian will have elliptic contour curves. If $x_g = y_g$ and $x_g$ is small, then the shape will be a pointy peak and the contours will be mostly small circles. The Gaussian pulse, after it has propagated forward in time in 2-dimensions, produces waves which look much like the GSI type A [McQuillin et al. 1984].

### *2.6 Energy norm*

A simple time-independent function of the pressure variable is needed in order to monitor the stability of the time evolution operator. If this function is indeed a constant, then the time evolution is stable. One function which should be constant in time is the total energy of the sound wave, $E_t$ [Landau and Lifshitz 1959]:

$$E_t = \int_V E \, dv$$

with

$$E = \frac{1}{2}\varrho_0 v^2 + \frac{1}{2}\frac{P^2}{c^2 \varrho_0}.$$

$E$ is the energy density of the pressure wave, $\varrho_0$ is the steady-state density of the fluid or material, $c$ is the sound velocity, and $v$ is the velocity of the oscillating particles. In the model discussed here $\varrho_0$ is not given, and $v$ is not calculated.

For monochromatic, parallel waves, the two terms in the energy density equation are equal [Landau and Lifshitz 1959]. Even though the last term will not be the same as the first for our circular, non-monochromatic waves, it will be a slowly varying function in time, approaching a constant value (after the first few timesteps). As long as it approaches a constant finite value, it is possible to use it as an 'energy norm', since it is possible to distinguish its behaviour from the behaviour of an unstable evolution operator. Our 'norm' is thus $p^2/c^2$. Or

$$NORM = \sum_{Nodes} \sum_{i,j} P(i,j) \cdot P(i,j)/V^2(i,j)$$

### *2.7 Brief description of programs and subroutines*

#### *2.7.1 Start up*

The basic layout of programs and the most important subroutines are

shown in *Fig. 5*. The main routine on the host is called TSTCM, which does not need to be on the Intel 310 cube manager, but with the help of the socket program NETCUBE, it may be on any other UNIX workstation available at CMI, such as the Sun-3 or Tektronix. With the NETCUBE program the Intel 310 cube manager is transparent to the other computers. The advantage of NETCUBE is that it unloads the multiuser 310, and thus makes it possible to use advanced features such as graphics on the other workstations while the program is running.

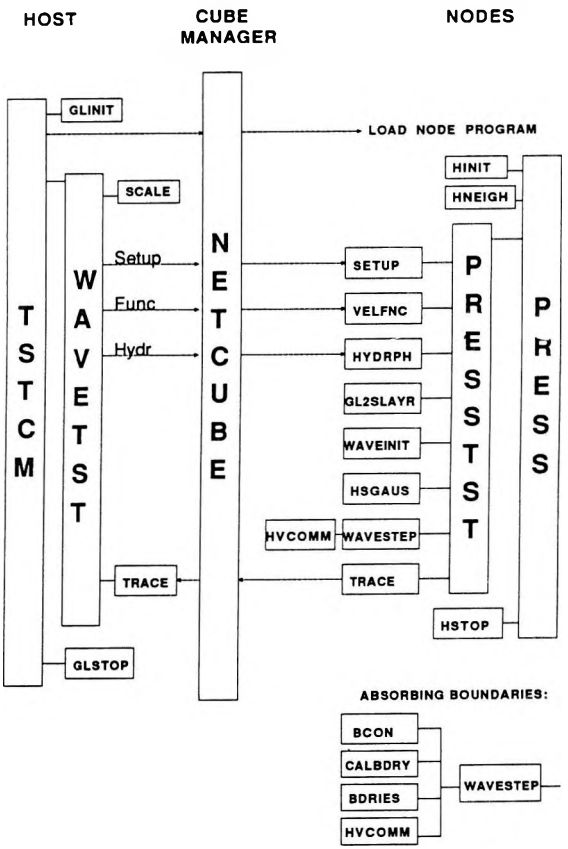


*Fig. 5.* Basic layout of programs and subroutines

*5. ábra.* A programok és szubrutinok elhelyezése

*Рис. 5.* Распределение программи и субрутинов

### 2.7.2 Host program

TSTCM calls GLINIT which initializes parameters needed in communication with the nodes. After GLINIT a message is sent to the Intel 310 to load the correct program, PRESS, onto the nodes. TSTCM then calls WAVETST, which is the main subroutine. WAVETST reads a parameter file, TSTIN which contains the basic parameters for running node programs, such as the grid size, timestep, velocity distribution, etc.

WAVETST then calls SCALE, which scales some of the data from TSTIN to fit with the programs on the Hypercube. The general setup parameters are then sent to the nodes. These parameters are picked up in the subroutine SETUP on all the nodes. This message includes the size of the next message sent to the nodes, *Func*. *Func* is the data containing the velocity distribution and it is received by VELFNC on the nodes. Lastly the initial pulse data, *Hydr*, is sent to the cube and received by the subroutine HYDRPH.

After WAVETST has finished sending data to the cube it goes into a loop and waits to receive the traces from the nodes subroutine TRACE. When all the trace data have been received, the traces are put into a file and WAVETST is finished. TSTCM then calls GLSTOP which closes the opened files, and the program is over.

### 2.7.3 Nodes

The node program is loaded onto the cube when the Intel 310 cube manager gets a message to do so from the host. As soon as it is loaded it starts running. The main program is PRESS, this calls HINIT which initializes the nodes for communication and defines the position of the nodes. HNEIGH is called to set up a special 2-D array for the nodes. In our case the 32 nodes are in a 16 by 2 array since we are looking at a long shallow region. PRESS then calls PRESSTST which is the main subroutine. PRESSTST calls SETUP, VELFNC and HYDRPH in order to receive the necessary data from the host.

SETUP takes in the data defining the problem, VELFNC receives the velocity data, and HYDRPH receives the initial pulse data and the hydrophone data. HYDRPH also checks to see if its node has any hydrophones, and if so it finds the array positions of the hydrophones. It sets a flag if there are any hydrophones. GL2SLAYR sets up the velocity array for each node. WAVEINIT determines whether the node has any boundaries or corners, and initializes the necessary arrays for the absorbing boundaries. WAVEINIT also rescales the velocity array for optimal use in WAVESTEP. PRESSTST then calls HSGAUS which initializes the Gaussian pulse at the prescribed position with the prescribed parameters. The program is now ready to step forward in time. WAVESTEP is the subroutine that does the finite-difference time stepping. Each call to WAVESTEP produces two time step calculation runs.

As discussed above, the $P$-array in each node has 'double' edges, the $P_{N+2jk}$ values on one node is the same as the $P_{2jk}$ values in the array on the neighbour node to the right. (There is an implicit sum over the $j$'s.) Similarly $P_{N+1jk}$ is the same as $P_{1jk}$ on the right neighbour node. During calculations, all but the edge

values are updated. These values must be received from the neighbour node before the next iteration starts. WAVESTEP thus calls HVCOMM which communicates the edge values. HVCOMM sends $P_{N+1\,jk}$ to the right node and $P_{2jk}$ to the left node, and receives the new $P_{N+2\,jk}$ from the right and $P_{1\,jk}$ from the left. It does the same for the up and down directions. After HVCOMM, the array is ready for another time iteration.

If the node is at a boundary, WAVESTEP will call BCON first to store the edge values in order to do absorbing boundaries calculations later. One time iteration is then done for all the inside points. The physical boundary points are done with calls to CALBDRY and BDRIES after which HVCOMM communicates the internal edges between nodes. After the WAVESTEP loop, PRESSTST calls TRACE, which picks out the pressure amplitudes at the hydrophone positions. These values are stored in a trace array which is sent back to subroutine TRACE on the host. This continues until all the traces are finished. PRESSTST returns to PRESS which calls HSTOP, which checks to see if all messages are sent before the program finishes, and if so it closes the communication channel to the host. The program is then finished.

## 3. Results

### *3.1 Test problem*

The test problem considered is that of a 2-dimensional long, shallow region, 350 m deep and 2800 m wide, see *Fig. 6*. The distance to the deepest interface is 300 m, with an absorbing boundary at 350 m and on the left and right vertical sides. The shot has a dominant frequency of 50 Hz, and is set off 5 m below the water surface. The first hydrophone was 125 m behind the shot and 10 m below the water surface, the other hydrophones followed 25 m apart.

The results of the computations are given in Figs. 7–16. Figs. 7–13 are 'snapshots' of the pressure wave in the region (0 m–350 m, 0 m–350 m). *Fig. 7* is the pulse initially (t = 0). *Figs. 8* through 13 show the pulse after propagating 30 msec, 60 msec, 90 msec, 120 msec, 150 msec and finally 180 msec, respectively. One clearly notices the reflections from the different layers, and absorption at the left and bottom boundaries. It is also clear that the water surface, top boundary, reflects with 180° phase shift. The leftmost dot is the starting position of the pulse, and the other dots represent the positions of the hydrophones. The amplitude of the waves are on a variable scale such that the maximum amplitude in each picture has the same displacement. *Fig. 14* shows traces from the 64 'leftmost' hydrophones from 0 sec to 1.024 sec after the initial pulse. *Fig. 15* is an amplified trace plot of all 96 hydrophones from 0 sec to 2.048 sec. In this plot a cutoff amplitude was imposed to make it possible to see the multiple reflected waves. 9 sets of traces were taken at different positions 25 m apart.

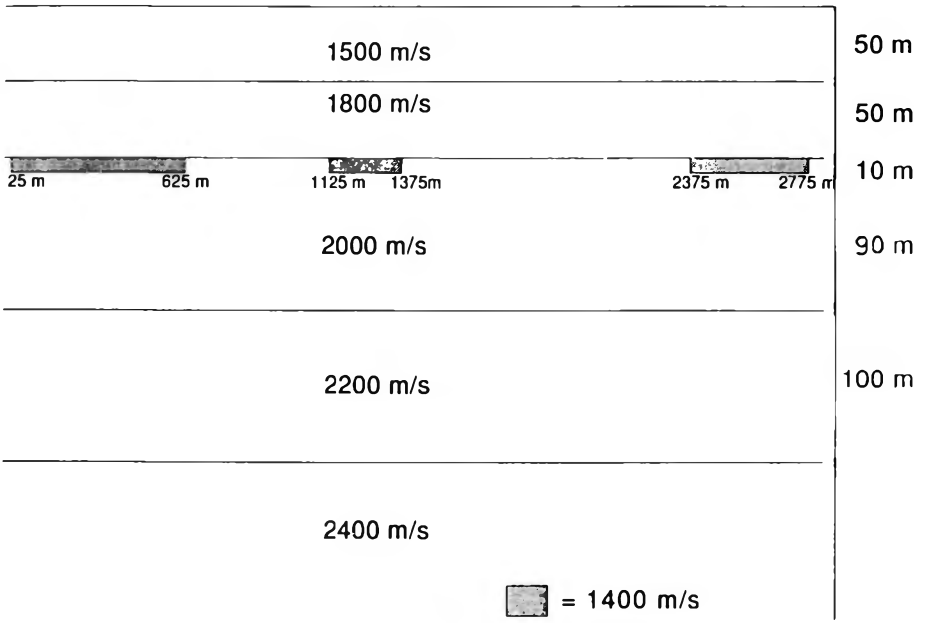


*Fig. 6.* The geological test problem

*6. ábra.* A kísérleti földtani modell

*Рис. 6.* Геологическая модель в эксперименте

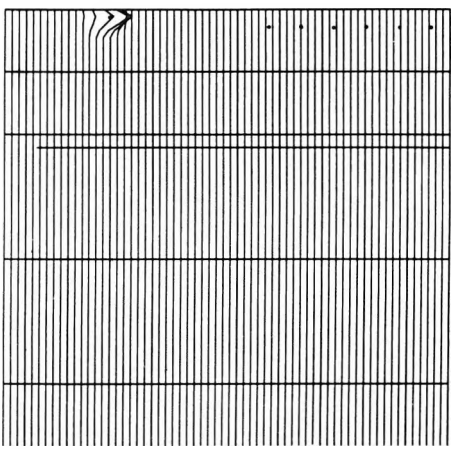

*Fig. 7.* Initial pulse

*7. ábra.* Kezdeti impulzus

*Рис. 7.* Начальный импульс

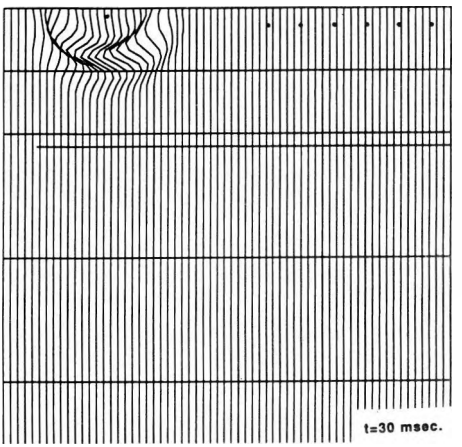
t=30 msec.

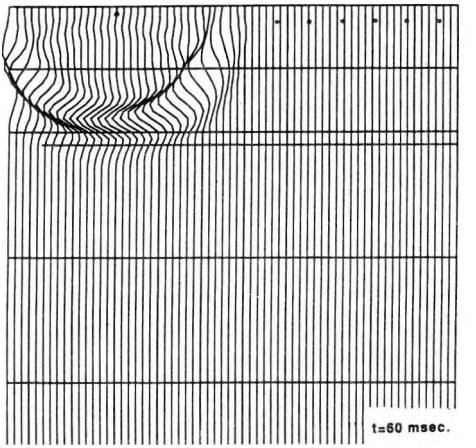
t=60 msec.

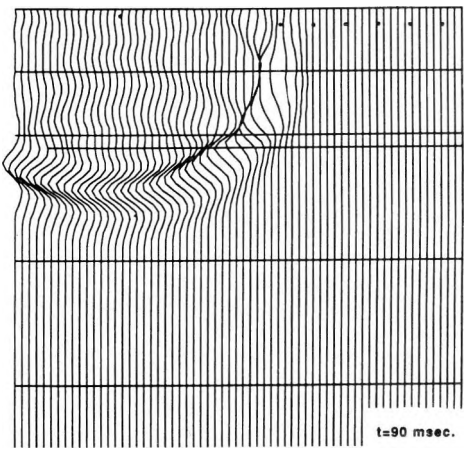
t=90 msec.

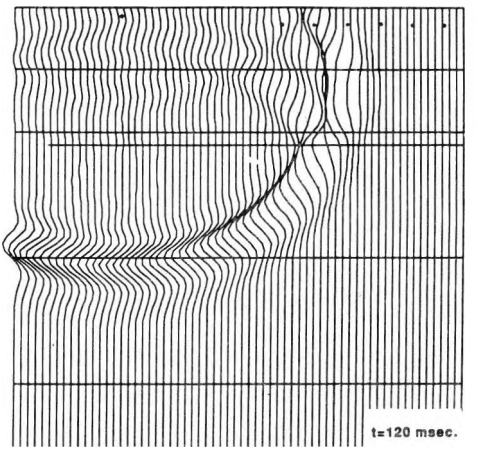
t=120 msec.

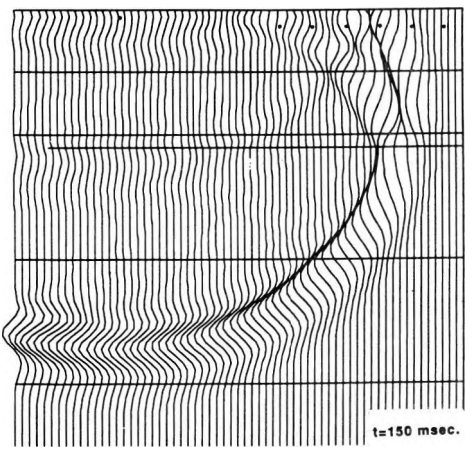
t=150 msec.

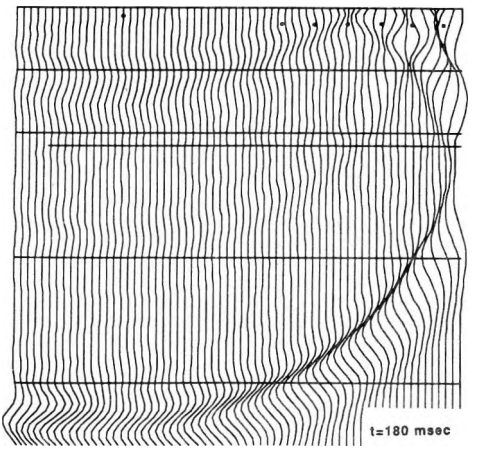
t=180 msec

*Figs. 8–13.* Snapshots of the pressure wave at time $t$

*8–13. ábra.* A nyomáshullám képe $t$ idő elteltével

*Рис. 8–13.* Изображение волны сжатия через время $t$

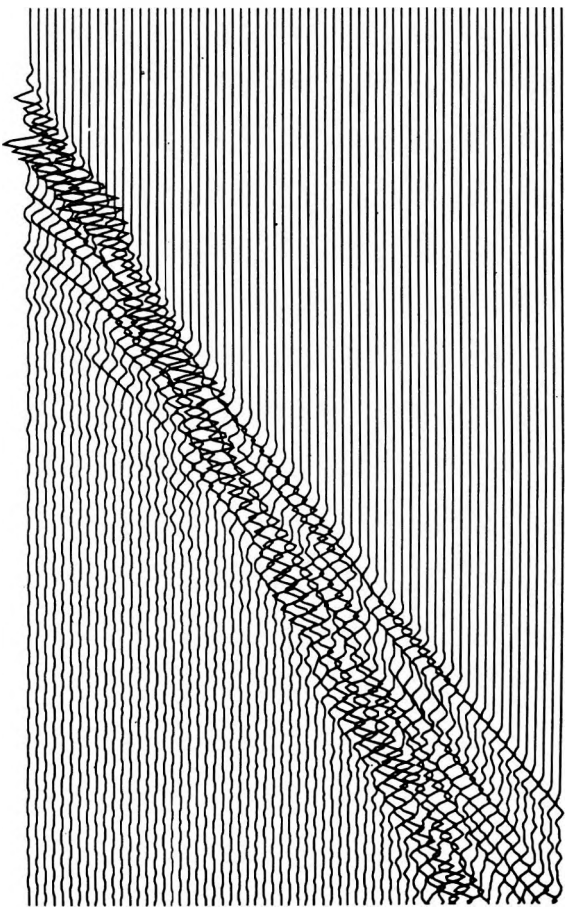

*Fig. 14.* Traces from the 64 leftmost hydrophones from 0 sec to 1.024 sec after the initial pulse

*14. ábra.* A bal oldali 64 hidrofon szeizmogramja 0-tól 1,024 s-ig a jel indítása után

*Рис. 14.* Сейсмограмма по 64 левым гидрофонам от 0 до 1,024 сек после начального импульса

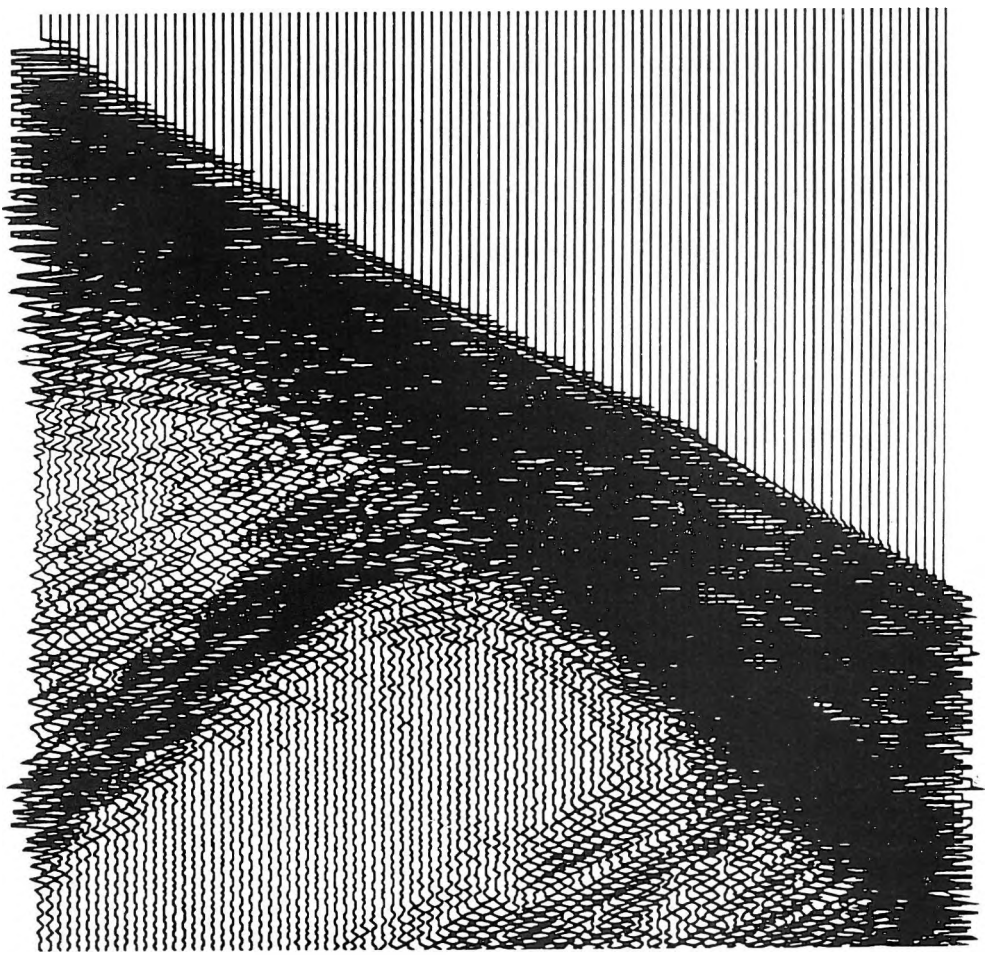

*Fig. 15.* Amplified trace plot of all 96 hydrophones from 0 sec to 2.048 sec. Shot at $x = 80$ m

*15. ábra.* A 96 hidrofon erősített szeizmogramja 0-tól 2,048 s-ig. Robbantás $x = 80$ m-ben

*Рис. 15.* Усиленная сейсмограмма по 96 гидрофонам от 0 до 2,048 сек. Взрыв при $x = 80$ м

Each data set consisted of all 96 hydrophones over 2.048 sec with a sampling every 4 msec, a total of $512 \times 96$ samples per trace file. The first shot, rightmost, was at 255 m from the left boundary, and the last at 55 m. *Fig. 16* contains the tracedata at 255 m. Fig. 15 was taken at 80 m.

A test run was also made to see the extent of the reflection off the 'absorbing' boundaries. This time the whole region was filled with salt water, $V = 1500$ m/s, and it had a reflecting boundary on the top and absorbing

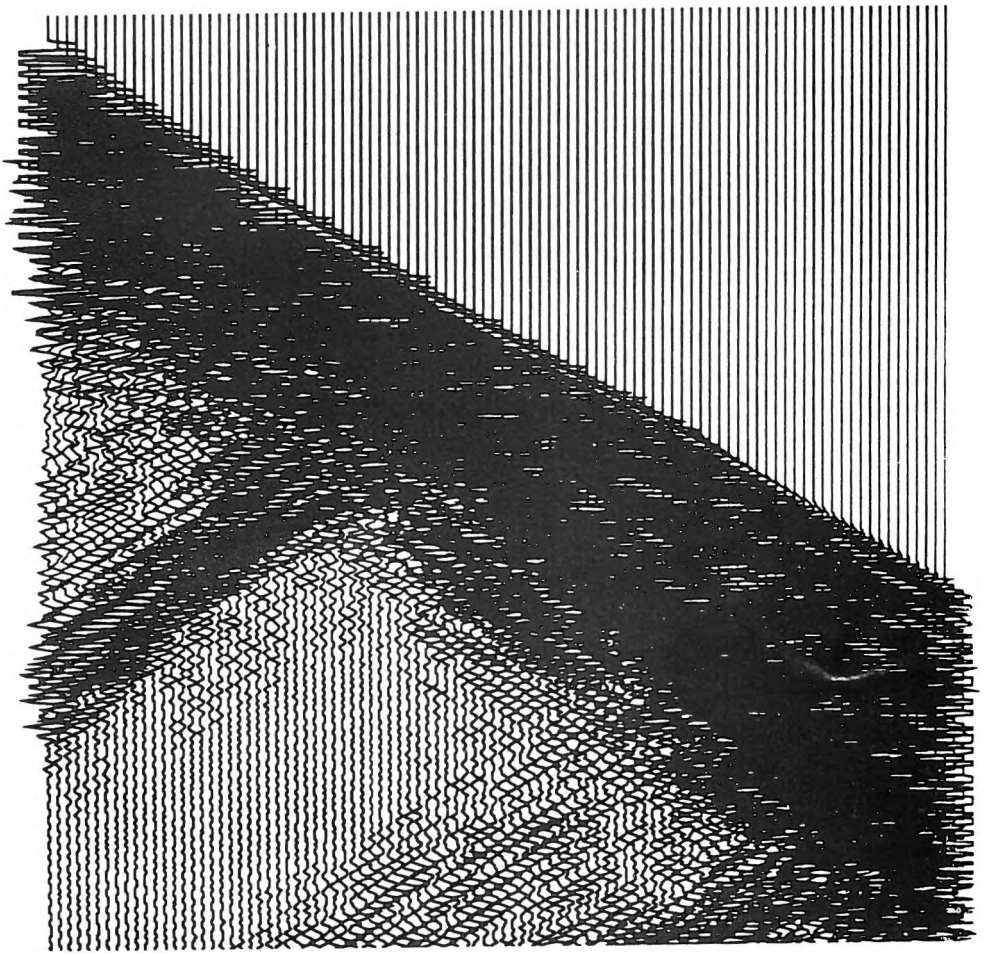

*Fig. 16.* Amplified trace plot of all 96 hydrophones from 0 sec to 2.048 sec. Shot at $x = 255$ m

*16. ábra.* A 96 hidrofon csillapított csatornái 0-tól 2,048 s-ig. Robbantás $x = 255$ m-ben

*Рис. 16.* Сейсмограмма по 96 гидрофонам с затуханием от 0 до 2,048 сек. Взрыв при $x = 255$ м

boundaries on the bottom and vertical sides. Otherwise the 2-D box was of the same size as that above, 2800 m horizontally and 350 m vertically. The position of the shot and the positions of the hydrophones were also similar to those in the above examples. Since the region of interest was so shallow, we should expect to see a large amount of reflection from the bottom boundary. The angle of incidence at the bottom boundary for waves hitting the middle hydrophone is greater than 72° from the normal. For 2*nd* order boundaries, this causes a

reflection coefficient of 35%. For the last hydrophone the angle is 82° and the reflection coefficient is 57%. The test run, *Fig. 17* did not contain any layers, only water with sound velocity of 1500 m/s, and the vacuum–water interface at the top. This interface causes the direct pressure wave amplitude to decrease rapidly with hydrophone position because of destructive interference with the 'mirror' shot above the water surface. The other reflection is the echo from the left 'absorbing' boundary.

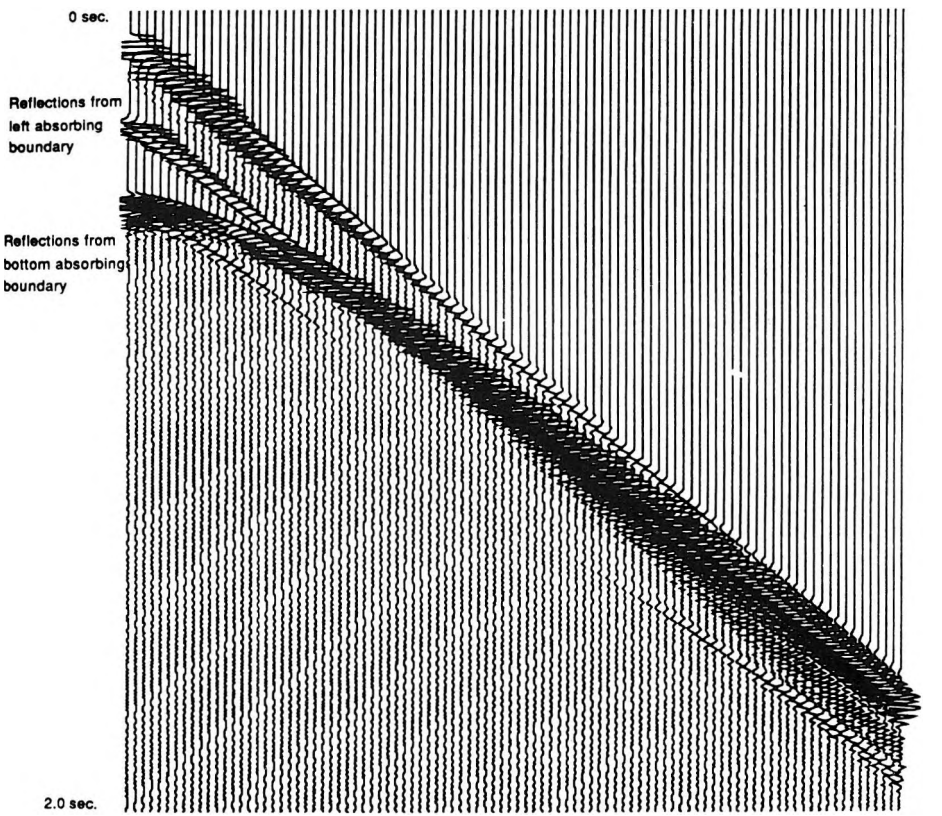


*Fig. 17.* Test run for one-layer case, with 1500 m/s velocity

*17. ábra.* Kísérleti futtatás 1500 m/s sebességü egyréteges modellre

*Рис. 17.* Эксперимент на однослойной модели со скоростью 1500 м/сек

### 3.2 Timing

We have obtained the timings given in *Table I* by setting up the same problem in each case. The problem solved is that already described, 350 m × 2800 m with a grid size of 2.5 m and a time increment of 0.0005 s. This means that each node of the 5-dimensional hypercube uses a pressure array of size 72 × 72 × 2, the 4-dimensional an array 142 × 72 × 2 and the 0-dimensional an array 1120 × 140 × 2, in order to cope with the whole problem. The number of iterations was 4048 for the 5-D cube and 256 otherwise. Therefore timings per iteration are calculated. Clearly it is time consuming to run the complete problem on the zero-dimensional cube. In each case we give the amount of speed-up gained by using the 5-D cube.

Timings for the second-order 9-point stencil (A.2) are also given. We notice that the number of arithmetic operations indicates that the 5-point stencil should be about 1.7 times faster. Here this is confirmed. There is a slight reduction in speed-up as the algorithms are the same away from the interior points. The results which we have plotted show no appreciable differences between the two solutions. However, this is to be expected when solving on such a fine grid. Also any improvement in the results can only be judged by performing the inverse problem on the trace data. Additionally tests need to be run on coarser grids. If, as the theoretical results in PETERSEN and RENAUT [1987] suggest, there is no degradation by using a grid twice as coarse with the 9-point stencil, then it offers a potential speed-up of almost 250%. Not only may the grid be coarsened, also reducing storage requirements, but the stability condition on the Courant number is higher, allowing a larger timestep.

| Scheme | dimension of cube | time per iteration | relative time |
|---|---|---|---|
| $2^{nd}$ order 5pt | 5 | .9995 s | 1.0 |
| $2^{nd}$ order 5pt | 4 | 2.1758 s | 2.1769 |
| $2^{nd}$ order 5pt | 0 | 32.4531 s | 32.4694 |
| $2^{nd}$ order 9pt | 5 | 1.6289 s | 1.6297 |

*Table I.* Timings

*I. táblázat.* Időmérések

*Таб.лица I.* Измерения времени

## 4. Conclusions

The suitability of the Intel Hypercube for the generation of synthetic seismic data has clearly been demonstrated. The solution of the problem here suggests that the Hypercube could be used to solve a large number of hyperbolic problems using the explicit finite difference method.

The parallel computer efficiency, the speed-up achieved with $n$ processors divided by the number of processors, is greater than one, which seems to contradict common sense. However the 80286 chip creates less efficient code if the arrays are larger than 64 Kbytes. This is the case here since the pressure array, the largest array, is 41 Kbytes when the program is distributed and 1.3 Mbytes when the program is running on one node. This is a characteristic of the 80286 chip and the efficiency shown here will not necessarily be reproduced if another processor chip is used. The fact that this is a factor proves that this program is highly parallel, and that the 'load balancing' was very successful. 'Load balancing' means making sure that the problem is divided or balanced equally among the processors, since the parallel program will go only as fast as the slowest processor.

The absorbing boundary algorithm used was not optimal for the long, shallow problem discussed here. The absorbing boundary algorithm seemed to work, as Figs. 7 through 13 show, but no investigation was done to determine if the reflection coefficients were the same as the theory predicted. Energy was absorbed, although not well enough to meet the requirements of good synthetic seismic traces. The Input/Output worked well. The NETCUBE routines made it possible to follow the evolution of the wave on the Sun-3 screen as the program progressed. A small simple input file, TSTIN, made it easy to change the configurations without changing the program, and recompiling.

The succes of this project opens the field for a large number of serious uses of the Hypercube. The program is also written in a highly vectorizable way which will make the program run efficiently on a vector-processor upgrade of the Hypercube. The theoretical analysis of higher order finite difference methods [PETERSEN and RENAUT 1987] shows that speed-up is possible by moving to larger gridsizes and larger timesteps without losing accuracy. Higher order finite differencing and boundary conditions will be investigated in the near future.

## Acknowledgement

This work was supported by a grant from Statoil (Den norske stats oljeselskap a/s).

## APPENDIX

### Stencils, phase velocity and group velocity

#### *A.1 Phase and group velocity derivation*

In section 2 we mentioned that the numerical model has solutions with properties different from those of the real solution. Here we explain this in greater detail.

A general wave solution of (2.1.1) can be represented by the Fourier mode

$$P(\vec{x}, t) = e^{i(\omega t - \vec{\xi} \cdot \vec{x})}$$

where $\omega$ is the temporal frequency and $\vec{\xi} = (\zeta, \eta)^T$ the vector of wave numbers. Substituting this into (2.1.1) we see that the *dispersion relation*

$$\omega^2 = v^2(\zeta^2 + \eta^2) \tag{A.1}$$

is satisfied. Therefore waves propagate in concentric circles with a phase velocity of size $v$ as is seen from the following definition of phase velocity:

$$\vec{c} = \frac{\omega}{|\xi|^2}\begin{pmatrix}\zeta\\ \eta\end{pmatrix} = \frac{v}{\sqrt{\zeta^2+\eta^2}}\begin{pmatrix}\zeta\\ \eta\end{pmatrix}.$$

The energy of the wave is transported at the group velocity:

$$\vec{C} = \vec{\nabla}_{\xi}\omega = \begin{pmatrix}\dfrac{\partial\omega}{\partial\zeta}\\ \dfrac{\partial\omega}{\partial\eta}\end{pmatrix} = \frac{v}{\sqrt{\zeta^2+\eta^2}}\begin{pmatrix}\zeta\\ \eta\end{pmatrix}.$$

Thus energy is also transported equally in all directions with a speed $v$.

We can apply the same analysis to the numerical method to determine the equivalent expressions for the numerical solution. For the formula (2.2.1) the dispersion relation is as given by TREFETHEN [1982]:

$$\sin^2\frac{\omega\triangle t}{2} = \left(\frac{v\triangle t}{h}\right)^2\left[\sin^2\frac{\zeta h}{2} + \sin^2\frac{\eta h}{2}\right].$$

Waves obeying this dispersion relation propagate with a phase velocity of magnitude

$$\frac{\omega}{|\xi|} = v\left(1 + \frac{|\xi|^2h^2}{24}\left(\mu^2 - \left(\frac{\cos 4\theta + 3}{4}\right)\right)\right) + 0((|\xi|h)^4).$$

Here $\mu = \dfrac{v\triangle t}{h}$ is the Courant number and $\theta$ the angle of propagation relative to the $x$ direction. Consequently waves propagate with different speeds in different directions—this is known as *dispersion*. The energy of the numerical solution moves with the group velocity which has components:

$$C_x = v\mu \frac{\sin \zeta h}{\sin \omega \triangle t},$$
$$C_y = v\mu \frac{\sin \eta h}{\sin \omega \triangle t}.$$

Therefore it has a group propagation angle relative to the $x$ axis

$$\Theta = \tan^{-1}\left(\frac{\sin \eta h}{\sin \zeta h}\right).$$

Expanding to lowest order terms

$$|\vec{C}| = v\left[1 - \frac{|\xi|^2 h^2}{8}\left[\frac{3+\cos 4\theta}{4} - \mu^2\right]\right]$$

and

$$\Theta = \theta + \frac{|\xi|^2 h^2}{24} \sin 4\theta.$$

Clearly the group speed also varies in different directions and the variation of the angle of propagation from the correct angle is not constant. Notice also that the expressions for group and phase speeds are accurate in terms of order up to two, this being the same as the order of accuracy of the numerical formula.

### *A.2. The 9-point stencil*

Rotating the 5-point stencil by 45° and combining with the original stencil gives the 9-point scheme second order in space and time:

$$P_{ijk+1} = 2P_{ijk} - P_{ijk-1} + \mu^2(\beta(P_{i+1jk} + P_{i-1jk} + P_{ij+1k} + P_{ij-1k} - 4P_{ijk}) + \frac{1-\beta}{2}(P_{i+1j+1k} + P_{i-1j-1k} + P_{i-1j+1k} + P_{i+1j-1k} - 4P_{ijk})), \qquad (A.2)$$

c.f. TREFETHEN [1982]. The stencil is given in *Figure A.1.*

### *A.3 9-point stencil of 4th order*

ALFORD et al. [1974] have suggested using an alternative stencil which has

fourth order accuracy in space:

$$P_{ijk+1} = (2-5\mu^2)P_{ijk} - P_{ijk-1} + \frac{\mu^2}{12}(16(P_{i+1jk} + P_{ij+1k} + P_{i-1jk} + P_{ij-1k}) - (P_{i+2jk} + P_{ij+2k} + P_{i-2jk} + P_{ij-2k})).$$

The stencil is given in *Figure A.2.*

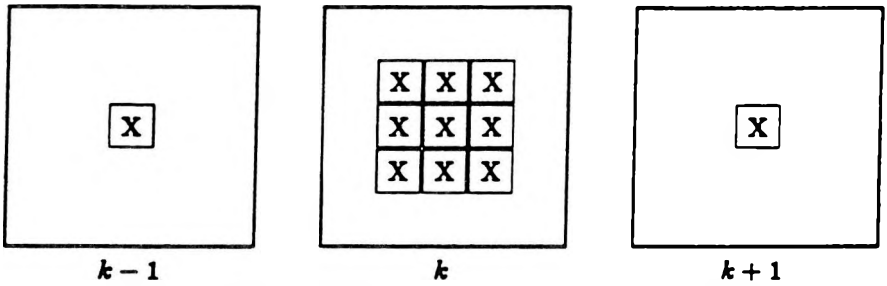


*Fig. A1.* Stencil for a 9-point scheme second order in space and time

*A1. ábra.* Térben és időben másodfokú, 9-pontos séma

*Рис. A1.* Девятиточечная схема, второго порядка в пространстве и во времени

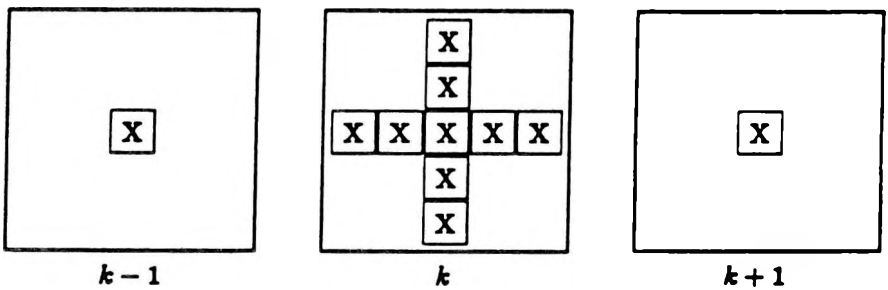


*Fig. A2.* An alternative stencil with fourth order accuracy in space

*A2. ábra.* Egy másik megoldási séma térben negyedfokú pontossággal

*Рис. A2.* Схема другого решения, с точностью четвертого порядка в пространстве

## REFERENCES

ALFORD R. M., KELLY K. R. and BOORE D. M. 1974: Accuracy of finite difference modeling of the acoustic wave equation. Geophysics, **39,** 6, pp. 834–842

CLAYTON R. W. 1986: Finite difference solutions of the wave equation on a concurrent processor. Seismological Laboratory Report, Caltech

CLAYTON R. W. and ENGQUIST B. 1977: Absorbing boundary conditions for acoustic and elastic waves. Bull. Seis. Soc. Am., **67,** 6, pp. 1540–1629

LANDAU L. D. and LIFSHITZ E. M. 1959: Fluid Mechanics. Course of Theoretical Physics, **6,** Pergamon Press

McQuillin R., Bacon M., and Barclay W. 1984: An Introduction to Seismic Interpretation. 2nd ed., Graham and Trotman, London

Petersen J. and Renaut R. 1987: Seismic Wave Propagation using a Hypercube Multiprocessor. CMI report 374502-2, Bergen, Norway

Richtmyer R. and Morton K. 1967: Difference Methods for Initial Value Problems Wiley Interscience

Trefethen L. N. 1982: Group velocity in finite difference schemes, SIAM Review, **24**, 2, pp. 113–136

## SZINTETIKUS KÉTDIMENZIÓS HULLÁMTERJEDÉS MODELLEZÉSE 4-DIMENZIÓS PÁRHUZAMOS SZÁMÍTÓGÉP-HÁLÓZATON

Johnny PETERSEN és Rosemary RENAUT

A kétdimenziós szintetikus szeizmikus hullámterjedést explicit véges differencia módszerrel modellező programok igen számításigényesek. Ahhoz, hogy percek alatt mesterséges szeizmikus csatornákat tudjunk előállítani, a mai szuperszámítógépekre van szükség. Másik lehetőség, hogy hasonló programokat futtatunk párhuzamos számítógépeken, ami a hasonló teljesítményű nagyszámítógép árának csak töredékébe kerül. Ezt az utat választva véges differencia programokat készítettünk egy 32 processzoros Intel Hypercube párhuzamos számítógépre. Mindegyik processzor egy IBM PC/AT-hez hasonlítható. A 2-D területet 32 egyenlő nagyságú alterületre osztottuk, és felosztottuk a processzorok közt. Mindegyik processzor 512 kbyte saját memóriával rendelkezik, melyből kb. 250–300 kbyte használható a programozáshoz. A feladat egy normál 2-D szeizmikus szelvény készítése, abszorbeáló határfelületekkel az alján, jobb és bal oldalon, a Clayton és Engquist [1977] paraxiális modelleknek megfelelően. A 4-dimenziós hálózaton való programozás különböző szempontjait tárgyaljuk. Egy mintafeladatot mutatunk be az eredményekkel együtt. A program 1 és 16 processzoron is futott. A különböző processzor konfigurációkhoz szükséges CPU időket és a multiprocesszor hatékonyságát tárgyaljuk.

## МОДЕЛИРОВАНИЕ РАСПРОСТРАНЕНИЯ СИНТЕТИЧЕСКИХ ДВУМЕРНЫХ ВОЛН НА ЧЕТЫРЕХМЕРНОЙ СЕТИ ПАРАЛЛЕЛЬНЫХ КОМПЪЮТЕРОВ

Джони ПЕТЕРСЕН и Розмари РЕНО

Программы моделирования синтетических двумерных сейсмических волн способом прямых конечных разностей нуждаются в громадном объеме расчетов. Для создания искусственных сейсмических каналов в течение нескольких минут необходимы современные супер-ЭВМ. Другая возможность заключается в загрузке сходных программ в параллельные ЭВМ, что по стоимости составляют лишь ничтожную долю от таковой крупногабаритной ЭВМ. На этом пути нами составлены программы конечных разностей для параллельного компъютера Intel Hipercube на 32 микропроцессорах. Каждый из процессоров сопоставим с IBM PC AT. Двумерное пространство было разделено на 32 равных подпространства и было распределено между процессорами. Каждый из процессоров имел собственную память в 512 килобайт, из которой примерно 250–300 килобайт могут быть использованы при программировании. Задача заключалась в составлении нормального двумерного сейсмического разреза с адсорбирующими поверхностями внизу, а также справа и слева, в соответствии с параксиальными моделями Клейтона и Энгквиста [Clayton and Engquist 1977]. Рассмотрены различные аспекты программирования на четырехмерной сети. Приводится типовая задача вместе с решениями. Программа испытывалась как при 1, так и при 16 процессорах. Рассмотрены времена CPU при различных конфигурациях процессоров, а также эффективность мультипроцессора.

GEOPHYSICAL TRANSACTIONS
Vol. 34. No. 4. pp. 333–342

# SEISMIC DATA ACQUISITION QUALITY CONTROL

Lutz E. REIMERS* and Reiner W. HEIL*

The steadily increasing demands on high-resolution seismology have resulted in new, higher quality technology for field data acquisition. At any particular site, field tests are carried out before starting the routine exploration to determine the optimum parameters of the field technology. During the survey the nearsurface geology may not be constant along the entire profile. That makes it desirable to perform quality control regularly and to change the data acquisition parameters, if necessary, to avoid quality loss. In this paper a set of parameters is introduced for a rapid estimation of data quality in the field, using a statistical interpretation of frequency and energy analysis of every trace. The evaluation of seismic records is thus reduced to a few parameters. These parameters enable the acquisition engineer to compare seismic signals from the different field tests and to define quality standards for the continuous comparison of seismic data along a line and between lines. A field example demonstrates the use of the method to find the best field parameters in practice.

**Keywords: seismic methods, high resolution, data acquisition, quality control**

## 1. Introduction

The development and improvement of seismic methods by more powerful devices for field data acquisition, and bigger and faster computers with better software for data processing, has enabled a larger amount of data to be recorded and processed in ever shorter times. Because of this a time delay between data recording and data processing arises, which does not allow a backward quality-improving influence on the survey as a result of data processing. On the other hand the demands on the results of seismic surveys have steadily increased. For example, at present, structures of some meters in extension are targets only in the geophysical exploration of coal-bearing formations. But in the near future demands will be similar in hydrocarbon prospecting. To meet these demands it is necessary to record data of the best possible quality with the guarantee of permanent fail-proof recording and optimum use of the equipment. On a modern seismic survey, where thousands of geophones are used, neither every geophone nor every element of the recording unit can be checked continuously. It is our aim to create tools to analyse the seismic data, to define by the help of tests an optimum quality and to recognize and to correct losses of quality during the survey.

* Westfälische Berggewerkschaftskasse, Institut für Geophysik, Herner Strasse 45, D-4630 Bochum
Manuscript received: first version:8 September, 1986, revised version: 9 August 1988

The electrical functions of the instruments and the geophones are tested daily. The optimal use of the equipment is guaranteed only, if before the measurements the recording parameters are chosen with regard to the target, and if during the measurements they are adjusted to the sometimes quickly changing seismogeological conditions. This applies particularly to those of the low-velocity layer.

The field parameters are derived from pilot-tests, the so called field-tests. The analysis of these tests is done in most cases in the field-crew HQ, visually counting frequencies, determining wave lengths and velocities and comparing seismograms played back by the data acquisiton system. This method is sufficient in many cases but it is unsatisfactory and out of proportion to the costs of the field tests. Since some thousand traces have to be compared, computer programs have been developed which make it easier to evaluate the pilot-tests in order to optimize the recording parameters. In these programs some statistic indicators (quality-numbers), characterizing the quality of the seismic data, are computed. This means a drastic reduction in data. The evaluation of the field tests provides thresholds for the quality-numbers. To secure constant quality of the running survey a continuous comparison of quality-numbers has to be carried out by an accompanying data processing. The basic requirement for this type of quality control is a short time delay between recording and processing of the data. In our surveys, the data processing was done with the computer of the WBK, Institut für Geophysik in Bochum. The farthest region of exploration was in Emsland, which can be reached by car in three hours from Bochum. The data was transported every day after completing the field-work and processed during the night. In this way a correction of the field parameters was possible with a delay of one day. If one assumes an advance of 60 shots per day with a shot distance of 30 meters then a delay of one day corresponds to 1800 meters in the field. So in the case of minor local geological changes the analysis results can only be used for parallel or cross lines, while quality decrease caused by regional changes in structure can be corrected for in further lines. A mobile computer in the field would have provided the optimum solution.

## 2. Quality analysis of seismic traces

It is certainly impossible to define an absolute measure for the quality of seismic traces, because a seismic survey only gives an image of a geological structure. How much information concerning the subsurface he then extracts therefore depends on the interpreter's intuition and experience. As basic conditions we need wide-band signals, high signal-to-noise ratio for high resolution. We can improve signal-to-noise ratio by the summing of repeated records and damp coherent noise by the CDP technique. So the definition of quality differences of seismic shots requires knowledge about the total energy and frequency content, the frequency and energy behaviour (i.e. changes of energy and

frequency in time), the signal-to-noise ratio, and either the coherency or the crosscorrelation coefficient of the signal.

The investigation can regard both single traces and ensembles of traces. Whatever the investigation, criteria have to be developed which make it easier to show differences between seismic signals, in order to select the best signal among a couple of qualitatively similar signals and to recognize any quality decrease during the survey.

### *Amplitude behaviour of seismic traces*

During the recording of seismic profiles not only the ground motions which are generated by the source are registered, but also the permanent ground noise. On a land survey the seismic amplitudes, i.e. the digitally recorded samples on a tape, represent the particle motion (acceleration or velocity) as a function of time. That part of a trace which originates from the stratified earth, providing information on it, is termed the signal. All other parts of the trace are called noise. With a seismic source a wavefield consisting of different wave types is generated. These wave types are: *P*-waves, *S*-waves, surface waves, head waves, reflected waves and multiples. In reflection seismics all waves, except the primary reflected *P*-waves, are considered to be noise. The recorded amplitudes of the seismic trace are therefore composed of a superposition of useful waves, source-dependent and source-independent noise. In a normal case only the source-independent noise may occur in time before the arrival of the direct wave or the head wave. The direct waves should have the highest amplitudes of the trace, because they have very low transmission losses. After extensive tests, a couple of indicators of the amplitude in the time domain proved to be very efficient. So the following quality numbers were defined as the amplitude rms value i.e. a mean amplitude of the seismic trace, the maximum amplitude and its time, the signal-to-noise ratio (or its reverse), the damping of the maximum amplitude, the times of the preceeding value and that of the decay of the trace amplitudes into the noise.

### *Frequency content of seismic traces*

The usual method for studying the frequency content of a seismic trace is to transform it into the frequency domain by the Fourier–transform. The result is an amplitude- and a phase spectrum. The trace length and the analysis window can be chosen in several ways. Taking the whole trace yields one spectrum per trace. The envelope of the spectrum represents the average form of the seismic pulse over the full trace. The individual peaks and troughs of the spectrum represent, in a complicated manner, the thickness of the layers, including the layers which generate multiples.

Another possibility is to take a shorter analysis window per trace. Then the general shape of the spectrum represents the mean form of the seismic pulse within the time window. The peaks and troughs of the spectrum contain information on the thickness of the layers within the time window.

As a further possibility a short but moving time window can be used. The windows may also overlap. This enables us to analyse the changes of the frequency content in time. The frequency content consists of two components; one which is slowly changing and dependent on absorption and other high-frequency filtering mechanisms, and a spatially changing component, which depends on the changing parameters of the layers.

To receive a quick overview of the frequency content of seismic traces a combination of the possibilities mentioned has been chosen. For every trace a frequency spectrum is computed. The beginning and the length of the analysis window can be selected arbitrarily. The cumulative spectrum sum (i.e. the spectrum is integrated) and the mid-frequency at half of the cumulative spectrum sum (i.e. half of the integrated area) are computed. Above and below the mid-frequency two limiting frequencies at an arbitrary percentage of the cumulative spectrum sum can be determined.

*Multi-trace processes using two-dimensional transformation*

If the reflections of a seismic section are superimposed upon by coherent noise with a different slope, then for the analysis of wave types and for the suppression of noise, an $f$–$k$ transform is useful, thus separating direct waves from reflected waves in the $f$–$k$ domain. The summed amplitude squares of the noise and signal parts can then be computed. The result is the spectral power of noise and signal, respectively. These values, in combination with their ratio, define quality numbers in the $f$–$k$ domain.

In the process of stacking if the image of a CDP has to be improved, the shape of the signal should be the same along the reflection hyperbola. A convenient measure for this is the coherence. As the coherence along a straight line can be estimated better then the one along a hyperbola, the $x^2 - t^2$ transform, which converts hyperbolas to straight lines, is suitable for quality estimates of reflection hyperbolae. If you stack along lines with a different dip (slant stack) and form the envelopes in the $v$–$t$ plane, you have an automatic determination of the stacking velocities. The sharpness of the amplitude peaks in the $v$–$t$ plane is a measure for the coherence of the reflection hyperbola in the $x$–$t$ domain. The integration over time results in a maximum and an average coherence, which are defined as quality numbers.

## 3. Field example

The use of the quality numbers is demonstrated now on a sample shot depth and charge test. The test consisted of 27 shots in total at nine different

shot depths (12, 18, ..., 60 meters) with three different charges (270, 540, 1000 grams) in each case. Each shot was recorded on 120 channels with a sample rate of 2 ms. The geophone group interval was 10 meters. First the quality numbers of each trace were computed, then the quality numbers for all traces of each shot were averaged. The following quality numbers were used versus shot depths: the amplitude rms value, the maximum amplitude, the arrival time of the maximum amplitude, the noise-to-signal ratio, the arrival time of a signal attenuated 20 db and that of the signal decaying into noise level, as well as the mid and limiting frequencies. For values corresponding to different charges, different symbols were used.

The amplitude rms values *(Fig. 1)* and the maximum amplitudes *(Fig. 2)* reach a maximum with increasing shot depth and then decrease. The maximum shifts with decreasing charge to greater shot depths. Conclusion: the optimal shot depth is 24 to 42 meters, with a tendency to decreasing slope with bigger charges. The times of the maximum amplitudes *(Fig. 3)* drop sharply with increasing shot depths and remain at a low level beyond 40 meters. As in the given study area, the target was near the first arrival, a shift of the maximum amplitude to later times means that the seismogram contains high-energy slow waves (noise, surface waves, etc.). Conclusion: a minimum shot depth of 42 meters and no influence of the charge. The minimum of the noise-to-signal ratio

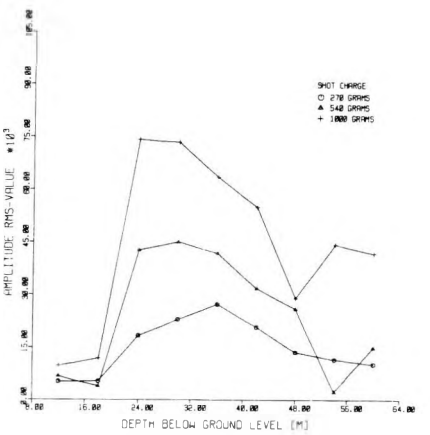


*Fig. 1.* Rms amplitude versus shot depth

*1. ábra.* Robbantási mélység és átlagnégyzetes amplitúdó összefüggése

*Рис. 1.* Взаимосвязь между глубиной взрывания и среднеквадратичными амплитудами

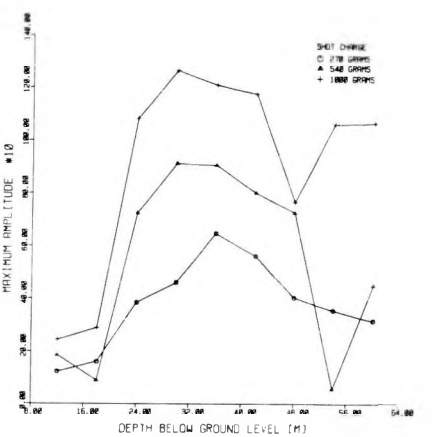


*Fig. 2.* Maximum amplitude versus shot depth

*2. ábra.* Robbantási mélység és maximális amplitúdó összefüggése

*Рис. 2.* Взаимосвязь между глубиной взрывания и максимальными амплитудами

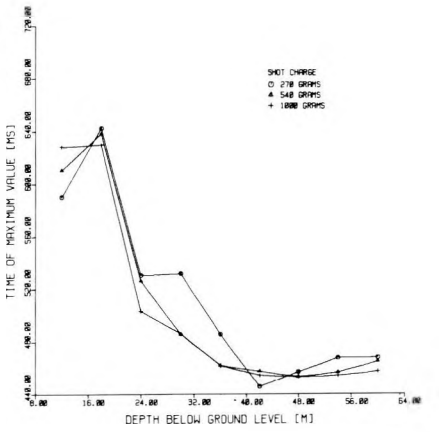


*Fig. 3.* Time of maximum amplitude versus shot depth

*3. ábra.* Robbantási mélység és maximális amplitúdó beérkezési idejének összefüggése

*Рис. 3.* Взаимосвязь между глубиной взрывания и временами вступления максимальных амплитуд

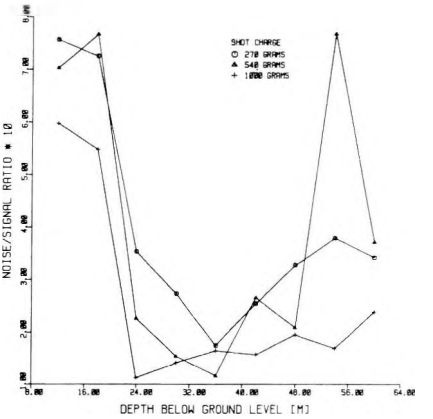


*Fig. 4.* Noise/signal ratio versus shot depth

*4. ábra.* Robbantási mélység és zaj/jel viszony összefüggése

*Рис. 4.* Взаимосвязь между глубиной взрывания и соотношениями шум/сигнал

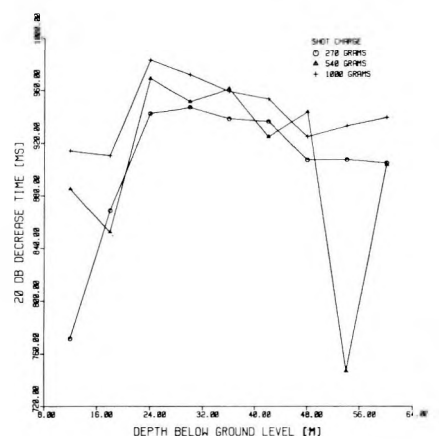


*Fig. 5.* Time of maximum amplitude decrease versus shot depth

*5. ábra.* Robbantási mélység és a maximális amplitúdó 20 dB-es csillapodási idejének összefüggése

*Рис. 5.* Взаимосвязь между глубиной взрывания и временами затухания максимальных амплитуд на 20 дбел

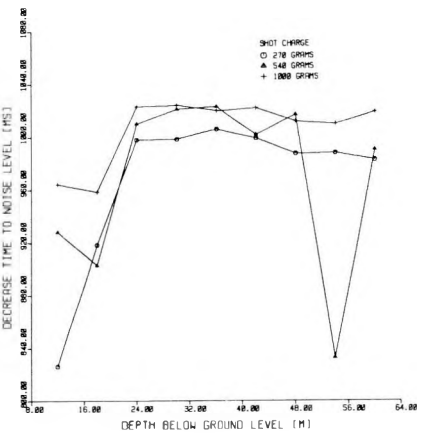


*Fig. 6.* Decay time to noise level versus shot depth

*6. ábra.* Robbantási mélység és a maximális amplitúdó lecsengési ideje közötti összefüggés

*Рис. 6.* Взаимосвязь между глубиной взрывания и временами полного затухания максимальных амплитуд

*(Fig. 4)* coincides with the maximum amplitudes. Conclusion: shot depth 24 to 48 meters, prefer higher charges. The times of the attenuation of the maximum amplitude and that of its decay to noise level (*Figs. 5* and *6*) indicate that the three different charges do not differ very much with regard to penetration. With a shot depth of at least 20 meters they secure a reflection time not under 1 second. Conclusion: shot depth not under 20 meters, the charge does not influence the result.

The mid- and limiting frequencies *(Fig. 7)* rise continously with increasing shot depths, with smaller charges creating higher frequencies. Conclusion: great shot depths, small charges.

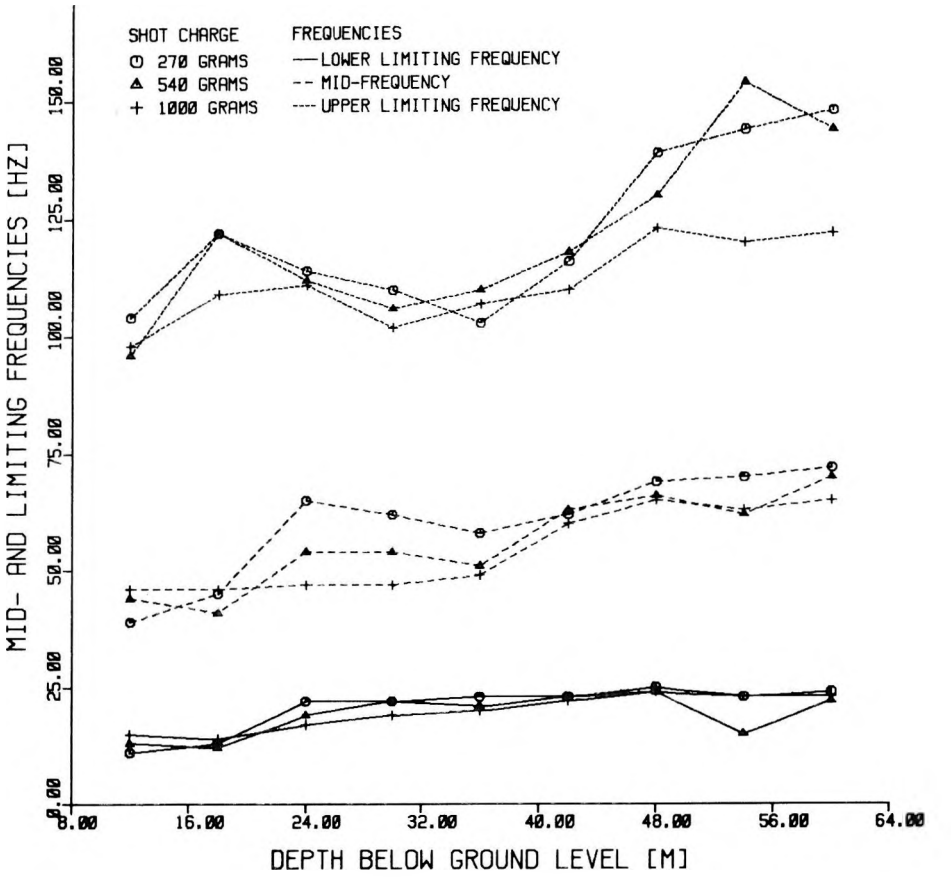


*Fig. 7.* Mid- and limiting frequencies versus shot depth

*7. ábra.* Összefüggés a robbantási mélység és a közép-, illetve határfrekvenciák között

*Рис. 7.* **Взаимосвязь между глубиной взрывания и средними или пограничными частотами**

## 4. Conclusion

Seismic data acquisition quality control is a method to increase the resolution of seismic data. In this, the response of the whole system including the earth filter is analysed. Single parts of the recording equipment and the geophysical parameters are not individually tested. With that method it is also immediately possible to detect failures of different sources on the recorded data and it facilitates quick counter-measures to dispense with disturbances.

Along the profiles begun with the parameters determined by a couple of

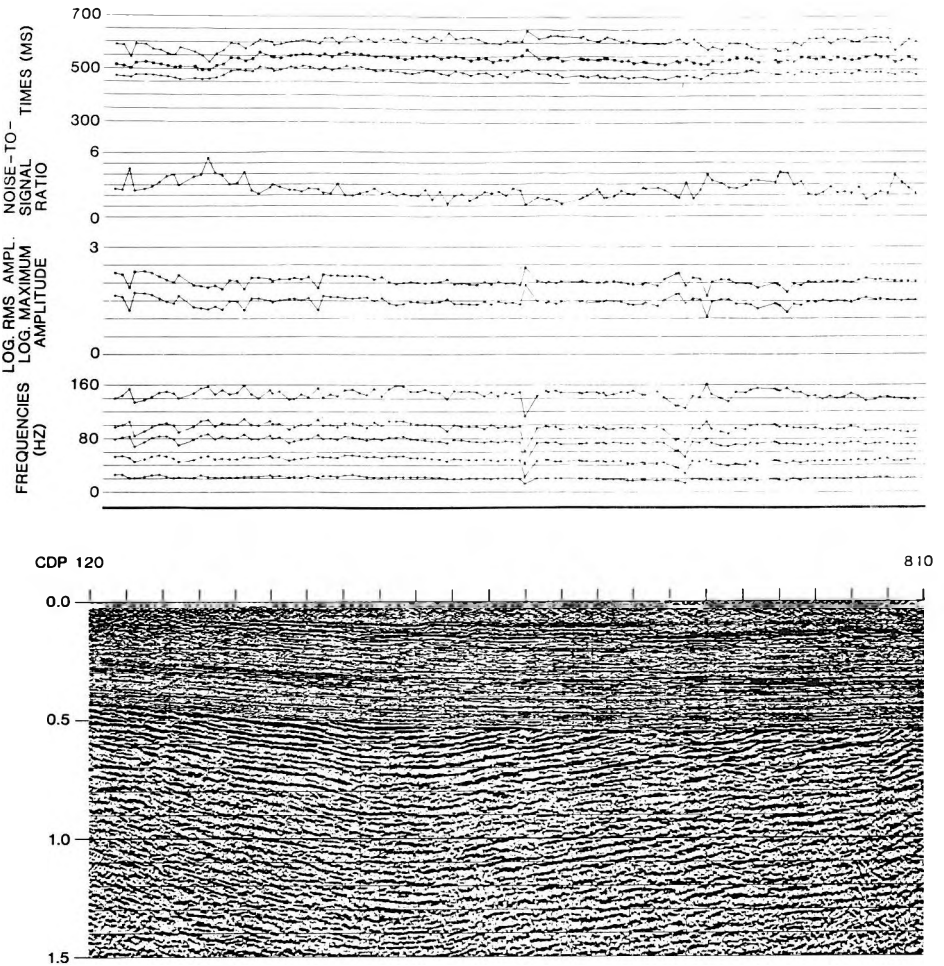


*Fig. 8.* Seismic time section shot with continuous quality control

*8. ábra.* Folytonos minőségellenőrzés mellett felvett szeizmikus időszelvény

*Рис. 8.* Сейсмический временной разрез, записанный при непрерывном контроле за качеством

test shots, it was found by comparing the quality numbers of the original test shots, that overall quality could be maintained *(Fig. 8)*. The developed analysis programs have been tested on some seismic profiles for coal, oil and gas prospecting. According to the statements of the contractors, the results show a reasonable improvement compared with former measurements.

## Acknowledgements

This investigation was financially supported by the Bundesminister für Forschung und Technologie (BMFT) of the Federal Republic of Germany.

## REFERENCES

ANSTEY N. A. 1977: Seismic interpretation – The physical aspects. International Human Resources Development Corp. 1.4, Boston, 625 p.

ANSTEY N. A. 1981: Signal characteristics and instrument specifications. In: EVENDEN R. S., STONE D. R. and ANSTEY N. A. (eds.) Seismic Prospecting Instruments Vol. 1., Geoexploration Monographs, 1, 3, Borntraeger, Stuttgart

ARNETZL H., HEIL R. W., REIMERS L. E. 1982: Versuche mit Sprengschnur für eine hochfrequente 3-D Kohleexploration. Nobel Heft **48,** No. 1, pp. 39–52

ARNETZL H., HEIL R. W. 1980: Tests for a high resolution 3–D seismic coal field exploration using detonating cord. EAEG 42nd Meeting, Istanbul, 1980, Abstract of papers, p. 26

HEIL R. W., REIMERS L. E. 1982: The geophysical exploration of coal in the Federal Republic of Germany. Paper presented at the 27th Geophysical Symposium, Bratislava, CSSR

HELBIG K. 1956: Bemerkungen zum Spektrum seismischer Schüsse unter Tage. Geol. Jahrb. **71,** pp. 671–674

JANKOWSKY W. J. 1974: Propagation and attenuation of seismic energy and their relation to sedimentary structures and lithology. Paper presented at the 44th SEG meeting, Dallas, Texas

REIMERS L. E. 1984: Qualitätssicherung bei reflexionsseismischen Messungen. 4. Mintrop–Seminar, Neheim-Hüsten, Mai 1984

REIMERS L. E., ROKITA D., GOLDFLAM S. 1986: Quality analysis of different marine airgun sources. Paper presented at the 48th EAEG meeting, Ostend, Belgium, 1986

RISCHE H. 1983: Influence of charge depth on the frequency content of seismic waves. Geophysical Transactions **29,** 2, pp. 163–171

RÜTER H., SCHEPERS R. 1977: Is it possible to increase the resolution in seismic exploration for coal by using high frequency signals. Paper presented at 47th SEG meeting, Calgary, Alberta, Canada 1977. Abstract published in Geophys. 1977, **42,** 7, p. 1563

RÜTER H., SCHEPERS R. 1978: Investigations of seismic response of cyclically layered carboniferous rocks by means of synthetic seismograms. Geophys. Prospecting **26,** 1, pp. 29–47

ZIOLKOWSKI A., LERWILL V. E. 1979: A simple approach to high resolution seismic profiling for coal. Geophys. Prospecting **27,** 2, pp. 360–393

## SZEIZMIKUS ADATOK MINŐSÉGELLENŐRZÉSE

Lutz E. REIMERS és Reiner W. HEIL

A nagy felbontású szeizmikával szemben támasztott folytonosan növekvő elvárások jobb minőségű mérési adatok gyűjtését lehetővé tevő új technológiák létrejöttét eredményezték. Mielőtt elkezdenénk a rutinmérést, meg kell határozni az optimális mérési paramétereket. A felszínközeli geológiai viszonyok változhatnak a vonal mentén a mérés során. Ez kívánatossá teszi a folyamatos

minőségellenőrzés bevezetését és a paraméterek esetleges változtatását, hogy a minőségromlást elkerüljük. Jelen cikkben egy sor olyan paramétert vezetünk be, amelyek az egyes csatornák energiájának és frekvenciájának statisztikai analízise révén együttesen alkalmasak a mérési adatok minőségének gyors becslésére. A teljes szeizmogram értékelése helyett így csak néhány paramétert kell figyelnünk. Ezek a paraméterek lehetővé teszik, hogy a különböző terepi próbamérésekkel nyert szeizmikus jeleket összehasonlítsuk és a vonal menti és vonalak közti szeizmikus adatok folyamatos összehasonlítására egy egységes minőségi szintet határozzunk meg. Hogy milyen módon juthatunk a gyakorlatban a legjobb mérési paraméterekhez ezzel a módszerrel, azt egy terepi példán mutatjuk be.

## КОНТРОЛЬ ЗА КАЧЕСТВОМ СЕЙСМИЧЕСКИХ ДАННЫХ

Луц Э. РЕЙМЕРС и Райнер В. ГЕЙЛ

Все увеличивающиеся требования к сейсморазведке высокой разрешающей способности привели к созданию методик, обеспечивающих возможность получения более высококачественных измерительных данных. До начала серийных измерений необходимо определить оптимальные параметры измерений. В процессе измерений приповерхностные геологические условия могут меняться вдоль профиля. Это делает желательными как непрерывный контроль за качеством, так и возможность изменений параметров во избежание ухудшения качества. В настоящей статье рассматривается ряд параметров, совместное использование которых дает возможность быстро оценить качество измерительных данных путем статистического анализа энергий и частот отдельно взятых каналов. При этом вместо интерпретации полных сейсмограмм необходимо следить лишь за несколькими параметрами. Этими параметрами обеспечивается сопоставимость сейсмических сигналов, полученных при различных опытных полевых измерениях, а также определение единого качественного уровня при непрерывном сопоставлении сейсмических данных, полученных вдоль профилей и между ними. Способ практического определения наилучших измерительных параметров при данной методике иллюстрируется полевым примером.

GEOPHYSICAL TRANSACTIONS 1988
Vol. 34. No. 4. pp. 343–359

# IN-MINE FREQUENCY SOUNDING WITH A BURIED GROUNDED DIPOLE SOURCE

Ernő TAKÁCS*

The in-seam vertical electric field of an elementary alternating current dipole located in a coal seam—equatorial array—and its frequency dependence are functions of the resistivity and thickness of the layers in the layered space. This study analyses the effect of these parameters on sections which can be regarded as basic models for the investigation of the overlying and underlying layers, and lateral inhomogeneities within the seam.

Using the frequency dependence belonging to the uniform space apparent resistivities ($\varrho_a^*(f)$) can be derived from the changes of the field according to frequency. These, in the form of frequency sounding curves, show the effects of layering more clearly than the frequency dependence of the field strength itself. With the combined application of the apparent resistivities calculated using the geometric factor $\{\varrho_a(f)$ and $\varrho_a^*(f)\}$ the resistivity of the seam can be obtained and the frequency dependence of that part of the space which influences the measurements can be examined. With increasing frequency the effect of the seam increases, especially at smaller transmitter–receiver separations; this is advantageous from the viewpoint of seam exploration.

From the in-seam field of the elementary dipole the potential difference measured using current and potential dipoles of finite size which extend to the host rock can be derived considering the dimensions and resistivity conditions.

**Keywords: grounded dipole source, frequency sounding, layered medium, in-seam geoelectric methods, in-mine geophysics, models**

## 1. Introduction

Several papers describe successful in-mine applications of direct current measurements [CSÓKÁS et al. 1986, BREITZKE et al. 1987]. The potentials of frequency sounding, however, are less well explored. Although the controlling of the investigated rock volume by changing the frequency and the simultaneous application of several parameters, e.g. amplitude and phase, as well as the probable increase in resolution, may have advantages just because of the limitations caused by in-mine conditions.

The inductive generation of the field and the measurement of magnetic field strength are strongly influenced by metal objects in the gallery. Therefore, as a first step, the possibilities of a system applying conductive excitation and measurement of the electric field were examined. The effect of metal objects on this measuring system is expected—and experienced, too—to be much less if groundings are kept at a sufficient distance from these objects. Another aspect

* Department of Geophysics, Technical University for Heavy Industry, Miskolc, Egyetemváros H–3515, Hungary
Manuscript received (revised version): 13 April, 1988

was to rely on known results of direct current measurements. This is how we chose the vertical current dipole and the measurement of the frequency dependence of its vertical electrical field, at the level of the transmitter (equatorial array).

The frequency sounding curves of some models and the algorithm used for calculating them have already been presented [TAKÁCS et al. 1986]. The aim of this paper is to clarify the relationship between the behaviour of the electromagnetic field and the parameters of the layered space, as well as to illustrate more expressively the information on layering and geological structure which is difficult to read out from frequency sounding curves.

## 2. Frequency sounding curve in a uniform space

It is expedient to begin the study of the frequency dependence of the electromagnetic field with uniform space. If this is used for correction, geological information on layering can be represented more clearly.

For the dipole equatorial array, which can be realized in a mine or in boreholes, the frequency sounding curve with a resistivity of $\varrho$ developing in uniform space is shown in *Fig. 1*. The quantity $|E_z(f)|/E_z(0)$ was applied to the ordinate; this quantity is the ratio of the field measured at frequency $f$, $|E_z(f)|$, and the field measured with direct current, $E_z(0)$, at identical electrode array. Because of generalization $R/\delta$ appears on the abscissa, where $R$ is the transmitter–receiver separation, and $\delta$ is the skin depth in a halfspace of resistivity $\varrho$ at frequency $f$. Figure 1 shows that at sufficiently low frequencies the direct current and alternating current fields are equal, or the difference is negligible. With increasing frequency, however, up to the value of $R/\delta = 1.6$, the alternating current amplitude increases to 1.455-times higher than the direct current value. At even higher frequencies—beyond the maximum—the electromagnetic energy (alternating current field) is gradually absorbed, as reflected by the decreasing values of the curve.

The above shows that the apparent resistivity ($\varrho_a$) calculated from $|E_z(f)|$ in the way used in direct current measurements is frequency-dependent even in uniform space, except for the quasi-stationary state part. Even so, it is advisable to plot the results as $\varrho_a(f)$ curves—or at least to calculate $\varrho_a(0)$—since these values carry information on the layers as it will be shown.

## 3. Frequency sounding curves in layered space

So far as layered space is concerned, it is obvious that the quasi-stationary state part provides information equal to that of the direct current measurement for the rock volume in which the current field is strong enough to influence the measured field strength. If this volume includes several layers, each of them will exert its effect on $|E_z|$.

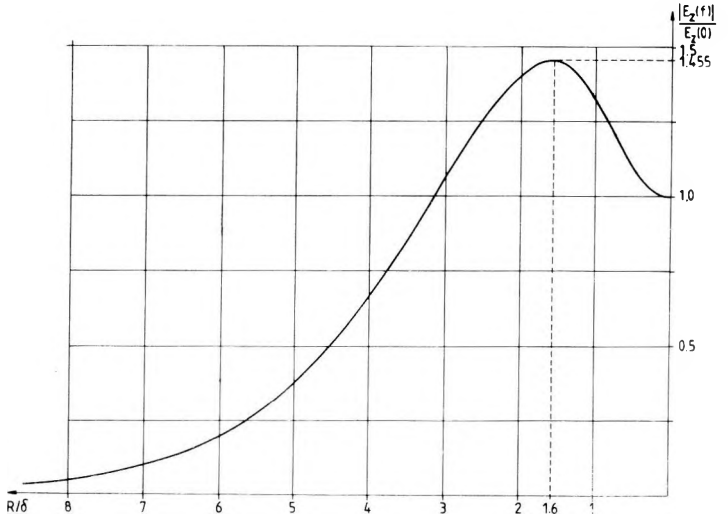


*Fig. 1.* Ratio of the vertical electric field strengths generated by vertical alternating current and direct current elementary electric dipoles versus the $R$ (distance)/$\delta$ (skin depth) ratio

*1. ábra.* A váltóáramú és egyenáramú vertikális, elemi, elektromos dipólus vertikális elektromos térerősségének hányadosa az $R$ (távolság)/$\delta$ (szkinmélység) viszony függvényében

*Рис. 1.* Отношение вертикальной электрической напряженности одиночного вертикального электрического диполя переменного и постоянного токов как функция $R$ (расстояние)/$\delta$ (мощность скин слоя)

With increasing frequency the volume of the current field becomes rearranged. In addition to this, real and imaginary current system develop. Thus, the contribution of the individual layers to the measured field component changes and the effect of layering appears in the frequency sounding curves.

For the time being, analyses of these effects have been performed concerning the absolute values, $|E_z|$, only. In *Figs. 2–4* frequency sounding curves calculated from the absolute values of $E_z$ are shown for various, 3-layer symmetric models, which approximately represent the domestic coal formations. From these curves layer parameters, effects of layering and transmitter–receiver separation can be assessed. This type of models can be considered the basic model for the prospecting task that involves examining the continuity and quality of the coal seam.

It can be stated that the $\varrho_a(f)$ curves of the layered space also show the basic characteristics of Fig. 1, different parts of the curve, however, exhibit deviations caused by the layered space. The characteristic features of these deviations can be summarized as follows.

It is obvious that $|E_z|$ increases if the resistivity of the layer, or layers, lying between the potential electrodes is higher; and it decreases if this resistivity is lower. The reverse is true concerning the resistivity of the layers outside the potential electrodes. The situation is the same for direct current. This is why high

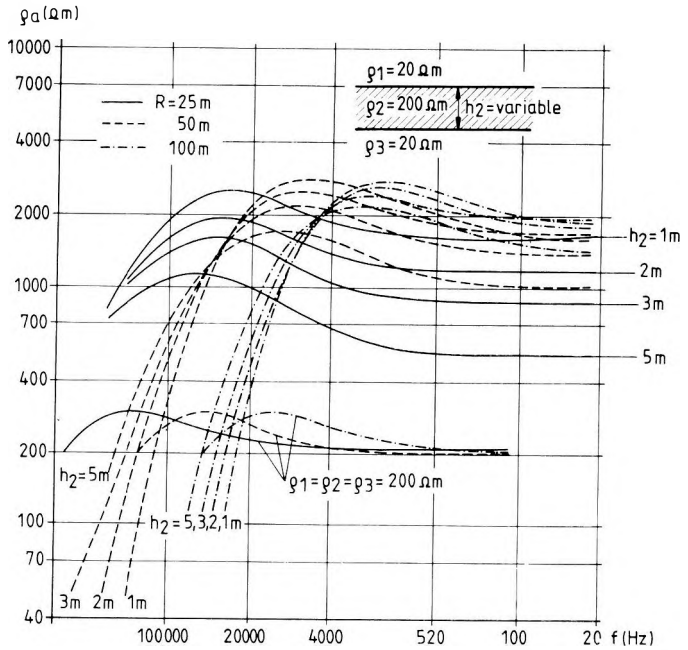


*Fig. 2.* Frequency sounding curves $\varrho_a(f)$ in a 200 Ωm seam with transmitter–receiver separations ($R$) of 25 m, 50 m and 100 m, for the model $\varrho_1 = 20$ Ωm, $h_1 = \infty$, $\varrho_2 = 200$ Ωm, $h_2$ = variable, $\varrho_3 = 20$ Ωm, $h_3 = \infty$

*2. ábra.* A 200 Ωm-es telepben 25 m, 50 m és 100 m adó–vevő távolságon ($R$) kialakuló $\varrho_a(f)$ frekvenciaszondázási görbék a $\varrho_1 = 20$ Ωm, $h_1 = \infty$; $\varrho_2 = 200$ Ωm, $h_2$ = változó; $\varrho_3 = 20$ Ωm, $h_3 = \infty$ modellre

*Рис. 2.* Кривые частотного зондирования $\varrho_a(f)$ при расстояних между передатчиком и приемником ($R$) в 25, 50 и 100 м в пласте сопротивлением 200 омм при модели $\varrho_1 = 20$ омм, $h_1 = \infty$; $\varrho_2 = 200$ омм, $h_2$ = переменная; $\varrho_3 = 20$ омм, $h_3 = \infty$

field strengths can be measured in a coal seam with a resistivity much higher than that of its environment. Thus, apparent resistivities may be significantly higher than the true resistivity of the seam. At the same time, the vertical field component is considerably smaller if a low resistivity layer is embedded in a high resistivity medium; this results in an apparent resistivity much lower than the real one. The magnitude of these effects is obviously a function of the separation $R$, too. With increasing frequency, the current field occupies a smaller volume; this increases the influence of that part of the space, which lies between the potential electrodes, i.e. the seam. This effect depends on the separation $R$, too. As a consequence, for a high resistivity seam—and especially for curves with small $R$ values—the maximum at frequencies beyond the quasi-stationary state section becomes more definite and the value of $\varrho_a(f)_{max}/\varrho_a(0)$ may exceed the highest value of 1.455 obtained for the uniform space. This is the case, for example, for the curve with the parameters $R = 25$ m and $h_2 = 5$ m in Fig. 2. At

the same time, the left, descending part of the curve is less steep. If the layer between the potential electrodes has a resistivity lower than that of the medium, then a phenomenon opposite to the previously outlined one will take place. Approaching the transmitter dipole, the current lines crossing the receiver dipole have a shorter path in the host rock; as a consequence of this and because of the high resistivity seam the effective resistivity of that part of the space which affects the measured value will increase. This results in the shifting of the maximum of the frequency sounding curve towards frequences higher than the frequency determined by the resistivity of the uniform host rock and the separation $R$. On the basis of all these, it can also be understood that the increase of the thickness of a seam with a resistivity higher than that of its environment exerts a similar effect.

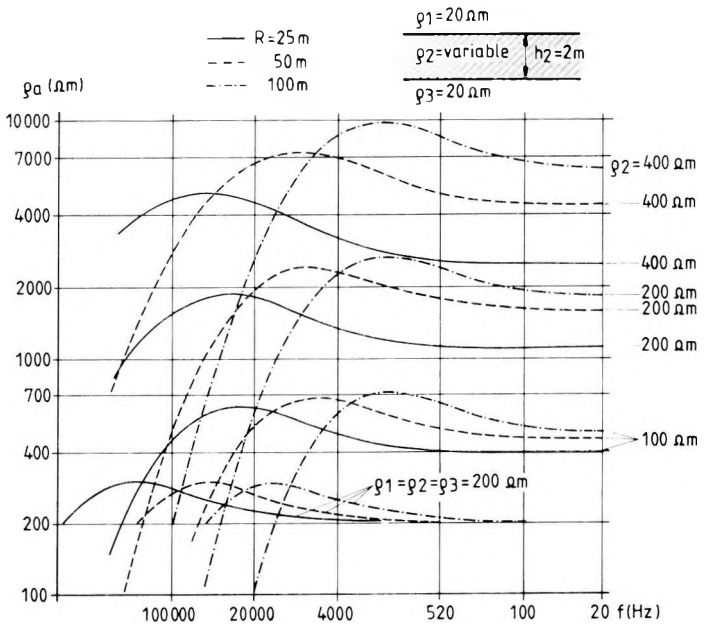


*Fig. 3.* Frequency sounding curves $\varrho_a(f)$ in a seam of resistivity $\varrho_2$, with transmitter–receiver separations ($R$) of 25 m, 50 m and 100 m, for the model $\varrho_1 = 20\ \Omega m$, $h_1 = \infty$, $\varrho_2$ = variable, $h_2 = 2$ m, $\varrho_3 = 20\ \Omega m$, $h_3 = \infty$

*3. ábra.* A $\varrho_2$ ellenállású telepben 25, 50 és 100 m adó–vevő távolságon ($R$) kialakuló $\varrho_a(f)$ frekvenciaszondázási görbék a $\varrho_1 = 20\ \Omega m$, $h_1 = \infty$; $\varrho_2$ = változó, $h_2 = 2$ m; $\varrho_3 = 20\ \Omega m$, $h_3 = \infty$ modellre

*Рис. 3.* Кривые частотного зондирования $\varrho_a(f)$ при расстояних между передатчиком и приемником ($R$) в 25, 50 и 100 м в пласте сопротивлением $\varrho$ омм при модели $\varrho_1 = 20$ омм, $h_1 = \infty$; $\varrho_2$ = переменная, $h_2 = 2$ м; $\varrho_3 = 20$ омм, $h_3 = \infty$

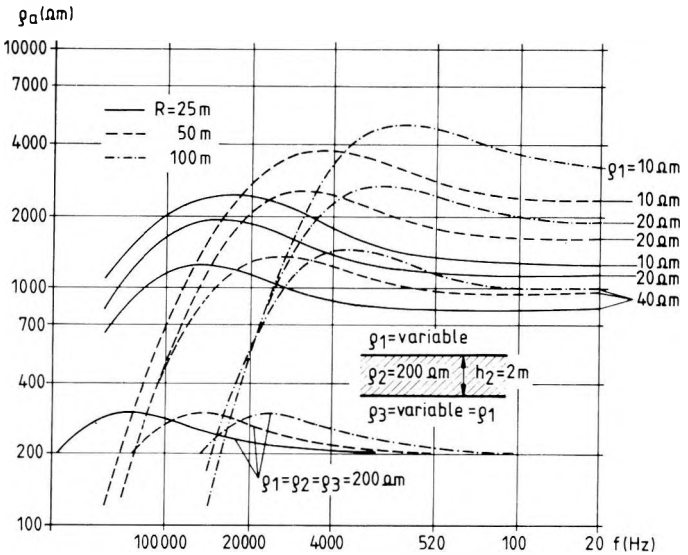


*Fig. 4.* Frequency sounding curves $\varrho_a(f)$ in a 200 Ωm seam with transmitter–receiver separations ($R$) of 25 m, 50 m and 100 m, for the model $\varrho_1$ = variable, $h_1 = \infty$, $\varrho_2 = 200$ Ωm, $h_2 = 2$ m, $\varrho_3 = \varrho_1$ = variable, $h_3 = \infty$

*4. ábra.* A 200 Ωm-es telepben 25, 50 és 100 m adó–vevő távolságon ($R$) kialakuló $\varrho_a(f)$ frekvenciaszondázási görbék a $\varrho_1$ = változó, $h_1 = \infty$; $\varrho_2 = 200$ Ωm, $h_2 = 2$ m; $\varrho_3 = \varrho_1$ = változó, $h_3 = \infty$ modellre

*Рис. 4.* Кривые частотного зондирования $\varrho_a(f)$ при расстояних между передатчиком и приемником ($R$) в 25, 50 и 100 м в пласте сопротивлением 200 омм при модели $\varrho_1$ = переменная, $h_1 = \infty$; $\varrho_2 = 200$ омм, $h_2 = 2$ м; $\varrho_3 = \varrho_1$ = переменная, $h_3 = \infty$

The four-layer model of *Fig. 5* corresponds to the case when the basement is near the seam. It can be seen that the high resistivity bedrock near the seam significantly modifies both the shape and the values of the $\varrho_a(f)$ curve. The figure is also an example of asymmetric layering. Obviously, the frequency at which the curve begins to decrease is mainly determined by the 10 Ωm overlying layer and the 2 m thick and 200 Ωm seam; and the bedrock has hardly any role in it. The maximum of $\varrho_a(f)$ curves appears only if the thickness of the underlying layer exceeds 8 m.

The curves of the five-layer section shown in *Fig. 6* also demonstrate that layers of higher resistivity near the coal seam reduce the maximum of the frequency sounding curve and the vertical field component, too. Because the model is symmetrical the frequency belonging to the maximum noticeably changes. With increasing $h_2$ and $h_4$ the curves approximate more and more the three-layer model curve, since at sufficiently high values of $h_2$ and $h_4$ the current cannot reach the 200 Ωm layers over and under the seam. The model presented indicates the possibility of examining the over- and underlying layers.

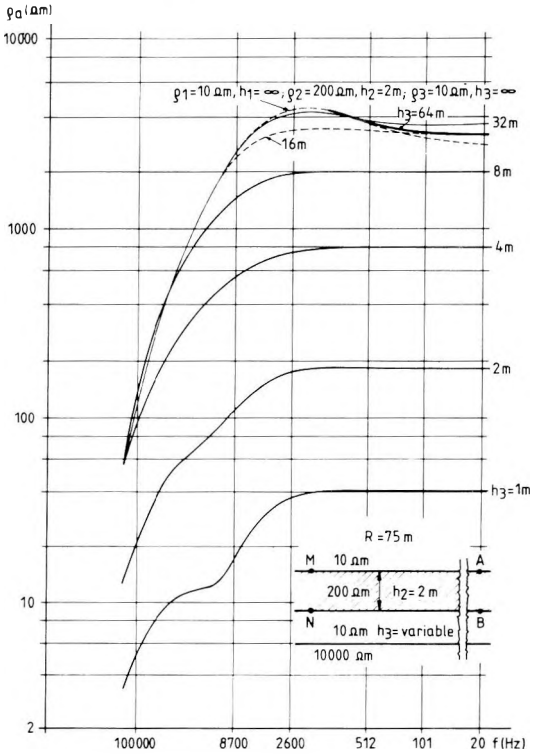


*Fig. 5.* Frequency sounding curves $\varrho_a(f)$ measured in a 200 Ωm seam with 75 m transmitter–receiver separation ($R$) for the model $\varrho_1 = 10$ Ωm, $h_1 = \infty$, $\varrho_2 = 200$ Ωm, $h_2 = 2$ m, $\varrho_3 = 10$ Ωm, $h_3 =$ variable, $\varrho_4 = 10{,}000$ Ωm, $h_4 = \infty$

*5. ábra.* A 200 Ωm-es telepben 75 m adó–vevő távolságon ($R$) kialakuló $\varrho_a(f)$ frekvenciaszondázási görbék a $\varrho_1 = 10$ Ωm, $h_1 = \infty$; $\varrho_2 = 200$ Ωm, $h_2 = 2$ m; $\varrho_3 = 10$ Ωm, $h_3 =$ változó; $\varrho_4 = 10\,000$ Ωm, $h_4 = \infty$ modellre

*Рис. 5.* Кривые частотного зондирования $\varrho_a(f)$ при расстоянии между передатчиком и приемником ($R$) в 75 м в пласте сопротивлением 200 омм при модели $\varrho_1 = 10$ омм, $h_1 = \infty$; $\varrho_2 = 200$ омм, $h_2 = 2$ м; $\varrho_3 = 10$ омм, $h_3 =$ переменная; $\varrho_4 = 10\,000$ омм, $h_4 = \infty$

In all curves of *Figs. 2–6* the values calculated by the direct current apparent resistivity formula were plotted on the ordinate. These values significantly differ from the resistivity of the layer in which the dipoles are located, even at low frequences; these differences are due to the layering. Identical values can be obtained only if the space is uniform.

From the value of $f_{max}$ belonging to the maximum of the curves, however, an apparent resistivity ($\varrho_{eff}$) can be derived; this being the resistivity of the uniform space which would produce the same effect at the given $R$ and $f_{max}$ as the layered space. In the uniform space the maximum of $\varrho_a(f)$ appears at the

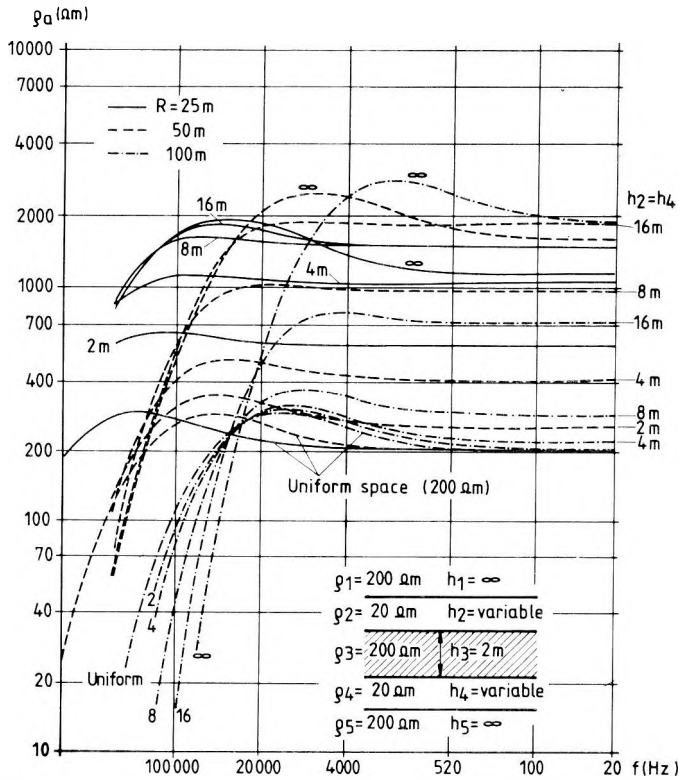


*Fig. 6.* Frequency sounding curves $\varrho_a(f)$ measured in a 200 Ωm seam with transmitter–receiver separations ($R$) of 25 m, 50 m and 100 m for the model $\varrho_1 = 200$ Ωm, $h_1 = \infty$, $\varrho_2 = 20$ Ωm, $h_2$ = variable, $\varrho_3 = 200$ Ωm, $h_3 = 2$ m, $\varrho_4 = \varrho_2 = 20$ Ωm, $h_4 = h_2$ = variable, $\varrho_5 = 200$ Ωm, $h_5 = \infty$

*6. ábra.* A $\varrho_3 = 200$ Ωm-es telepben 25, 50 és 100 m adó–vevő távolságon ($R$) kialakuló $\varrho_a(f)$ frekvenciaszondázási görbék a $\varrho_1 = 200$ Ωm, $h_1 = \infty$; $\varrho_2 = 20$ Ωm, $h_2$ = változó; $\varrho_3 = 200$ Ωm, $h_3 = 2$ m; $\varrho_4 = \varrho_2 = 20$ Ωm, $h_4 = h_2$ = változó; $\varrho_5 = 200$ Ωm, $h_5 = \infty$ modellre

*Рис. 6.* Кривые частотного зондирования $\varrho_a(f)$ при расстояних между передатчиком и приемником ($R$) в 25, 50 и 100 м в пласте сопротивлением 200 омм при модели $\varrho_1 = 200$ омм, $h_1 = \infty$; $\varrho_2 = 20$ омм, $h_2$ = переменная, $\varrho_3 = 200$ омм, $h_3 = 2$ м; $\varrho_4 = \varrho_2 = 20$ омм, $h_4 = h_2$ = переменная; $\varrho_5 = 200$ омм, $h_5 = \infty$

value $R/\delta = 1.6$, from this the skin depth $\delta$ and from it, knowing $f_{max}$, $\varrho_{eff}$ can be obtained.

For the five-layer model of Fig. 6 the following values are obtained for different $h_2 = h_4$ thicknesses:

| $h$(m) | 2 | 4 | 8 | 16 |
|---|---|---|---|---|
| $\varrho_{eff}(R = 25\text{ m})\Omega m$ | 144 | 96 | 64 | 43 |
| $\varrho_{eff}(R = 50\text{ m})\Omega m$ | 173 | 130 | 77 | 45 |

The decreasing trend of $\varrho_{eff}$ can be explained by the increasing influence of the 20 Ωm under- and overlying layers. At the same time, the increase of $h_2$ and $h_4$ increases the field, because the current density increases at the measuring site. This phenomenon results in high apparent resistivity values.

The ratio of the apparent resistivities $\varrho_{eff}(f_{max})/\varrho_a(f\to 0)$ is a characteristic parameter of the layers penetrated by the current. The unit value of the ratio or its value close to unity suggests a uniform space. If this volume is less than 1, then the layer in which the dipoles are located is embedded in a medium of lower resistivity; on the other hand, a value greater than 1 suggests a host rock of higher resistivity.

## 4. Calculation of $\varrho_a^*(f)$ transformed apparent resistivity curves

On the original $\varrho_a(f)$ curve the above-mentioned effects of layering can be discovered only if the curves belonging to the layered model are matched with the curve of the uniform space for comparison. The information on layering can be enhanced, however, if the frequency dependence also appearing in the uniform medium (see *Fig. 1*) is removed from the original $\varrho_a(f)$ curve; in other words, a transformed $\varrho_a^*(f)$ curve is constructed. Using this transformation we obtain for the uniform medium $\varrho_a^*(f)$ = constant = $\varrho_{real}$, that is a straight line parallel to the abscissa.

The basis of transformation is that for each measured $|E_z(f)|$ value the quantity $|E_z(f)|/|E_z(f\to 0)|$ can be calculated, to which a concrete $R/\delta$ belongs based on the relationship shown in *Fig. 1*. Knowing $R$ and $f$ the skin depth can be determined and from this we get the transformed apparent resistivity by means of the formula

$$\varrho_a^*(f) = 3.94 \cdot 10^{-6}\delta^2 f$$

Since for certain models the value of $|E_z(f)|_{max}/|E_z(f\to 0)|$ may exceed the highest value 1.455 possible in the uniform medium, when calculating $\varrho_a^*(f)$ the procedure chosen was to normalize to $|E_z(f)_{max}|$ instead of $|E_z(f\to 0)|$, and the transformation is applied mainly to the descending — high frequency — part of the curves. Thus, with increasing frequency, data which are more and more characteristic of the formations between the electrodes are obtained, this being important in investigating the lateral changes within these formations.

*Fig. 7* presents an enlightening example of the above transformation. For the three-layer model approximating the coal formations the original $\varrho_a(f)$ curves and the transformed $\varrho_a^*(f)$ curves of the descending part of the $\varrho_a(f)$ curves can be seen. On the latter ones the increasing influence of the 2 m thick seam can clearly be seen; it increases $\varrho_a^*(f)$ with increasing frequency. As a matter of fact, at sufficiently high frequencies the electromagnetic channel waves must develop.

The $\varrho_a^*(f)$ values are quantities which can be derived from the shape of the original frequency sounding curve, from the ratio of the $\varrho_a(f)$ values belonging to different frequencies. For the determination of these values only the relative values are required and, thus, they are independent of the dimensions of the dipoles, too.

Judging from our examinations, the position of $\varrho_a(f_{max})$ along the frequency axis allows determining a resistivity value correctly reflecting the summarized effect of the host rock, especially for larger $R$ separations ($R > 75$ m). Because for the direct current geometric sounding the limit

$$\lim_{R\to\infty} \varrho_a(R) = \frac{\varrho^2(\text{seam})}{\bar{\varrho}\ \text{host rock}}$$

exists, and the less the resistivity contrast is the smaller the $R$ separation will be at which the limit is reached, the formula

$$|\varrho_a(f\to 0)| \underset{R\to\infty}{\approx} \frac{\varrho^2(\text{seam})}{\varrho_a^*(f_{max})}$$

can be written. From this a good estimate of the seam resistivity can be obtained. For example, from the curves shown in Fig. 7 the values of 191 Ωm ($R = 12.5$ m), 210 Ωm ($R = 50$ m) and 207 Ωm ($R = 100$ m) are obtained for the $\varrho_{(seam)}$ in the way described above.

## 5. Field of a finite vertical electric dipole

So far the characteristics of the electromagnetic field generated by a vertical elementary electric dipole of unit moment were dealt with.

Because the elementary dipole cannot be realized, it is necessary to examine what kinds of deviations from the theoretical case are caused by the finite transmitter and receiver dipoles. Further on, we will discuss exclusively the model of a relatively thin coal seam embedded in a host rock of lower resistivity; and the groundings of the dipoles may be located in the over- and underlying layers. We examined for the model shown in *Fig. 7* how the field component $|E_z|$ is affected if the transmitter dipole is of finite length, but the current remains 1 A, and how the measured potential difference is affected by the finite receiver dipole.

The effect of the finite transmitter dipole can be taken into account by superposing the effect of several elementary dipoles. In the limiting case the more and more finer divisions lead to integration along the dipole. In order to decide what kind of division—or maybe integration—should be used, we examined for the given model how the value of $E_z$ changes with the position of the transmitter within the layer, for different $z$ values, at dipole dimensions, layer thicknesses, $R$ separations and frequences which can be expected in practice. $E_z$

was found to be practically constant within each layer whereas it changes at the layer boundaries in the same ratio as the resistivities. An example of this for two transmitter positions is shown by *Fig. 8* which gives the numerical values of $\varrho_a$. This means that the elementary transmitter can be located anywhere within the layer, or the elementary transmitters can be replaced by a finite transmitter with a length of the layer thickness.

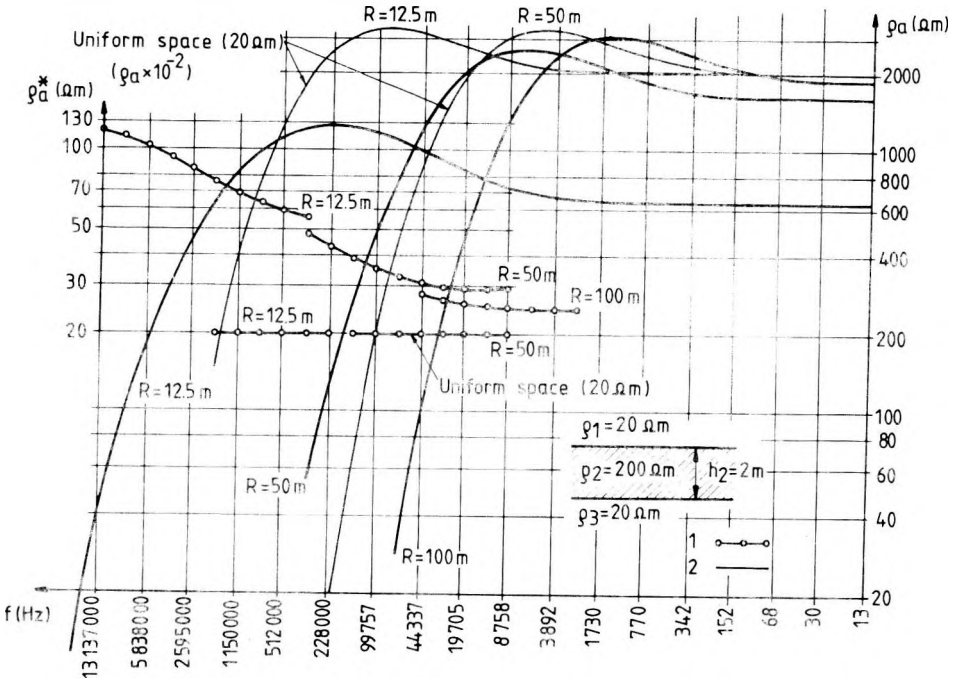


*Fig. 7.* Original $\varrho_a(f)$ and transformed $\varrho_a^*(f)$ frequency sounding curves measured in a 200 Ωm seam with transmitter–receiver separations ($R$) of 12.5 m, 50 m and 100 m for the model $\varrho_1 = 20$ Ωm, $h_1 = \infty$, $\varrho_2 = 200$ Ωm, $h_2 = 2$ m, $\varrho_3 = 20$ Ωm, $h_3 = \infty$. The ordinates of the curves of the 20 Ωm uniform space must be multiplied by 0.01

1—transformed $\varrho_a^*(f)$ curves; 2—original $\varrho_a(f)$ curves

*7. ábra.* A 200 Ωm-es telepben 12,5; 50 és 100 m adó–vevő távolságon ($R$) kialakuló eredeti $\varrho_a(f)$ és transzformált $\varrho_a^*(f)$ frekvenciaszondázási görbék a $\varrho_1 = 20$ Ωm, $h_1 = \infty$; $\varrho_2 = 200$ Ωm, $h_2 = 2$ m; $\varrho_3 = 20$ Ωm, $h_3 = \infty$ modellre. A 20 Ωm-es homogén tér görbéinek ordinátáját 0,01-el szorozni kell.

1 — transzformált látszólagos fajlagos ellenállás, $\varrho_a^*(f)$, görbék; 2 — eredeti $\varrho_a(f)$ görbék

*Рис. 7.* Кривые частотного зондирования, первичные $\varrho_a(f)$ и преобразованные $\varrho_a^*(f)$, при расстояних между передатчиком и приемником ($R$) в 12,5, 50 и 100 м в пласте сопротивлением 200 омм при модели $\varrho_1 = 20$ омм, $h_1 = \infty$; $\varrho_2 = 200$ омм, $h_2 = 2$ м; $\varrho_3 = 20$ омм, $h_3 = \infty$. Ординаты кривых однородного поля 20 омм нужно перемножить на 0,01

1 — кривые преобразованных кажущихся удельных сопротивлений $\varrho_a^*(f)$; 2 — кривые кажущихся удельных сопротивлений $\varrho_a(f)$

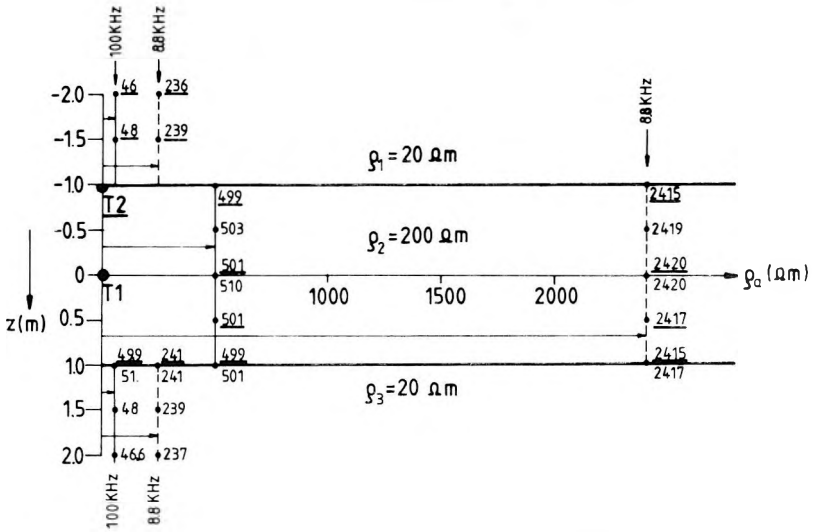


*Fig. 8.* Vertical electric field strengths, $|E_z|$, generated by an elementary dipole of unit moment located in the middle of the 200 Ωm seam (*T*1) and at the upper boundary of the seam (*T*2), respectively, with the transmitter–receiver separation of $R = 50$ m at different $z$ values for the model shown in Fig. 7. Numbers placed next to the dots denote $\varrho_a(f)$ apparent resistivity (those underlined belong to the underlined transmitter position)

*8. ábra.* A 7. ábra modelljében $R = 50$ m adó–vevő távolságon különböző $z$ értékeknél kialakuló $|E_z|$ vertikális elektromos térerősség értékek a 200 Ωm-es telep közepén (*T*1) és a telep felső határán (*T*2) elhelyezett egységnyi momentumú elemi dipól hatására. A pontok melletti számok $\varrho_a(f)$ látszólagos fajlagos ellenállást jelentenek (az aláhúzott számok a *T*2 adóhoz tartoznak)

*Рис. 8.* Значения электрических напряженностей $|E_z|$, возникающих при различных значениях $z$ в модели рис. 7 при расстоянии между передатчиком и приемником $R = 50$ м под влиянием одиночного дипола с единичным моментом, помещенного в центр пласта сопротивлением 200 омм (*T*1) и на верхнюю границу пласта (*T*2). Цифрами рядом с точками обозначаются кажущиеся удельные сопротивления $\varrho_a(f)$ (подчеркнуты цифры, соответствующие передатчику *T*2)

*Fig. 9* relates to the transmitter being located in the lower resistivity layer. Comparing the numerical data of Figs. 8 and 9 we see that if the elementary transmitter gets into the lower resistivity layer, then the field values decrease approximately in the ratio $\varrho_2/\varrho_1$ at the given point; and their values do not significantly depend on the position of the transmitter within this layer. Thus, in this case, too, the elementary transmitters can be replaced by a transmitter of finite length located within the layer.

Another important conclusion can be drawn from the former. For the model in question the field around the receiver dipole can be considered uniform from the point of current density, and it is symmetrical to the axis of the seam, for the given values of $R$ and $z$. Thus, it can be understood that at the layer boundaries, along the receiver line, the value of $|E_z|$ abruptly changes according

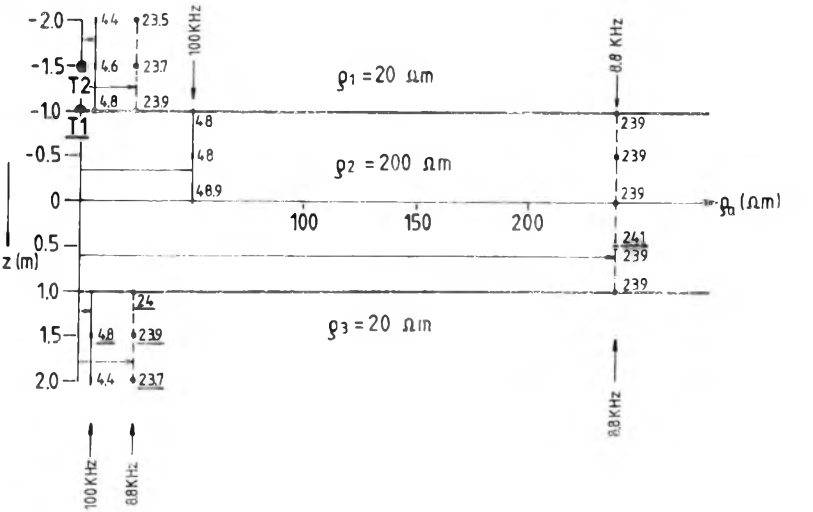


*Fig. 9.* Vertical electric field strengths $|E_z|$, generated by an elementary dipole of unit moment located in the 20 Ωm overlying layer at the boundary of the seam (*T1*) and 0.5 m above it (*T2*), respectively, with the transmitter–receiver separation of $R = 50$ m at different $z$ values for the model shown in Fig. 7. For legend see Fig. 8.

*9. ábra.* A 7. ábra modelljében $R = 50$ m adó–vevő távolságon különböző $z$ értékeknél kialakuló $|E_z|$ vertikális elektromos térerősség értékek a 20 Ωm-es fedüben a telep határán (*T1*) és fölötte 0,5 m-rel (*T2*) elhelyezett egységnyi momentumú elemi dipói hatására. Jelölés, mint a 8. ábrán, az aláhúzott számok a *T1* adóhoz tartoznak.

*Рис. 9.* Значения электрических напряженностей $|E_z|$, возникающих при различных значениях $z$ в модели рис. 7 при расстоянии между передатчиком и приемником $R = 50$ м под влиянием одиночного диполя с единичным моментом, помещенного в кровлю сопротивлением 20 омм на границу с пластом (*T2*). Обозначения – как на рис. 8, подчеркнуты цифры, соответствующие передатчики *T1*

to the ratio of resistivities. After all, the field of the finite dipole can be determined from a single quantity related to the central layer, taking into account the uniformity according to the current density, and knowing in which layer the transmitter part of finite length is located.

Field strengths $|E_{z2}|$, $|E_{z1}|$ and $|E_{z3}|$ within the respective layer are obtained by summing up the $|E_z|$-s generated by the individual transmitter parts *(Fig. 10)*. The field strengths belonging to a unit length of transmitter and generated by the individual transmitter parts in their own layer can be expressed with the field strength belonging to a unit length of transmitter and generated by the transmitter in the central layer, $e_z = \dfrac{|E_z|}{dl}\,\dfrac{\mathrm{V}}{\mathrm{m}^2}$ where $dl$ is the dipole length. E.g. the field strength generated in the upper layer by a transmitter of unit length located in the upper layer is obtained by determining the field strength generated in the central layer by the upper transmitter first, which is $(\varrho_1/\varrho_2)e_z$, then—using the uniformity of the current—from this the field strength in the upper layer,

i.e. $(\varrho_1/\varrho_2)^2 e_z$. Then, using the notations of Fig. 10, and taking into account the finite length of the transmitters and the uniformity of the current, the following relationships are obtained:

$$|E_{z2}| = e_z T_2 + \left(\frac{\varrho_1}{\varrho_2}\right)^2 e_z \frac{\varrho_2}{\varrho_1} T_1 + \left(\frac{\varrho_3}{\varrho_2}\right)^2 e_z \frac{\varrho_2}{\varrho_3} T_3 = e_z \left(T_2 + \frac{\varrho_1}{\varrho_2} T_1 + \frac{\varrho_3}{\varrho_2} T_3\right),$$

$$|E_{z1}| = e_z \frac{\varrho_1}{\varrho_2} T_2 + \left(\frac{\varrho_1}{\varrho_2}\right)^2 e_z T_1 + \left(\frac{\varrho_3}{\varrho_2}\right)^2 e_z \frac{\varrho_1}{\varrho_3} T_3 = e_z \frac{\varrho_1}{\varrho_2} \left(T_2 + \frac{\varrho_1}{\varrho_2} T_1 + \frac{\varrho_3}{\varrho_2} T_3\right),$$

$$|E_{z3}| = e_z \frac{\varrho_3}{\varrho_2} T_2 + \left(\frac{\varrho_1}{\varrho_2}\right)^2 e_z \frac{\varrho_3}{\varrho_1} T_1 + \left(\frac{\varrho_3}{\varrho_2}\right)^2 e_z T_3 = e_z \frac{\varrho_3}{\varrho_2} \left(T_2 + \frac{\varrho_1}{\varrho_2} T_1 + \frac{\varrho_3}{\varrho_2} T_3\right).$$

Let us denote the expression in brackets as $A_r$ and call it "reduced transmitter length". The field is perceived by the dipole of finite length spreading beyond the central layer. Knowing the field strengths in the individual layers, the potential difference measured by the receiver is

$$\Delta U = |E_{z2}| M_2 + |E_{z1}| M_1 + |E_{z3}| M_3$$

where $M_1$, $M_2$ and $M_3$ are parts of the $MN$ separation within the respective layers.

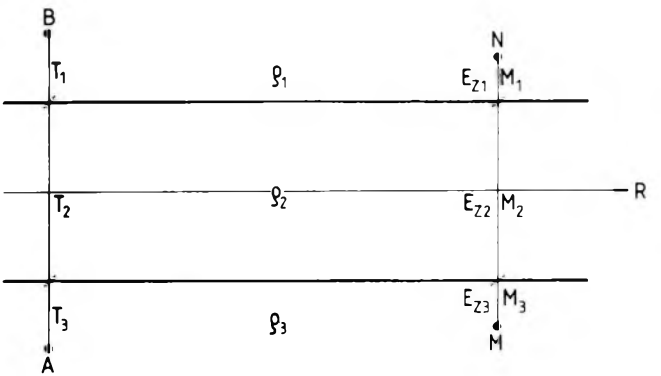


*Fig. 10.* The symmetric transmitter and receiver dipoles of finite size extending over the under- and overlying layers ($T_1$, $T_2$, $T_3$ and $M_1$, $M_2$, $M_3$ indicate the parts of the dipoles in the respective layers)

*10. ábra.* A fedőbe és fekübe átnyúló szimmetrikus elhelyezkedésű véges méretű adó- és vevő-dipól ($T_1$, $T_2$, $T_3$, illetve $M_1$, $M_2$, $M_3$ jelöli az egyes rétegekbe eső dipólszakaszokat)

*Рис. 10.* Диполи передатчика и приемника конечних размеров, расположенные симметрично и проникающие в кровлю и почву (отрезки диполей в ордельно слоях обозначены через $T_1$, $T_2$, $T_3$, а также $M_1$, $M_2$ и $M_3$)

After substitution and re-arrangement

$$\Delta U = e_z A_r \left( M_2 + \frac{\varrho_1}{\varrho_2} M_1 + \frac{\varrho_3}{\varrho_2} M_3 \right) = e_z A_r M_r$$

where the expression in brackets is marked with $M_r$; this can be called "reduced receiver length".

The accuracy of the calculation based on the single quantity related to the central layer can be checked by using for comparison a more accurate value calculated by a program involving the layer relations as well, i.e. starting from the two different ways of $\Delta U$ calculations. Calculated from one single transmitter $\Delta U = e_z A_r M_r$. With the program involving the layer relations

$$\Delta U_P = (e_z T_2 + e_{z12} T_1 + e_{z32} T_3) M_2 + (e_{z21} T_2 + e_{z11} T_1 + e_{z31} T_3) M_1 + \\ + (e_{z23} T_2 + e_{z13} T_1 + e_{z33} T_3) M_3.$$

Here, in each case $e$ indicates the field strengths generated by the transmitters of unit length, namely, $e_z$ indicates the field strength generated in the central layer by the transmitter in the central layer (this is also used when calculating from the single quantity)

$e_{z12}$ indicates the field strength generated in the central layer by the transmitter in the upper layer,

$e_{z31}$ indicates the field strength generated in the lower layer by the transmitter in the upper layer,

$e_{z21}$ indicates the field strength generated in the upper layer by the transmitter in the central layer,

$e_{z11}$ indicates the field strength generated in the upper layer by the transmitter in the upper layer.

For the model of Fig. 7 and for a separation of $R = 50$ m, if both the transmitter and receiver dipoles are 2.5 m long, i.e. both dipoles have two, 0.25 m long parts in the host rock, the percentage errors calculated using the formula

$$h\% = \frac{\Delta U_P - \Delta U}{\Delta U_P} 100$$

are as follows

| $f$(Hz) | 20 | 70 | 230 | 780 | 2600 | 3800 | 30 000 | 100 000 |
|---|---|---|---|---|---|---|---|---|
| $\Delta U(\mu V)$ | 4245 | 4274 | 4396 | 4871 | 5875 | 6468 | 4488 | 1366 |
| $\Delta U_P(\mu V)$ | 4244 | 4273 | 4395 | 4870 | 5876 | 6468 | 4487 | 1363 |
| $h\%$ | −0.024 | −0.023 | −0.023 | −0.021 | +0.017 | 0 | −0.022 | −0.22 |

It can be seen that calculation from the single quantity causes only negligible error, thus, the uniformity according to current density is relevant for the dimensions and frequencies discussed.

*

Based on the peculiarities of the frequency sounding curves obtained for the geological models examined in this paper, the equatorial electric frequency sounding curves of the buried vertical current dipole can be utilized for

— examining the over- and underlying layers,
— examing the lateral inhomogeneities within the coal seam from a single gallery, with measurements between two galleries or with cross-hole measurements,
— monitoring the changes of resistivity with time.

Concerning the last application it is advantageous that the examined rock volume can be controlled by changing the frequency, i.e. fixed electrodes can be used. As far as the first two tasks are concerned, it is advisable to use the $\varrho_a^*(f)$ transformed curve or, rather, the difference between the transformed curve calculated for a basic model and the measured transformed curve.

## REFERENCES

Csókás J., Dobróka M., Gyulai Á. 1986: Geoelectric determination of quality changes and tectonic disturbances in coal deposits. Geophysical Prospecting, **34**, 7, pp. 1067–1081

Breitzke M., Dresen L., Csókás J., Gyulai Á., Ormos T. 1987: Parameter estimation and fault detection by three-component seismic and geoelectrical surveys. Geophysical Prospecting, **35**, 7, pp. 832–863

Takács E., Nagy J., Mádai F. 1986: Field of a vertical, alternating current, electric elementary dipole in a layered medium. Geophysical Transactions, **32**, 1, pp. 43–56

## BÁNYABELI FREKVENCIASZONDÁZÁS FÖLDELT ÁRAMDIPÓLUSSAL

TAKÁCS Ernő

A széntelepben levő ekvatoriális felállású váltóáramú elemi dipólus vertikális elektromos térerősségének értéke és frekvenciafüggése a telepben a rétegzett tér rétegei fajlagos ellenállásának és vastagságának függvénye. A tanulmány ezen paraméterek hatásával foglalkozik olyan modellekre, amelyek a valóságban előforduló laterális inhomogenitásokat, fekü és fedü viszonyokat tükrözik. A homogén térben kialakuló frekvencia-függés felhasználásával a térerősség frekvencia szerinti változásából látszólagos fajlagos ellenállások vezethetők le ($\varrho_a^*(f)$). Ezek frekvenciaszondázási görbéje a rétegződés hatását szemléletesebben mutatja, mint magának a térerősségnek a frekvenciafüggése. A geometriai tényezővel számított látszólagos fajlagos ellenállás, $\varrho_a(f)$ és $\varrho_a^*(f)$ együttes felhasználásával megkapható a telep fajlagos ellenállása és vizsgálható a mérésre hatással levő térrész változása a frekvenciával. A frekvencia növekedésével a telep hatása — különösen a kisebb adó–vevő távolságoknál — fokozódik, ami a telep kutatása szempontjából előnyös. Az elemi dipólus telepben kialakuló térerősségéből a méretek és fajlagos ellenállás viszonyok figyelembevételével levezethető a kísérő rétegekbe átnyúló, véges méretű adó és vevő használatával mért feszültség.

## ПОДЗЕМНОЕ ЧАСТОТНОЕ ЗОНДИРОВАНИЕ ПРИ ЗАЗЕМЛЕННОМ ПИТАЮЩЕМ ДИПОЛЕ

Эрнё ТАКАЧ

Значение ветрикальной электрической напряженности одиночного экваториального диполя переменного тока, помещенного в угольный пласт, и ее частотная зависимость в пласте являются функцией от удельных сопортивлений и мощностей слоев расслоенного пространства. В настоящей работе рассматривается влияние этих параметров на модели, отражающие неоднородности по латерали, а также характер кровли и почвы, наблюдаемые в действительности. При использовании частотной зависимости, возникающей в однородном пространстве, по изменениям напряженности в зависимости от частоты можно вывести кажущиеся удельные сопротивления ($\varrho_a^*(f)$). Кривыми частотных зондирований по ним значительно нагляднее иллюстрируется влияние слоистости, нежели частотной зависимостью самой напряженности. При совместном использовании кажущихся удельных сопротивлений $\varrho_a(f)$ рассчитанных с учетом геометрического фактора, и $\varrho_a^*(f)$, можно определить удельное сопротивление пласта и изучить зависимость части пространства, оказывающей влияние на результаты измерений, от частоты. С увеличением частоты эффект от пласта возрастает, особенно при меньших расстояниях между передатчиком и приемником, что является благоприятным обстоятельством для разведки пласта. По напряженности поля в пласте от одиночного диполя с учетом размеров и удельных сопротивлений можно определить напряжение, измеряемое при использовании передатчика и приемника конечных размеров, протягивающихся и в соседние слои.

ON THE BANKS OF THE DANUBE

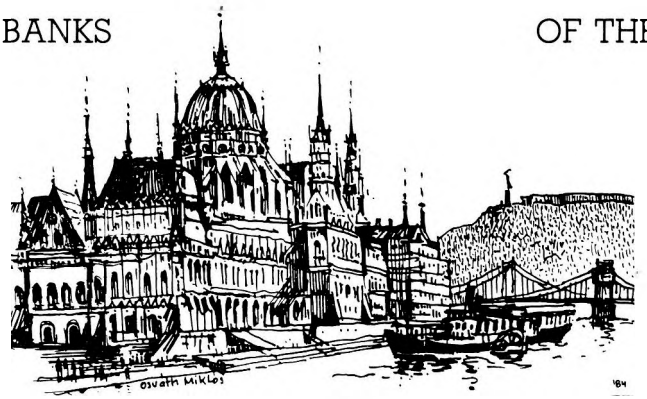


# 34th INTERNATIONAL GEOPHYSICAL SYMPOSIUM AND TECHNICAL EXHIBITION

BUDAPEST, HUNGARY
4–8 September 1989

The 1989 Symposium will be held at:

KARL MARX UNIVERSITY OF ECONOMICS
in the city of Budapest

This year's symposium will be organized by the Association of Hungarian Geophysicists together with the geophysical societies and institutions from the participating socialist countries.

For bookings please complete and return the attached cards.

for further information regarding the Symposium, Technical Exhibition and accomodation, please write to:
Magyar Geofizikusok Egyesülete
Budapest
Anker koz 1.
Hungary
1061
Telex: 22 53 69 MTESZ MGE h
Telephone: (36)-1-429-754

MAGYAR GEOFIZIKUSOK EGYESÜLETE 1954 MUNKÁNK TÁRSA

GEOPHYSICAL SYMPOSIUM BUDAPEST 4-8 SEPT. 1989 34 ГЕОФИЗИЧЕСКИЙ СИМПОЗИУМ